TIMPAN

***T**echnologies to **IMP**rove **A**irframe **N**oise*

***S**pecific **T**argeted **RE**search **P**roject*

Thematic Priority 4: Aeronautics and Space

Project number 030870

Extracts of Public Information

AIAA/CEAS Aeroacoustics Conference, Miami, 2009, Paper No. 2009-3276

Experimental Assessment of Low Noise Landing Gear Component Design

Werner Dobrzynski[1]
Deutsches Zentrum für Luft- und Raumfahrt (DLR), 38108 Braunschweig, Germany

Leung Choi Chow[2]
Airbus, Filton, Bristol, BS99 7AR, Great Britain

Malcolm Smith[3]
ISVR, University of Southampton, Highfield Hampshire, Great Britain

Antoine Boillot[4]
Messier-Dowty SA, 78142 Velizy Villacoublay, France

Olivier Dereure[5]
Messier-Bugatti SA, 78141 Velizy Villacoublay, France

and

Nicolas Molin[6]
Airbus, 31060 Toulouse, France

Landing gear related airframe noise is one of the dominant aircraft noise components at approach. It therefore is essential to particularly reduce landing gear noise. In the European SILENCER project, advanced low noise gears had been designed and tested at full scale. In the current European co-financed project TIMPAN (Technologies to IMProve Airframe Noise) still more advanced low noise design concepts were investigated and noise tested on a ¼ scaled main landing gear model in the German-Dutch Wind Tunnel. A variety of gear configurations were tested including a new side-stay design, different modifications of bogie inclination, wheel spacing, bogie fairings with different flow transparency, leg-door configurations and brake fairings. The acquired farfield noise data are compared against the results from a landing gear noise prediction model, transposed to full scale flight conditions and compared against the full scale test data obtained for the SILENCER advanced A340 style 4-wheel main landing gear. An optimal combination of tested gear modifications led to a noise reduction of up to 8 dB(A) in terms of overall A-weighted noise levels relative to the SILENCER reference gear configuration.

I. Introduction

Due to the advances in aircraft engine noise reduction, airframe noise became a major noise component during approach and landing. For wide body aircraft in particular the dominant airframe noise sources are the landing gears followed by aerodynamic noise originating from deployed high-lift devices.

[1] Research Engineer, Institute of Aerodynamics and Flow Technology, Lilienthalplatz 7, 38108 Braunschweig, Germany.
[2] Engineer, Aerodynamics Department, Building 09B, Filton, Bristol, England BS99 7AR, Great Britain.
[3] Research Engineer, University of Southampton, Highfield Hamphire, Great Britain.
[4] Research Engineer, R&T Department, Zone Aéronautique Louis Breguet, 78142 Vélizy-Villacoublay, France
[5] Research Engineer, R&T Department, Zone Aéronautique Louis Breguet, 78141 Vélizy-Villacoublay, France
[6] Research Engineer, Acoustics and Environment Department, 316 route de Bayonne, 31060 Toulouse, France

Accordingly numerous research efforts were made to reduce landing gear noise either through dedicated wind tunnel experiments or flight tests [1, 2]. Initial noise reduction solutions were the application of solid add-on fairings to protect the complex landing gear structure from the flow [3 - 6]. Based on the results of these experiments it was realized that flow displacement by such fairings could be detrimental regarding additional noise originating from gear components adjacent to those which were faired. As a solution of this problem porous fairings were developed, which would reduce the magnitude of flow displacement but still result in a sufficiently low wake flow velocity not to generate high interaction noise levels with the downstream gear components [7 - 9].

While add-on solutions could be applied at short terms for current aircraft it was realized that low noise gears for future aircraft can best be developed by accounting for noise aspects already in the design stage. A corresponding effort was undertaken in the European research project SILENCER ("Significantly Lower Community Exposure to Aircraft Noise") [10].

Based on the results of this study, a combination of low noise gear component design and the application of porous fairings [7] was considered to exploit the maximum possible noise reduction potential. This work was performed in an European co-financed research project entitled "Technologies to IMProve Airframe Noise" (TIMPAN) with partners from European aircraft industries, research establishments and academia and focused on an A340 style 4-wheel main landing gear which was originally used in SILENCER, but only limited noise reduction had been achieved accompanied by some weight penalty.

The objective of the TIMPAN study therefore was to develop operational low noise main landing gear components without weight penalties, taking into account modifications in the gear architecture (e.g. wheel spacing and bogie angle) and to optimize and quantify the benefit from the application of porous fairings for various gear components. As in SILENCER the design was based on the relevant constraints predefined by gear functionality and safety for real aircraft application.

II. Main Landing Gear Configurations

The design work was based on the SILENCER advanced A340 type 4-wheel main landing gear configuration and focused on

- a low noise design of individual gear components known to represent major noise contributors (e.g. side-stay, various links, leg-door structure and brakes) and
- the noise-wise optimal arrangement of gear components to minimize the interaction of high speed turbulent inflow with complex gear structures (e.g. variation of bogie angle, wheel spacing, placement of fairings and additional ramp door).

Fig. 1 presents a comparison between the SILENCER reference configuration and one of the TIMPAN configurations to better understand the design philosophy in TIMPAN. One of the drawbacks of the SILENCER design was the excessive weight of the telescopic side-stay which, however, allowed for a noise-wise optimal design of the leg-door structure. In TIMPAN therefore a new side-stay design also required a new low noise leg-door design. As shown in Fig. 1 this is a door which is articulated in a way to (once the gear is deployed) protect the complex leg/ drag stay structure from the high speed inflow. It should also be noted (Fig. 1) that for both the SILENCER and the TIMPAN gear design the torque link is installed in front of the leg and is protected through a fairing, while in the back only a narrow slave link is attached to guide the dressings.

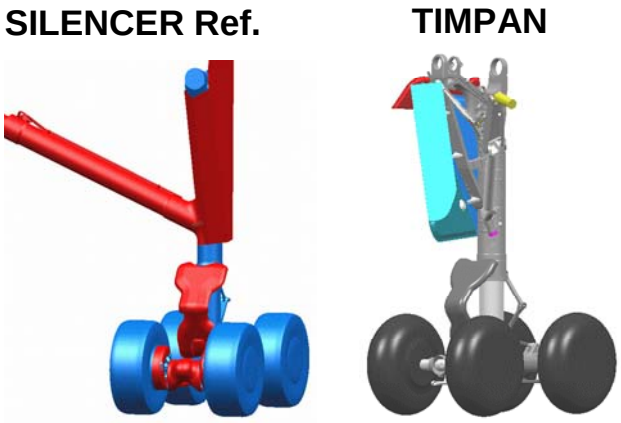

Figure 1. Comparison of SILENCER and TIMPAN main landing gear concepts

Much effort was directed towards the development of a side-stay which could be almost as quiet as the SILENCER clean circular telescopic stay. The final design is depicted in Fig. 2. Compared with the current A340 design the major advantage is the integration of the down-lock springs into the stay to realize a comparatively "clean" design of the components' outer contours. In addition an upstream ramp was provided to, at the same time, shield the still complex stays' geometry, the upper leg area and the cavity aperture from the flow.

Also advanced brake fairings were developed in TIMPAN. The brakes were partly recessed and completely separated from the flow by a streamlined fairing. To allow for the necessary brake cooling a mesh-window was foreseen (Fig. 3).

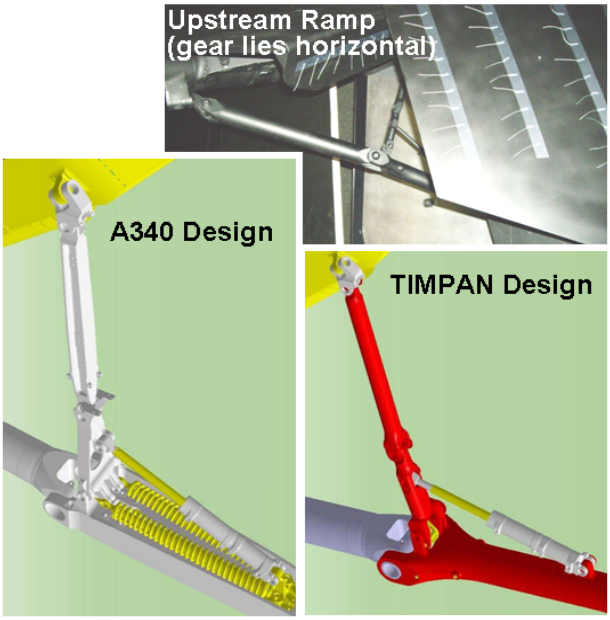

Figure 2. TIMPAN side-stay design and upstream ramp

A low noise arrangement of selected bogie components included:

- Variation of the bogie angle from 0° (reference) to -15° toe down.
- Identification of a potentially optimal wheel spacing (Fig. 4) combined with different bogie- and torque link fairings (solid and porous, respectively).

A "narrow" wheel spacing was defined as reduced spacing by 50% of the tire width relative to the reference total tire spacing and analogous "wide" as a 50% of tire width increase in wheel spacing.

Examples of the application of solid or porous bogie fairings in combination with a solid or porous torque link fairings are presented in Fig. 5.

Due to budget limitations in TIMPAN only scale model tests were planned in order to make use of the already existing ¼ scaled SILENCER main landing gear high fidelity mock-up. Accordingly all new gear components were manufactured at that scale to fit to the existing mock-up. The advantage of testing at model scale was that a wide range of configurations could be tested due to correspondingly short stopovers for gear modification.

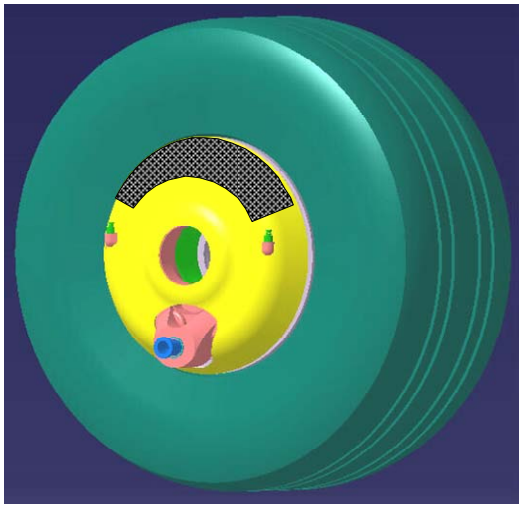

Figure 3. Brake faring with mesh type insert for brake cooling

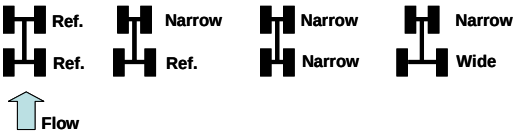

Figure 4. Schematic of selected combinations of forward and rear wheels' spacing

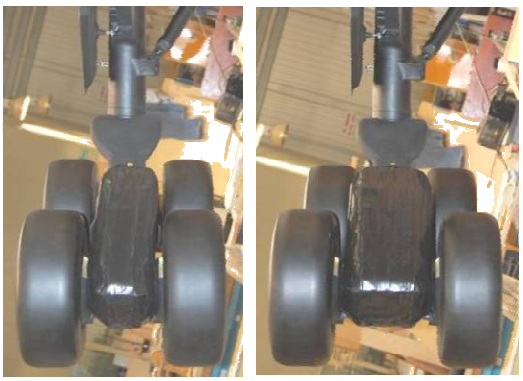

Figure 5. Bogie fairings in combination with torque link fairings for different wheel spacing

III. Experiments

Noise measurements were performed in the DNW-LLF (German-Dutch Wind tunnel – Large Low Speed Facility) in its free-jet configuration with a nozzle cross section of 6 m by 6 m. The maximum wind speed for this tunnel configuration is 78 m/s (152 kts), which is close to the typical landing/ approach speed for current commercial aircraft. The anechoic test-hall (the lower limiting frequency is 80 Hz for broadband noise) allows farfield noise meas-

urements outside the flow field at lateral distances up to about 18 m from the very landing gear which is well in both the acoustic and geometric farfield.

A. Wind Tunnel Test Set-up

As in SILENCER the model gear was installed in a side-wall of 7 m length, which forms an extension of one side of the wind tunnel nozzle (Fig 6). In x-direction (i.e. streamwise) the gear was installed at a distance of about 5 m from the nozzle exit plane. The height of the side-wall is 8 m at the nozzle and 9 m at its trailing edge (accounting for free jet spreading). Those areas along the wall surface (upper and lower edge areas), which are exposed to the wind tunnel shear layer flow, are treated with absorptive material to minimize flow noise generation and radiation from the side-wall. For the same reason the wall's trailing edge features a saw-tooth shape.

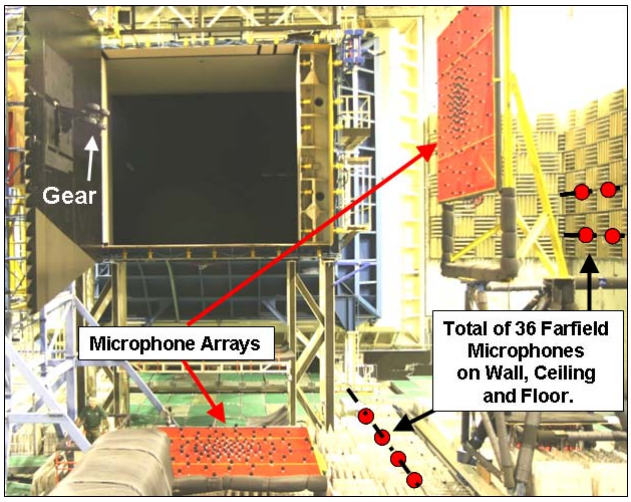

Figure 6. Overview of the measurement set-up in the DNW-LLF 6 m by 6 m open test section

The side-wall arrangement was used to simulate the "in-flight" geometric/acoustic environment (reflection geometry from the wing surface) and to reduce flow noise radiation from the support structure. In order to simulate the actual in-flight lower wing surface boundary layer thickness the wind tunnel boundary layer was "peeled off" by means of a scoop which is installed along the side-wall's leading edge. In TIMPAN the existing DNW test set up was adapted to install the ¼ scale mock-up of an A340 type main landing gear for later comparison with the SILENCER WP 2.3 advanced full scale main landing gear test results [10].

During landing/ approach the A340 aircraft typically operates at a characteristic angle-of-attack with respect to the inflow direction. Since in the test set-up the flow direction has to be parallel to the surface of the side-wall this difference between inflow direction and aircraft axis must be accounted for. Based on the gear installation angle in the aircraft (and accounting for deviations of local flow- from flight-directions) a slight backward gear-leg orientation was decided upon for the wind tunnel set-up. On the aircraft the main landing gear-leg is (laterally) inclined with respect to the lower wing surface. Therefore in the test set-up a corresponding inclination angle was realized between the gear-leg and the surface of the side-wall.

The gear bay geometry was not exactly reproduced. Instead an almost rectangular bay was used, internally lined with absorbing foam to avoid acoustic resonance phenomena. However, the bay aperture was exactly simulated.

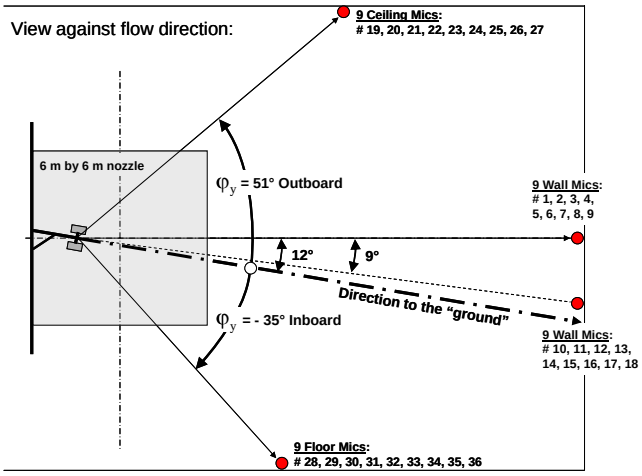

Figure 7. Selected farfield microphone positions on the wind tunnel side wall, the ceiling and the tunnel floor

B. Measurement Techniques and Data Analysis

A similar measurement set-up was applied as in the preceding SILENCER test, i.e. 2 microphone arrays "looking" to the gear from two directions and 4 different rows of microphones (with microphones distributed in flow direction) were installed close to the wall (2 rows), the floor (1 row) and the ceiling (1 row), respectively (Fig. 7). That way noise radiation both towards the "ground" and in sideline directions were determined. In each individual row 9 microphones were positioned at angular increments of about 10° or less in streamwise direction, covering a range of polar angles between about $60° < \varphi_x < 125°$ (Fig. 7). All farfield measurement positions were equipped with 1/2"-diameter LinearX M51 type electret

freefield microphones. Acoustic data were acquired up to a frequency of 40 kHz.

The analysis and reduction of farfield noise data aimed at the determination of noise level spectra and radiation directivities for different landing gear configurations at different flow velocities. If this basic information is at hand, the measured data may ultimately be extrapolated towards the operational conditions as specified for approach noise certification. To obtain the true source characteristics from wind tunnel out-of-flow acquired acoustic data, sound pressure levels have to be corrected for insufficient signal-to-noise ratio, for the effects of shear-layer refraction [11] (including wave convection), microphone directivity, atmospheric absorption [12] and for the effect of convective amplification (assuming dipole type sources). All farfield noise data were normalized towards a constant propagation radius and will be presented in terms of 1/3-oct. band levels.

To visualize local flow conditions at selected gear components tufting tests were performed. Pictures from two different view angles were recorded by means of two video cameras.

IV. Test Results

To ensure the quality of the data, the test started with a background noise measurement for the clean side-wall, i.e. without gear and closed gear cavity. The test matrix comprised a total number of 47 gear configurations, resulting from different combinations of individual gear component designs. In order to save measurement time, different from the "standard" procedure of testing for all configurations at 3 different speeds, the majority of configurations were tested at 2 speeds only (i.e. 78 and 62.5 m/s).

To enable an extrapolation of noise data towards speeds beyond the measurement range respective scaling laws must be defined. As one result of previous landing gear noise tests, dipole type noise source mechanisms were found to dominate. Therefore the following velocity scaling of levels and frequencies pertain:

$$\Delta L = 10 \cdot \log\left(v/v_{ref}\right)^6 \tag{1}$$

based on an arbitrary reference speed v_{ref} . From measured frequencies f and flow velocities v the relevant non-dimensional Strouhal number St can be calculated as

$$St = \frac{f \cdot s}{v} = \text{const.} \tag{2}$$

with s as characteristic length scale or scale factor.

In order to allow for the comparison of earlier results from full scale tests in SILENCER with the current scale model data in TIMPAN the identical length scale s can be applied, but multiplied by the relevant scale factor thus automatically accounting for 4 times higher frequencies in this model experiment.

To finally present source noise level directivities and account for the source size (model scale factor) at the same time, all data will be referenced towards a constant propagation distance r_{ref} based on spherical sound attenuation relative to the measurement distance r and accounting for the model (source) size through

$$L_{ref} = L + 20 \cdot \log\left(r/r_{ref}\right) + 20 \cdot \log\left(s_{ref}/s\right) \tag{3}$$

The data from microphones at similar streamwise (φ_x) positions but for slightly different azimuthal angles in the range of $3° < \varphi_y < 12°$ (corresponding to the two rows of microphones on the test hall wall) were averaged and considered to represent the noise characteristic for radiation direction towards the "ground". This was considered reasonable since the respective level spectra show similar and systematic variations for all tested gear configurations in the order of less than 1 dB.

In order to check the validity of the anticipated scaling laws to account for the effect of flow speed on broadband landing gear noise, in the following spectra are presented in a non-dimensional form based on Equ. (3) to normalize levels and Equ. (2) to calculate Strouhal numbers from measured frequencies.

Prior to any comparison of noise spectra for different gear configurations as studied in TIMPAN it is worthwhile to check how well the noise spectrum for the original SILENCER full scale advanced main landing gear compares to the noise spectrum as obtained for the ¼ scale gear in its SILENCER reference configuration after transposition to full scale conditions according to Equs. (2) and (3). This comparison is depicted in Fig. 8 and shows a surprisingly good agreement except for a level peak at a frequency of about 1 kHz. It is interesting to note that both at model scale and at full scale a similar level peak occurs, but with a much higher level for the scale model gear. The comparison of broadband noise levels is excellent for forward arc radiation directions while, compared to the full scale build, the model gear turns out to be about 1 to 2 dB noisier for rear arc radiation directions.

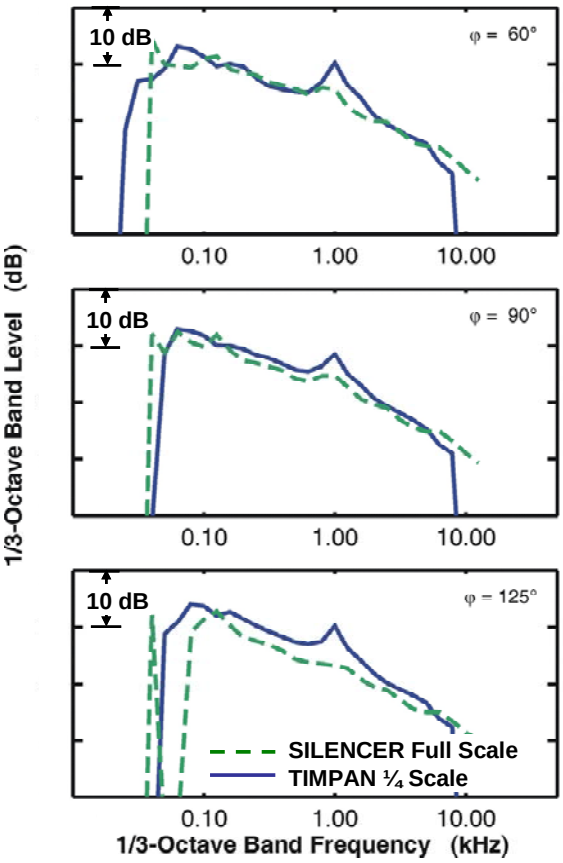

Figure 8. Comparison of normalized 1/3-oct. band level spectra for the TIMPAN ¼ scaled model gear in its SILENCER reference configuration with the spectrum for the original full scale SILENCER advanced gear for different polar radiation angles

As is obvious from this figure the chosen data reduction procedure (effect of speed presented for the reference configuration only) in the average provides reasonable results for all three radiation directions, i.e. in the forward arc ($\varphi_x = 60°$), corresponding to an aircraft in overhead position ($\varphi_x = 90°$), and into the rear arc ($\varphi_x = 125°$), respectively. Fig. 9 also shows that compared to the SILENCER reference configuration, a broadband noise reduction potential of up to about 10 dB is obtained for the quietest TIMPAN gear design. This noise reduction potential is most pronounced for the most important forward arc radiation direction. At very low Strouhal numbers the noise reduction potential is quite limited but still 2 to 4 dB.

2. Normalized noise level directivities

From the comparison of the spectra presented above it is obvious that there is some Strouhal number effect on the noise directivity characteristics. Noise level directivity

A further analysis of this apparent "tone" noise effect showed that this level peak scales on a Strouhal number basis and would correspond to a vortex shedding frequency from the dressings, which were simulated in TIMPAN by electric wire material. Any noise reduction potential derived from the ¼ scale model reference gear therefore must account for this particular model effect.

A. Noise Characteristics

1. Normalized noise level spectra

In Fig. 9 noise spectra are shown for the SILENCER reference configuration and the quietest TIMPAN configuration, respectively. This latter gear configuration combines the following features:

- Negative bogie angle (toe down),
- Narrow wheel spacing (both forward and rear wheel sets),
- Porous bogie and torque link fairings,
- TIMPAN brake fairings,
- Articulated TIMPAN door with 45° ramp and
- TIMPAN side-stay design.

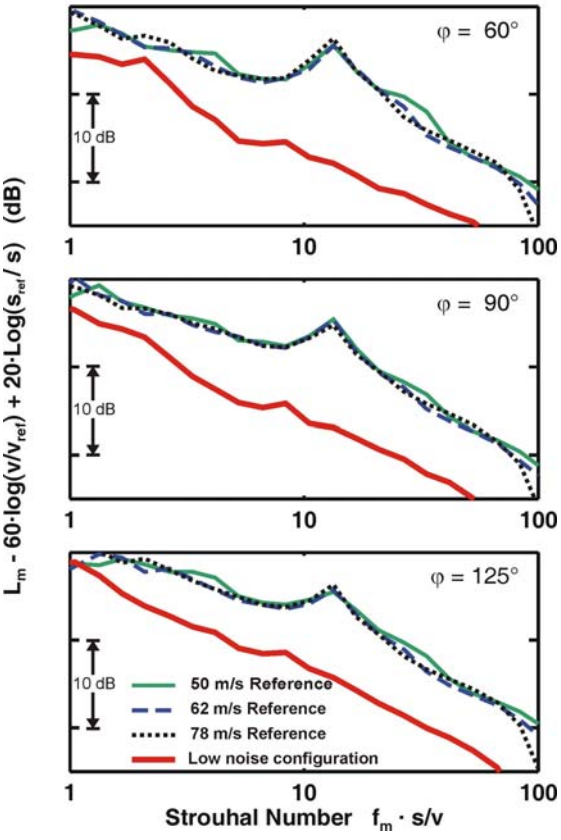

Figure 9. Comparison of normalized 1/3-oct. band noise spectra for the SILENCER reference and the TIMPAN low noise configuration for different polar radiation angles

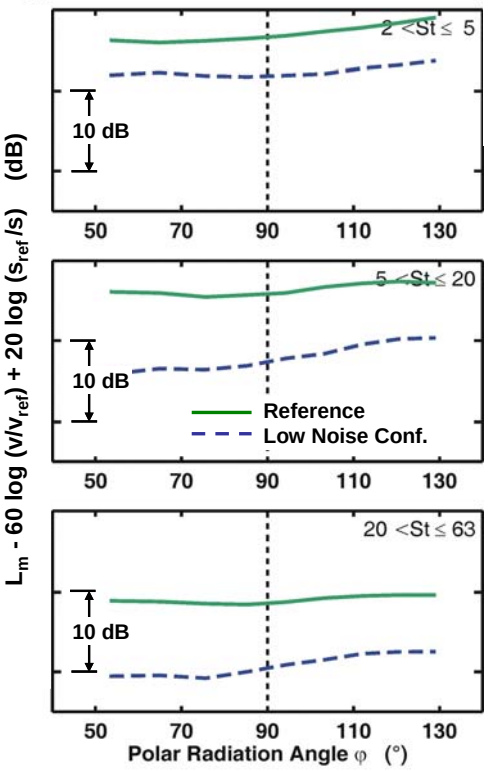

Figure 10. Comparison of polar directivities of normalized 1/3-oct. band noise levels in different bands of Strouhal number for the SILENCER reference and the TIMPAN low noise configuration

these graphs the solid black line indicates the position of the wall. While for the SILENCER reference configuration (upper part of Figure 11) the bogie area can be identified as the predominant noise source, with the gear in its low noise configuration (lower part of Figure 11) the highest noise levels originate from the leg-door/ side-stay area (Note: maximum levels are much lower for ID 55). From these results the conclusion can be derived that the TIMPAN low noise design was successful in dramatically reducing bogie related noise sources but needs further attention regarding an effective low noise design of the leg-door/ side-stay structure.

This conclusion is supported by the results from sideline measurements. Fig. 12 present a comparison of normalized landing gear noise directivities under the line of flight and for both outboard and inboard sideline radiation directions, respectively, for the SILENCER reference configuration and the TIMPAN low noise configuration. Note that for the SILENCER reference ities will therefore be presented for three different Strouhal number ranges. Sound energy is respectively integrated in the three ranges: $2 < St \le 5$; $5 < St \le 20$ and $20 < St \le 63$.

This normalized data representation inherently accounts for small differences in actual test speeds. Corresponding examples of noise directivities are presented in Fig. 10 for the SILENCER reference configuration and the TIMPAN low noise configuration, respectively. While the SILENCER configuration exhibits an almost omnidirectional noise radiation characteristic for the whole Strouhal number range of interest, the corresponding directivities for the low noise configuration feature an increasing level gradient with increasing Strouhal number, i.e. low levels in the forward arc and high levels in the rear arc radiation direction. Accordingly the TIMPAN low noise configuration provides an increasing noise reduction potential for higher Strouhal numbers and forward arc radiation direction.

In an attempt to explain this change in the respective noise level directivities, array source plots can be inspected. Most interesting results are provided by the microphone array presenting source distributions from a sideline view (Fig. 11). In

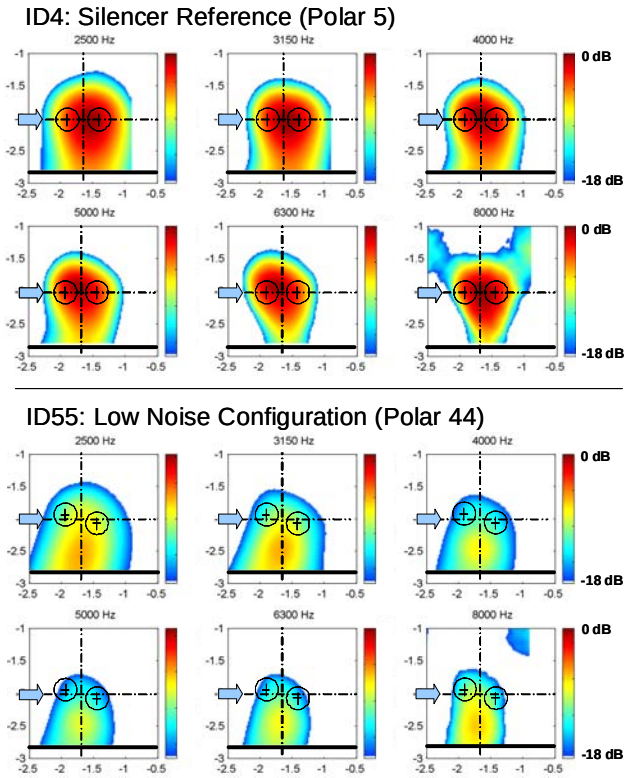

Figure 11. Comparison of noise source distributions from a "side view" for the SILENCER reference configuration and the TIMPAN low noise configuration and different 1/3-oct. band frequencies, respectively (wind speed from left to right; same level scales for the two configurations at identical frequency but autoscaling for different frequencies)

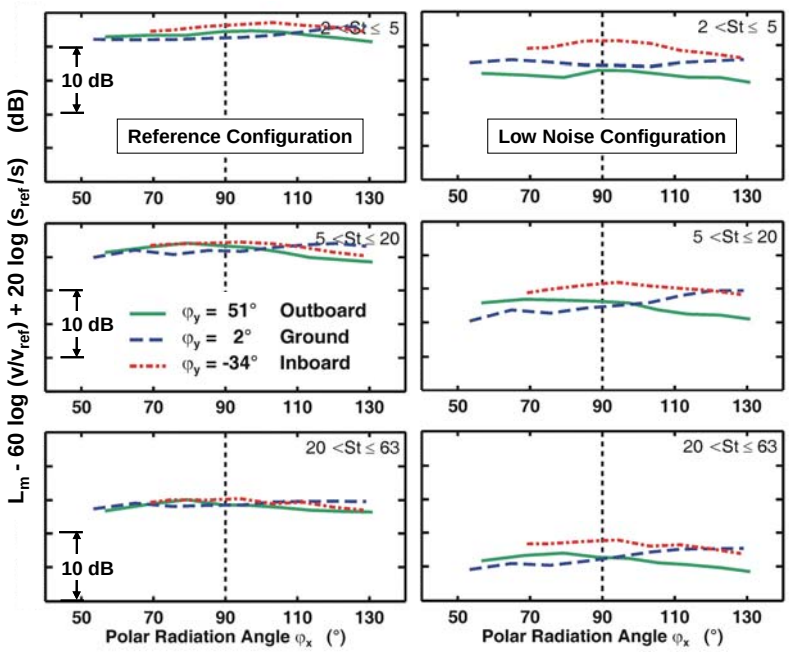

Figure 12. Polar directivities of non-dimensional 1/3-oct. band noise levels in different bands of Strouhal number for the SILENCER reference the TIMPAN low noise configurations and different azimuthal (sideline) radiation angles φ_y , respectively

configuration there is very little difference in the polar directivities for different sideline directions. However, differences show up for the quieter gear build as is presented in Fig. 12. It can be stated that the noise reduction obtained by this gear configuration is most pronounced for overhead ("ground") and outboard radiation directions, while the levels for inboard radiation direction remain relatively high. From the results as obtained for the variety of different gear configurations it turns out that this observation cannot be associated with any particular gear build but is specific for all relatively quiet configurations and thus supports the conclusion that the leg-door/ side-stay area is the remaining dominant source region compared to the bogie area for the SILENCER reference configuration. While the leg door shields noise to be radiated towards outboard directions, noise as generated by the various leg door construction details on the inboard side of the door can freely radiate in this direction. From these results it may also be concluded, that noise originating from the bogie area features an almost omnidirectional directivity, while noise from the leg-door structure is more directional.

Any efforts to further reduce the noise radiation from this gear design thus obviously must focus on the leg-door/ side-stay components. However, this skewness of the azimuthal radiation directivity is not considered a problem with respect to aircraft noise impact on the ground because the presented directivities are referenced to a constant radiation radius. In a flyover situation noise levels experience a geometrical damping for sideline directions which would amount to about 3 dB for a 45° azimuthal angle, thus compensating the observed "source" level increase shown in Fig. 12.

B. Noise Reduction Potential

The effectiveness of different noise reduction measures was determined through the computation of level differences from corresponding tests relative to a suitable reference configuration, i.e. the level difference from two gear configurations with one component change at a time.

From this exercise a rank order of noise reduction means' effectiveness is obtained, which however, to a limited extent suffers from the fact that not all these changes could be tested for the same reference configuration, meaning that a measure which was tested for a relatively noisy configuration will have a different effectiveness as it would have when tested on a relatively quiet configuration. Therefore no relevant rank order of priority can be provided. Still, some important general low noise design guidelines can be identified based on this procedure and will be discussed below.

3. Bogie and torque link fairings

The combined application of a bogie fairing and a torque link fairing (note: the torque link is installed in front of the gears' leg) seems to be a prerequisite for a low noise gear. It turned out that a porous design of both these fairings is an effective noise reduction feature. Fig. 13 depicts the individual effects on noise of these fairings for either a solid or porous make. For porous fairings, the flow displacement is significantly reduced while still achieving a low enough wake flow velocity.

In this context it should be mentioned that different wheel spacing did not have a notable effect on noise although this design parameter has some effect on the flow through the bogie structure.

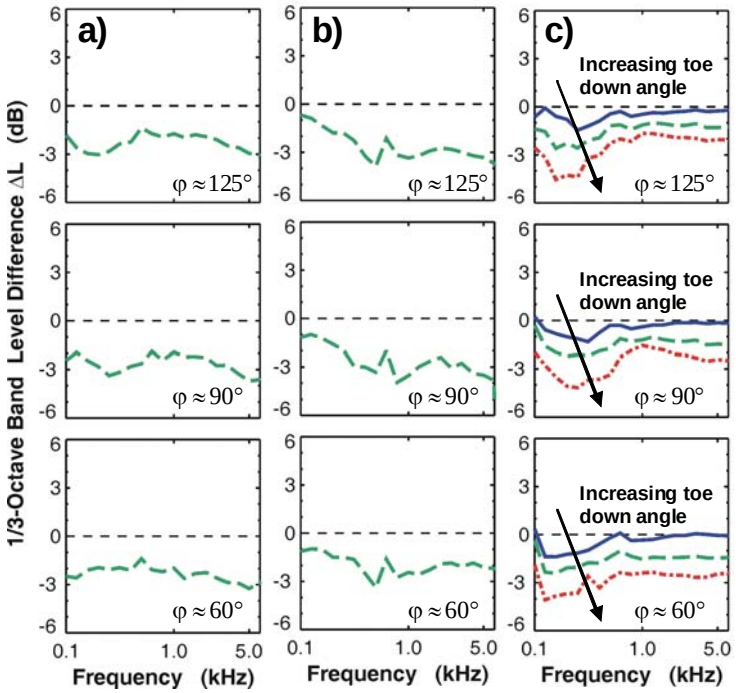

Figure 13. Effects of (a) porous bogie fairing and (b) porous torque link fairing w.r.t. solid fairings and (c) of bogie inclination angle

respect to noise. Such means are imperative because otherwise excess noise from the brakes will degrade the noise benefits from other noise reduction treatments.

6. *Leg-door/side-stay design*

The TIMPAN side-stay in combination with the articulated leg-door design turned out to be reasonably quiet but not as good as the SILENCER telescopic side-stay. This situation can significantly be improved by application of a ramp to reduce high frequency noise originating from the upper leg area and the side-stay joints and avoids flow interaction with the cavity aperture.

As a final result in this study the optimal combination of all tested gear modifications (see Section A for configuration details) provided a noise reduction of 8 dB(A) in terms of the OASPL (Overall Sound Pressure Level) compared to the noise signature of the SILENCER reference configuration. The highest noise reduction potential is achieved for high frequencies and forward arc radiation direction (Fig. 14). The latter is the most important radiation direction, because the effect of convective amplification will enhance the noise levels in this radiation direction once this "stationary source noise characteristic" will be transposed to flight conditions.

V. Noise Prediction

Prior to the tests predictions of some of the key configurations were made using a semi-empirical landing gear noise prediction model [13]. Carrying out predictions prior to testing is beneficial as it confirms that the tests will provide useful results and guides the priorities for the experimental programme. Comparing predictions with measured data after the test is obviously beneficial for validating the model, but also helps in interpreting and extrapolating from the data.

4. *Bogie inclination angle in combination with a bogie fairing*

A successive increase in toe down bogie angle led to a successive decrease in noise (see Fig. 13). However, the noise-wise optimal toe down bogie angle might not have been captured in TIMPAN. This parameter needs a dedicated optimization cycle, keeping in mind that the final optimal angle might only be relevant for the gear architecture under consideration. It is assumed that the effect on noise of this design parameter is due to a shielding effect of a front wheel bogie fairing with respect to the flow impact at the rear axle.

5. *Brake fairings*

The type of brake fairings tested in TIMPAN on partially recessed brakes are considered an optimal solution with

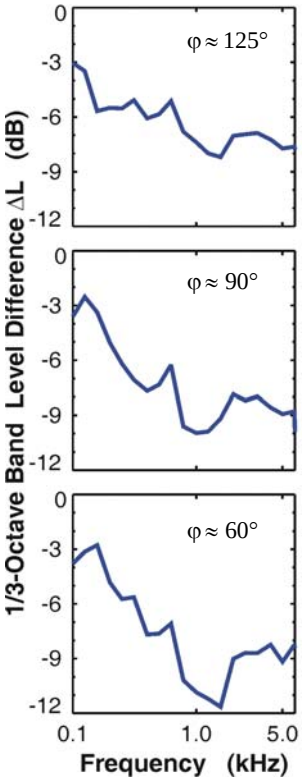

Figure 14. Noise reduction potential vs full scale frequency of the TIMPAN low noise configuration in comparison with the SILENCER reference configuration

The prediction model has been validated in a considerable number of previous tests, but a major difficulty here was that the gear modifications to be tested (e.g. variation of wheel layout and bogie angle, ramp fairing, etc.) were expected to cause major changes to the flow distribution. As no CFD predictions were available it was necessary to make a number of assumptions about the extent to which each modification either increased or decreased the local flow over each gear component, so for example it is known that the blockage from wheels increases the flow over the brakes which increases their importance as a source. Other assumptions included the following: Installing a porous fairing reduced flow over shielded components with no increase over other components; installing a solid bogie fairing shielded some components completely but also increased external flow over the wheels and mid-leg region; installing the ramp fairing shielded parts of the upper leg and side-stay but increased flow on some leg components.

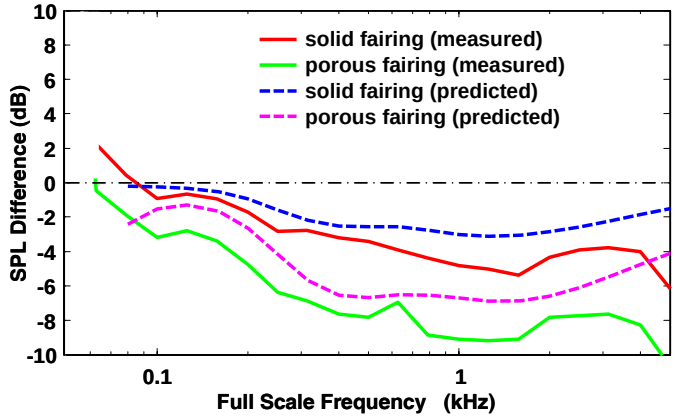

Figure 15. Predicted and measured effect of installing either a solid or porous bogie fairing and ramp fairing on the standard gear with the TIMPAN folding side-stay

On the basis of these assumptions Fig. 15 shows a comparison of the predicted and measured benefits of installing either a solid bogie fairing or a porous bogie fairing, combined with a toe-down bogie angle so as to ensure that components of the rear axle are shielded and also a ramp fairing to shield the upper leg. The reference build for this comparison comprises the standard advanced gear bogie combined with the new folding side-stay. The benefit of having a porous fairing rather than a solid fairing is fairly well predicted, and a key to this prediction is that a solid fairing significantly increases the flow over other components. Without this assumption the solid fairing would be predicted to be as effective as the porous fairing since they shield the same regions.

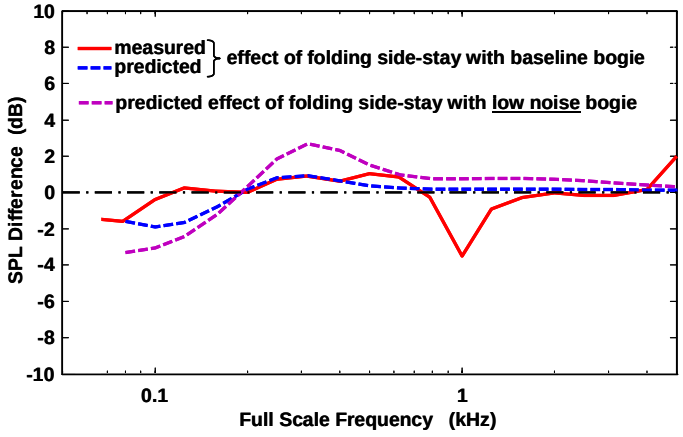

Figure 16. Noise increase due to changing from the SILENCER telescopic side-stay to the TIMPAN folding side-stay with the bogie in its reference configuration or its low noise configuration, respectively

The noise model may also be used to extend the range of the database by predicting builds that could not be included in the test program. So for example Fig. 16 shows the additional noise produced by changing from the telescopic side-stay to the TIMPAN folding side-stay when the bogie is either in its baseline configuration or is in its low noise configuration. The measured data confirm that this has only a small effect when the bogie is in its baseline configuration, but the prediction model shows by how much the relative importance of the side-stay is increased when the bogie noise is reduced, a characteristic that is borne out by Fig. 11.

VI. Transposition of Noise Data to Flight Conditions

Measured noise data were finally transposed to flight conditions to estimate the potential impact of the new main landing gear design on the noise certification level (Effective Perceived Noise Levels) in approach for a generic long range twin engine aircraft. The low noise main landing gear configuration evaluated in-flight combines the following features:

- -15° bogie angle (toe down),
- Narrow wheel spacing (both forward and rear wheel sets),
- Porous bogie and torque link fairings,
- TIMPAN brake fairings,
- Articulated TIMPAN door with 45° ramp and
- TIMPAN side-stay design.

The estimation of approach noise levels is based on Airbus' total aircraft noise prediction code, accounting for landing gear source noise reduction in terms of level differences obtained from the wind tunnel tests after transposition to full scale conditions. This prediction code has been validated previously through comparisons with flight test data [14]. The code predicts the levels from each airframe and engine noise source separately.

The following parameters have been taken into account to conduct noise impact calculations for a long range twin engine aircraft configuration as defined in TIMPAN:

- Landing gear configurations: A340 baseline reference landing gears or with SILENCER advanced nose and main landing gear design [10];
- Aircraft configuration: 23° slat, 32° flap and landing gears down;
- Conventional approach trajectory: –3° glide slope;
- Flight parameters: Speed V_C = 145 kts, aircraft angle of attack = 3°;

At this stage neither a potential impact on the aerodynamic aircraft performance nor on aircraft weight was taken into account for this noise estimation.

Fig. 17 presents the estimated impact on the EPNL for the TIMPAN low noise main landing gear design in comparison with the SILENCER advanced gear design and the A330/A340 baseline main landing gear design, respectively, on (i) main landing gear source noise level, (ii) total landing gear source noise level, (iii) airframe noise, and (iv) total aircraft noise level. Accordingly, A340 main landing gear noise is reduced by more than 7 EPNdB due to the TIMPAN low noise features. This corresponds to an additional 5 EPNdB noise reduction in comparison with the previously developed advanced SILENCER main landing gear design [10].

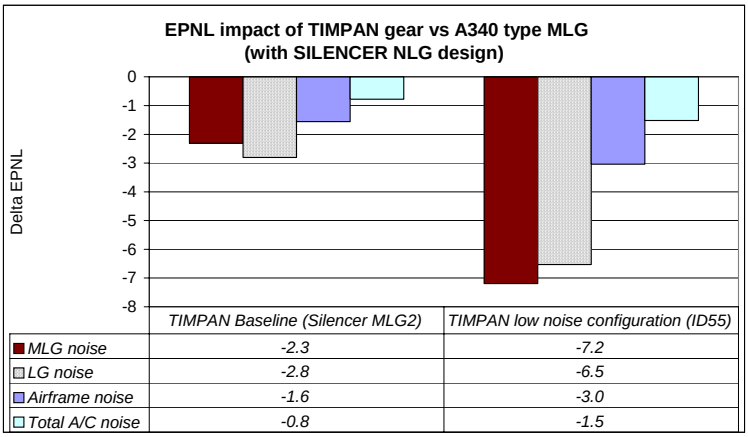

Figure 17. Impact on EPNL for approach conditions of the TIMPAN low noise main landing gear design vs the SILENCER gear design and the original A330/A340 gears, respectively

With TIMPAN low noise main landing gears the overall landing gear noise (including SILENCER nose landing gear design) is reduced by 6.5 EPNdB when compared to A330/A340 original landing gear noise levels. This demonstrates that the objectives of the TIMPAN research project to reduce landing gear noise levels by 6 EPNdB relative to the year 2000 technology has been achieved.

Finally, total aircraft noise can be reduced by 1.5 EPNdB in approach when applying the TIMPAN low noise features on A330/A340 main landing gears for otherwise identical noise levels related to both high-lift devices and the engines.

VII. Summary

In the European co-financed research project TIMPAN the "advanced low noise design" of an A340 type 4-wheel main landing gear, as developed in the former European SILENCER project, was further investigated with the objective to develop gear components which are as quiet or even quieter as the SILENCER design but with less weight penalty. A number of design options were developed to fit on the existing ¼ scale SILENCER advanced gear for noise testing in DNW-LLF. A variety of different gear configurations were tested for two wind speeds, respectively, including a new side-stay design, different modifications of bogie inclination (toe down), different wheel spacing, bogie fairings with different flow transparency, different leg-door and brake designs.

Acoustic farfield data were acquired for frequencies up to 40 kHz to account for the model scale factor. A comparison of normalized noise spectra and directivities as obtained for the SILENCER reference configuration at model scale with the spectra from the original SILENCER full scale test shows reasonable agreement.

An optimal combination of all tested gear modifications led to a noise reduction of up to 8 dB(A) in terms of overall A-weighted noise levels relative to the SILENCER reference gear configuration. The main contributions to this noise reduction originated from an increase in toe down bogie inclination angle, both a bogie and torque link porous fairing in combination with a low noise side-stay and brake design and an alternative leg-door design (re SILENCER) in combination with a ramp.

In contrast to the SILENCER reference configuration the polar noise directivity for the TIMPAN low noise configuration is characterized by maximum high frequency noise levels in the rear arc radiation direction. Source location with microphone arrays and supported by the analysis of sideline noise level directivities, proved the leg-door/ side-stay structure to represent the dominating noise source area for the TIMPAN low noise main landing gear configuration, while noise originating from the bogie area was dominating for the SILENCER reference gear configuration.

The test data are broadly in line with predictions made using a semi-empirical prediction model, although the use of this model is limited by the lack of accurate information about the changes in local flow over each component.

Finally, measured noise data were transposed to flight conditions to estimate the overall approach noise reduction for a generic long range aircraft. The TIMPAN low noise main landing gear configuration provides more than 7 EPNdB main landing gear source noise reduction, which results in a total aircraft noise reduction of 1.5 EPNdB for otherwise unchanged high-lift devices and engine noise levels.

Acknowledgments

The authors thank the staff of Airbus, BAE-Systems, Messier-Dowty, Messier-Bugatti and Southampton University for their efforts in manufacturing of landing gear components and their support during the test conduct. The acoustic data acquisition was prepared and conducted by DNW. The engaged support by the DNW project coordinator, Hermann Holthusen, is highly appreciated. Finally EC co-funding of this research project is also acknowledged.

References

[1]Dobrzynski, W. and Buchholz, H., "Full-Scale Noise Testing on Airbus Landing Gears in the German Dutch Wind Tunnel", *AIAA/CEAS 1997-1597*, Atlanta/USA, 1997.

[2]Stoker, R.W., "Landing Gear Noise Test Report", NASA Contract NAS1-97040, 1997.

[3]Dobrzynski, W., Chow, L. C., Guion, P., Shiells, D., "Research into Landing Gear Airframe Noise Reduction", *AIAA/CEAS Meeting Paper* 2002-2409, Breckenridge/CO, 2002.

[4]Ravetta, P.A., Burdisso, R.A. and Ng, W.F., "Wind Tunnel Aeroacoustic Measurements of a 26%-scale 777 Main Landing Gear Model", *AIAA/CEAS 2004-2885*, Manchester/UK, 2004.

[5]Abeysinghe, A. et al., "QTD 2 (Quiet Technology Demonstrator) Main Landing Gear Noise Reduction Fairing Design and Analysis", *AIAA/CEAS 2007-3456*, Rom/Italy, 2007.

[6]Remillieux, M.C. et al., "Noise Reduction of a Model-Scale Landing Gear Measured in the Virginia Tech Aeroacoustic Wind Tunnel", *AIAA/CEAS 2008-2818*, Vancouver/Canada, 2008.

[7]Smith, M.G. et al., "Control of Noise Sources on Aircraft Landing Gear Bogies", *AIAA/CEAS 2006-2626*, Cambidge/USA, 2006.

[8]Ravetta, P.A., Burdisso, R.A. and Ng, W.F., "Noise Control of Landing Gears Using Elastic Membrane-Based Fairings", *AIAA/CEAS 2007-3466*, Rom/Italy, 2007.

[9]Boorsma, K,, Zhang, X. and Molin, N., "Perforated Fairings for Landing Gear Noise", *AIAA/CEAS 2008-2961*, Vancouver/Canada, 2008.

[10]Dobrzynski, W. et al., "Design and Testing of Low Noise Landing Gears", *Journal of Aeroacoustics, Volume 5, Number 3, 233-262*, 2006.

[11]Amiet, R. K., "Correction of Open Jet Wind Tunnel Measurements for Shear Layer Refraction", *AIAA Meeting Paper* 75-532, Hampton, VA./USA, March 24-26, 1975.

[12]Bass, H. E., Sutherland, L. C., Zuckerwar, A. J., "Atmospheric Absorption of Sound: Update", *J. Acoust. Soc. Am. 88(4)*, pp. 2019-2021, Oct. 1990.

[13]Smith, M. G. and Chow, L. C., "Validation of a Prediction Model for Aerodynamic Noise from Aircraft Landing Gears", AIAA/CEAS 2002-2581, Breckenridge/USA, 2002.

[14]Molin, N. et al, "Prediction of low noise aircraft landing gears and comparison with test results", *AIAA/CEAS 2006- 2623*, Cambridge/USA , 2006.

Bluff Body Noise and Flow Control with Atmospheric Plasma Actuators

Xun Huang* Xin Zhang† and Steve Gabriel‡

University of Southampton, Southampton, SO17 1BJ, United Kingdom

Plasma actuators operating in atmospheric air were employed to modify aerodynamic flow over a bluff body. The model consisted of a cylinder and a strut that was installed on the trailing half side of the cylinder. The objective was to reduce the broadband noise that is mainly generated by the impingement of the cylinder wake on the strut. The plasma actuators were configured to produce dielectric barrier discharges, through which the flow separation from the cylinder was enhanced. As a result the wake-strut interaction was reduced, leading to the attenuation of broadband noise. The noise and flow control performance with the plasma actuators were studied in an anechoic chamber facility as well as a wind tunnel facility by examining sound pressure and mean flow field respectively. With the current plasma actuators, it was found that there was 1 dB reduction in overall sound pressure level at a free stream speed of 30 m/s, and the wake speed impinging on the strut was reduced. A possible solution to improve the broadband noise attenuation performance is discussed at the end of this paper.

I. Introduction

THE high level of nuisance noise generated by the take-off and landing of aircraft has a significant impact on the communities near airports.[1] With a reduction target of perceived noise level of 50% by 2020,[2] various control techniques have been tested to attenuate aerodynamically generated noise. Plasma actuators, operating in atmospheric pressure air condition, hold the potential to reduce flow-induced noise through modifying aerodynamic flow field. Some recent work[3–6] have demonstrated the potential of using the dielectric barrier discharge (DBD) plasma actuators[7] to attenuate the tonal noise of a cavity that is similar to a landing gear bay.

Dielectric barrier discharge plasma actuators are able to generate weakly ionized atmospheric plasma, which is coupled to an electric field thus inducing body force that affects the flow field local to the plasma actuators.[8–12] In addition to a high alternating current (AC) power supply, a plasma actuator system consists of a pair of copper electrodes, between which a dielectric material is placed to prevent electric arching. The voltage applied to the electrodes operates at O(kHz) frequency to sustain the glow discharge. The simplicity and absence of mechanical moving parts, *e.g.* pumps, make the plasma actuator a promising option for aerospace applications. In this work the DBD plasma actuators were applied to a bluff body, which is an idealised model of the main leg part of a landing gear. The same type of plasma actuators were applied on a single cylinder at Reynolds number from 1×10^4 to 4×10^4 previously[10,13] to control wake flow and suppress vortex shedding.

In the previous cavity experiments, the plasma actuators attenuated flow-induced tonal noise through either manipulating shear layer[3–5] or generating disturbances at off-resonant frequency.[6] The amplification of the flow system at the normal resonant frequency is consequently suppressed. Rather than tonal noise attenuation, the interest of the present investigation is focused on broadband noise attenuation. The plasma actuators were designed and installed on the surface of the bluff body model. The flow around the model was manipulated by the externally applied body force. Through modifying the wake flow behind the model, the flow induced noise at broadband frequency range was expected to be reduced. The effectiveness of the noise attenuation by the plasma actuators was firstly studied by performing far field acoustic measurements in an anechoic facility. Both sound pressure level (SPL) and overall sound pressure level (OASPL) were examined. To provide insight into the noise control mechanism from aerodynamic side, the natural and forced flow fields were subsequently measured and visualised by particle imaging velocimetry (PIV) in a low speed wind tunnel. The next two sections describe the experiments and discuss results. A summary of the present work is provided at the end of the paper.

*Lecturer, Aeronautics and Astronautics, School of Engineering Sciences. AIAA Member.

†Professor, Aeronautics and Astronautics, School of Engineering Sciences. Associated Fellow AIAA.

‡Professor, Aeronautics and Astronautics, School of Engineering Sciences.. AIAA Member.

II. Experimental Methods

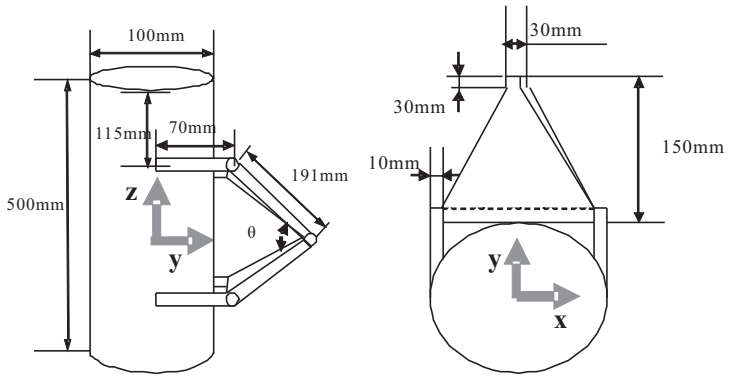

Figure 1. Schematic of the model.

The bluff body tested in this work is a simplified model of bogie beam parts installed on a landing gear, including a cylinder and a strut. The former one corresponds to the main leg of the landing gear, and the latter one corresponds to the torque link of the landing gear. The diameter of the cylinder is 100 mm. The height of the cylinder is 500 mm. The angle θ of the torque link is 45 deg. Additional geometry information of the model, along with the coordinates employed in the PIV measurements, are given in Figure 1. The origin of the coordinates is on the center point of the cylinder.

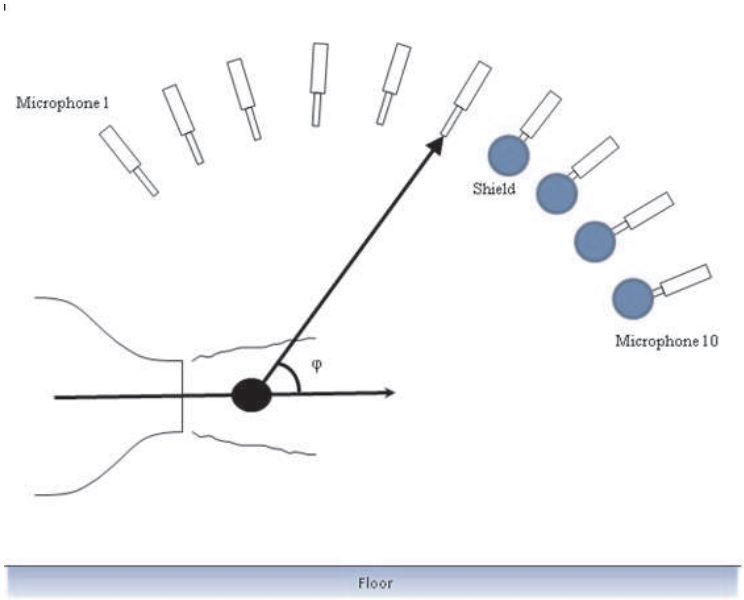

Figure 2. Far field acoustic measurement in an anechoic facility.

The model was tested in an anechoic chamber to examine its far field acoustic properties. Figure 2 shows the testing units in the anechoic chamber. There are 10 microphones installed on an arc that is approximately 2 m away from the model. The elevation angle ϕ of each microphone is 115, 105, 95, 88, 78, 68, 55, 48, 38, 30 deg, respectively. The last four microphones were covered by shields to alleviate the wake effect on acoustic measurement. For each microphone the lowest sensitive frequency is 20 Hz and the highest one is 20 kHz; the sensitivity is -44 ± 5 dB (0 dB$= 1$ V/pa at 1 kHz); the signal-to-noise ratio is more than 58 dB. The microphones' output was passed through preamplifiers and anti-aliasing filters and subsequently was sampled with a data acquisition system produced by National Instruments at 44.1 kHz. A 4096 point fast Fourier transform with a Hanning window function was applied to the sampled data. The spectral results were averaged over 50 signal blocks for statistical confidence.

A nozzle connecting to the plenum chamber can produce a jet flow with the speed up to 30 m/s in the experiments. Reynolds number is up to 2.1×10^5 based on the cylinder diameter. The bluff body model was installed 300 mm down-

stream of the nozzle exit. The power supply of the plasma actuators was located in a separate room to prevent its cooling fan noise from polluting the sound measurements in the anechoic chamber facility. The AC voltage at O(kV) was applied to the plasma actuators via a 20 m length high voltage cable, whose impedance is unknown. As a result, the impedance matching network of the power supply worked inefficiently. For the present configuration the plasma actuators performed efficiently at 6 to 7 kHz with the most uniform and the brightest plasma, which normally corresponds to the maximal body force. To use the plasma actuator at higher frequency beyond 20 kHz, which is outside of the frequency range of human hearing, a new impedance matching network should be designed according to the impedance values of the power supply, cables and the plasma actuators. This can be solved as soon as the plasma actuator design scheme is finalized.

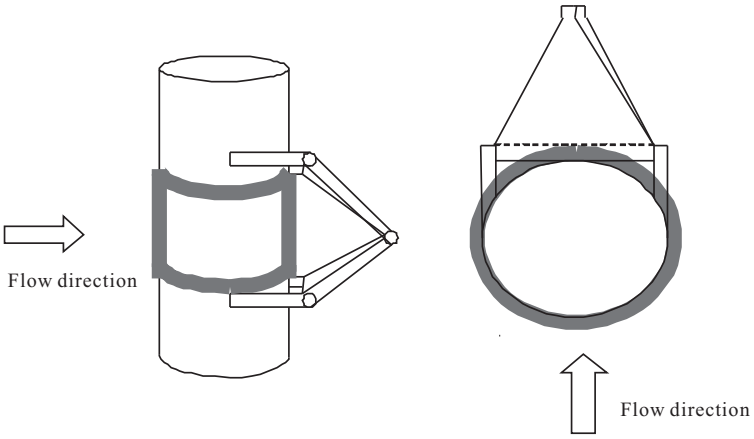

Figure 3. Side view and ceiling view of a passive flow control on the model.

Figure 3 shows a passive flow control method that was implemented by covering the cylinder surface with rubber material, whose thickness is 5 mm that reduces the interaction between the strut and the cylinder wake. Compared to the baseline case without the rubber, the width of the wake is increased that subsequently leads to reduced flow strength impinging on the strut. As a result, the sound generated in the wake-strut interaction is attenuated. Figure 4 shows far field SPL results obtained by a single microphone in the anechoic chamber facility. It can be seen that the SPL at the broadband frequency range (from 1 to 10 kHz) were reduced by up to 10 dB. The noise reduction, however, is small when the rubber thickness is less than 3 mm.

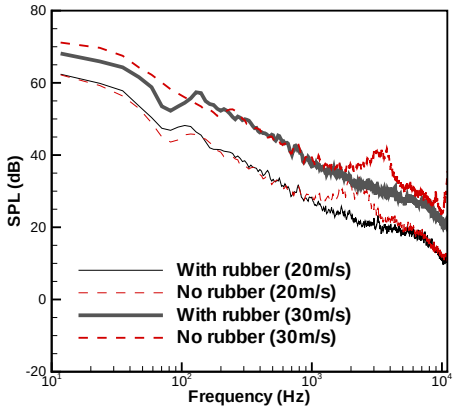

Figure 4. Sound level reduction by the passive flow control method.

Although the passive control method works effectively, the attention is focused on active control methods with the plasma actuators to avoid the need to change the aerodynamic surface extensively. The plasma actuators were designed and produced by flexible printed circuit board (PCB) technology to cover the whole cylinder surface. Kapton is the general dielectric material used in commercial flexible PCB production. The thickness of the Kapton material is 0.5 mm that is selected for its flexibility and for preventing electric breakdown. In the experiments the AC power supply with up to 20 kV peak-to-peak voltage (V_{pp}) was applied to the plasma actuators. More details of the AC power supply and the

plasma actuators can be found in literatures.[3–6]

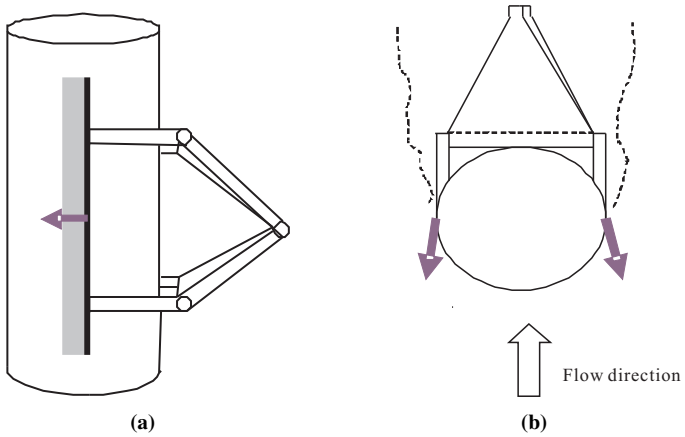

Figure 5. Schematic of the plasma actuator installed on the model.

Figure 5 shows the plasma actuator installed on the model. The plasma actuator consists of two pairs of electrodes, which are installed at $\Omega = 0$ and 180 deg (ω is showed in Figure 1). Other configurations were also extensively tested. It was found that the installation angles slightly below 0 and above 180 deg were also good. However, the installation angles between 0 and 180 deg were found to be less efficient for wake flow control. In Figure 5 the black line denotes the top electrodes exposed to air. The gray lines denote the bottom electrodes that are insulated from the top electrodes and the aluminium model surface by two layers of Kapton material, which is not shown in Figure 5 for simplicity. The overall thickness of the plasma actuator is 1 mm. The arrows in Figure 5 indicate the body force direction that is tangential to the model surface. Under the current configuration with the upstream actuation, the separation from the cylinder was expected to be enhanced, leading to reduced wake-strut interaction. On the other hand, downstream actuation can reduce the width of the wake from a single cylinder[10] and suppress the vortex shedding. The downstream actuation was therefore presumed to increase wake impinging on the strut and thus not a preferable solution for the present investigation.

To study the flow changes due to plasma actuation, PIV measurements were conducted in a low speed wind tunnel facility at the University of Southampton. The wind tunnel is of a closed jet, open loop design. The maximum flow speed attainable in the working section of the tunnel is 30 m/s. The working section has a uniform cross section that measures 0.9 m wide $\times 0.6$ m high. The PIV system used in the experiments is a product of Dantec Measurement Systems and incorporates two Gemini Nd:YAG lasers by New Wave Research that are capable of running at 4 Hz emitting 120 microjoule pulses at 532 nm. A Dantec HiSense (type 13 gain 4) 1024×1289 resolution charged coupled device camera was used to capture flow field of $x - y$ plane at different z value, in double frame mode for image capture. The lenses available were a Nikon Nikkor 24 mm f/2.8 lens and a Nikon Nikkor 60 mm f/2.8 lens. To provide seeding for the flow a Safex S195G smoke seeder using Regular DJ Mix Fluid by Marin Professional was used. The typical size of the non-spherical particles is $2\,\mu$m in diameter. The particles provided suitable tracer material that was homogeneously distributed into the flow. The seeder was placed in the same room as the wind tunnel and care was taken so that the presence of the seeder would not interfere with the flow around the wind tunnel. Image correlations were performed using Dantec's FlowManager to obtain velocity vectors. Typically image sets were processed using an adaptive correlation with a minimum pixel sized interrogation area of 16×16 with a $75\% \times 75\%$ overlap to improve the resolution of the vector map. The processing technique produces a vector map containing up to 317×253 vectors. Inevitably spurious vectors arise as a result of the finite number of tracer particles in the flow, excessive particle displacements, insufficient resolution or even poor image quality. The method for removing these spurious vectors is by using a range validation whereby vectors that are greater than a specified magnitude would be rejected. To produce the time-mean flow, 200 instantaneous vector maps were generated from images collected with 2 Hz sampling rate.

III. Results

To quantitatively compare the noise control performance, SPL results obtained in the anechoic chamber tests were examined. A fixed testing procedure was followed. Firstly, the actuators were installed on the intended test position; secondly, the acoustic data were collected without plasma actuation; finally, the acoustic data were acquired with plasma actuation. The procedure was repeated at different flow speeds and voltages (V_{pp}). Normally, higher voltage led to better

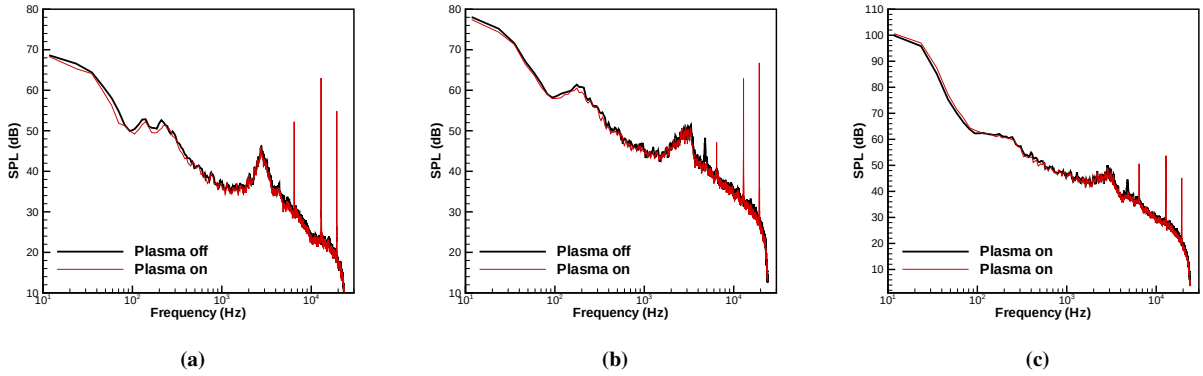

(a) (b) (c)

Figure 6. SPL results of microphone 2, 6, and 9.

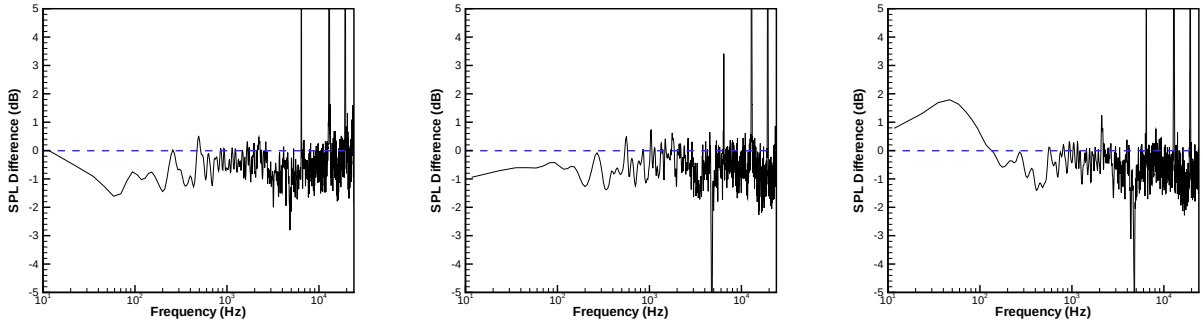

(a) (b) (c)

Figure 7. SPL differences of microphones 2, 6, and 9, where the SPL difference is the SPL value with upstream plasma actuation minus the SPL value without plasma actuation.

control performance. However, the plasma actuators could be broken down by V_{pp} above 20 kV.

Figure 6 shows SPL results of three microphones at $U_\infty = 30$ m/s and $V_{pp} = 15$ kV. To illustrate the noise control performance clearly, the difference between the SPL values with/without plasma actuation is given in Figure 7, where the negative value denotes noise reduction due to plasma actuation, and vice versa. It can be seen that with the upstream actuation, there are broadband noise reduction recorded at microphones 2 and 6. Similar discovery was found in SPL recorded at microphones 1 to 7. However, there is up to 2 dB increase in the low frequency range recorded at microphone 9, which is almost in the wake flow. Microphone 10 is also immersed in the wake flow and produces the similar results. The results from microphone 9 and 10 suggest that, due to the upstream actuation, the wake is more turbulent that produces more noise in low frequency range. On the other hand, the results from microphone 1 to 7 imply that there is a broadband noise reduction outside the wake flow area. It is also worth noting that better noise reduction performance was obtained at a lower speed of $U_\infty = 20$ m/s. In addition to the broadband noise reduction, the plasma actuator also radiates tonal noise at its driving frequency and harmonics. The undesirable sound effect can be removed by increasing the driving frequency beyond 20 kHz with modified impedance matching network, which should be designed as soon as the specifications of the plasma actuator, power supply and cables are finalized for the desired application.

1/3 octave band spectrum results for the data recorded at microphones 2, 6, and 9 are showed in Figure 8. The frequency band is from 125 to 5000 Hz, set below the plasma driving frequency (6.5 kHz) to avoid its negative impact on the 1/3 octave band averaged results. To show the control effect clearly, the difference of 1/3 octave band spectrum with/without the plasma actuation is showed in Figure 9. It can be seen that noise attenuation is up to 1.5 dB, and is most effective in the frequency ranges below 100 Hz and above 2500 Hz for microphone 1 to 7. The noise attenuation effect in the low frequency range for microphones 9 and 10, however, is reduced.

During the test, although all circuits were shielded to prevent electromagnetic interference from plasma discharges,

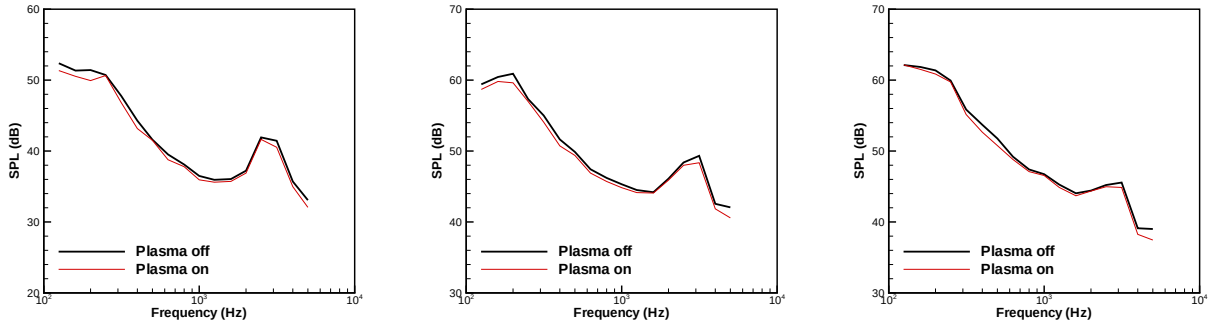

(a) (b) (c)

Figure 8. 1/3 octave band spectra results of microphones 2, 6, and 9.

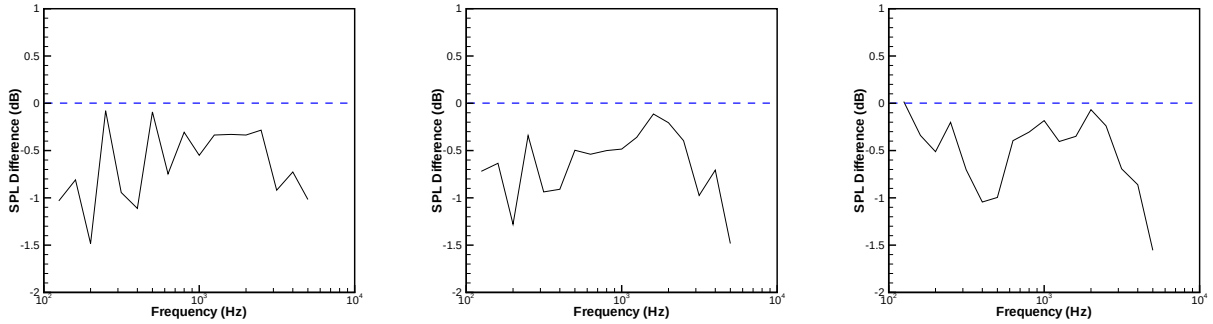

(a) (b) (c)

Figure 9. 1/3 octave band spectra differences of microphone 2, 6, and 9.

the data recorded at microphone 8 was still corrupted and is not used here. In addition, the last microphone in the arc (microphone 10) was immersed in the wake and produced much higher SPL in low frequency range under the plasma actuation, leading to the OASPL increase rather than a reduction. Here only results recorded at microphones 1 to 7 and microphone 9 under upstream plasma actuation are showed in polar coordinates in Figure 10, where the OASPL reduction values are indicated on the radius axis, and the elevation angle of each microphone is on the angle axis. To avoid the inclusion of the plasma radiation noise in the OASPL computation, the frequency range from 125 to 5000 Hz was considered again. It can be seen that, except at microphone 9, the OASPL reductions at all other microphones are about 1 dB.

The sound reduction with the upstream actuation was presumably caused by reducing the wake impinging on the strut. To provide further insight into physics, the time-mean flow results obtained by the PIV measurements were examined. Figure 11 compares the mean velocity U in the x direction with/without the plasma actuation. Two different lines in the observed plane are compared. The first line is normal to the joint that connects the cylinder and the strut. The second line is normal to the strut. The specific coordinates of the two lines are: $y = 16\,\text{mm}$, $z = 135\,\text{mm}$; and $y = 120\,\text{mm}$, $z = 80\,\text{mm}$. Figure 11 shows that U velocity with the plasma actuation is larger than U velocity without the plasma actuation, implying that the wake impinging on the strut could be reduced under the upstream plasma actuation. The PIV measurements were on the joint of the strut at $y = 180\,\text{mm}$ and $z = 0\,\text{mm}$, where little difference in U was found. It implies that the plasma actuation just works effectively on flow field local to the plasma actuators.

Two-dimensional mean flow field results on the $x - y$ plane at $z = 80\,\text{mm}$ are showed in Figure 12. A white coloured block in Figure 12(b) excludes an imperfection area of the sampled flow. The dashed lines in Figure 12(a) and Figure 12(c) denote the laser sheet positions on the strut, on which the wake is supposed to impinge. Compared to Figure 12(a), Figure 12(c) shows that the impinging was reduced with the upstream plasma actuation. On the other hand, Figure 12(b) and Figure 12(d) show that V velocity in the y direction was affected little by the upstream actuation.

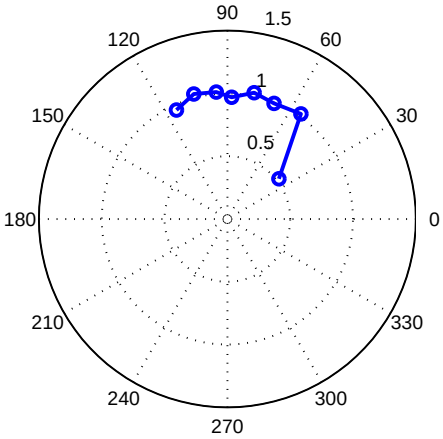

Figure 10. OASPL reduction due to the plasma actuation.

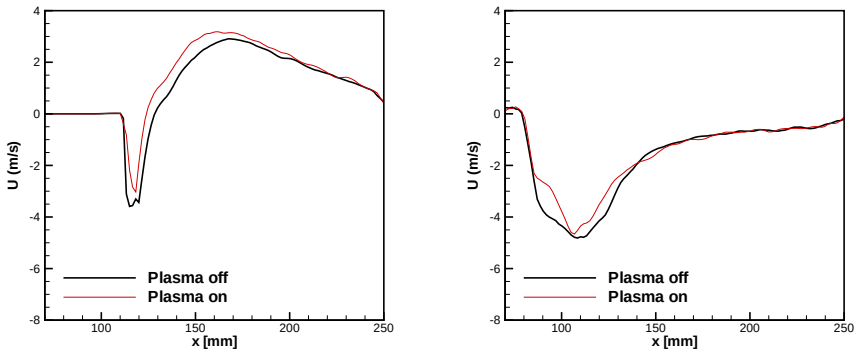

(a) **(b)**

Figure 11. The velocity U in the x direction at: (a) $y = 16$ mm, $z = 135$ mm; and (b) $y = 120$ mm, $z = 80$ mm.

The preliminary results suggest that the flow separation on the bluff body is enhanced by using upstream plasma actuation. It was found that the flow separation enhancement was reduced along with the increase of the free-stream speed. For example, the changes in the aerodynamic field at 30 m/s were not so distinctive as the changes at 20 m/s. Compared to the noise control results by the passive control method (Figure 4), the active control results reflect the fact of the limited authority of the current plasma actuators, which generate an ionic wind of approximately 4 m/s at 1 mm above the dielectric surface according to the previous measurements. In this work the Kapton material was selected for the easy production of the plasma actuators by employing commercial flexible PCB technique. It was found that the induced ionic wind speed can be up to about 8 m/s if the Kapton dielectric material was replaced with 1 mm thickness silicon rubber, where, however, the electrodes of the plasma actuator have to be positioned manually. To better attenuate noise from the bluff body, new actuators based upon silicon rubber will be produced and tested next.

IV. Summary

The aim of this experimental investigation was to investigate the broadband noise attenuation potential of upstream plasma actuation on a bluff body. The plasma actuators were applied to the bluff body surface at free-stream speed up to $U_\infty = 30$ m/s. Both far field microphone measurements in an anechoic chamber facility and PIV surveys of turbulent

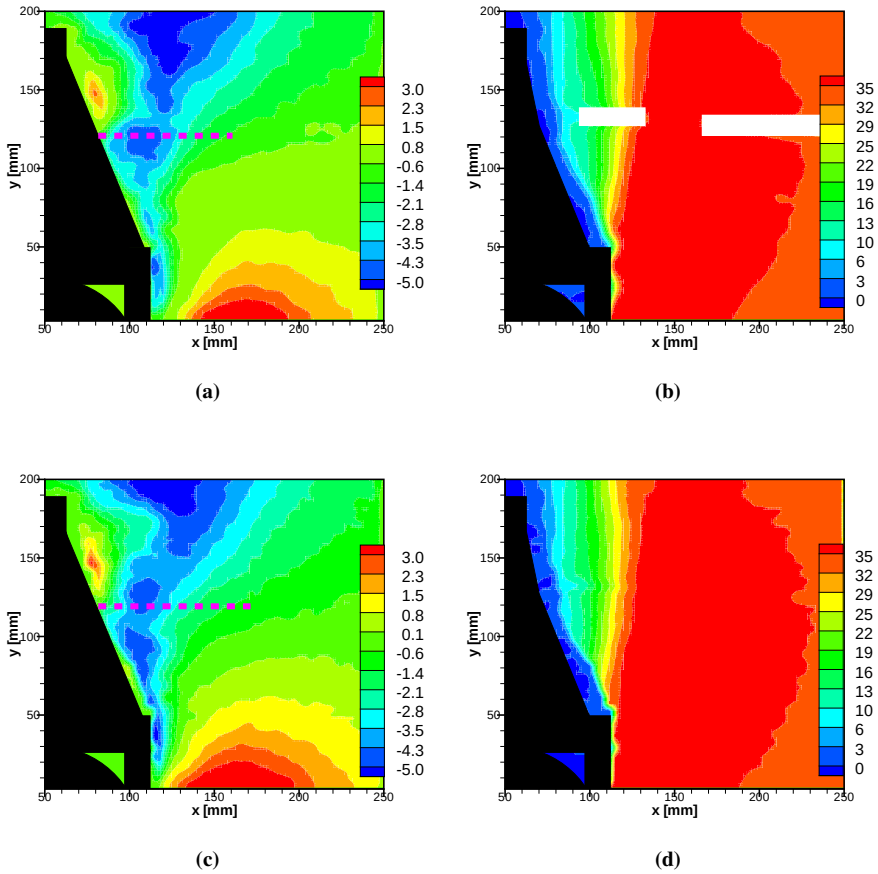

Figure 12. The velocity field, where (a)-(b): without plasma actuation, (c)-(d): with upstream actuation, (a),(c) is U in the x direction, and (b), (d) is V in the y direction.

wake flow in a low speed wind tunnel facility were performed. The microphone measurements show that the far field OASPL values at broadband frequency range can be reduced by about 1 dB with the upstream plasma actuation. Rather than suppressing vortex shedding that generates the tonal noise components in the noise spectrum, the broadband noise reduction is achieved by affecting the interaction between the cylinder wake and the strut. This observation is supported by flow field measurements using PIV. The flow field results local to the junction of the cylinder and the strut, and on the strut were examined by PIV. It can be seen that the speed of the wake impinging on those places is reduced. The same finding was also recorded at other places local to the strut. To further reduce noise, additional wake-strut interaction attenuation should be achieved by increasing the plasma actuator performance. The work is ongoing and beyond the scope of this paper.

Compared with other alternatives, the plasma actuators have many merits, including: simple and cheap implementation of the plasma actuator, direct installation of the plasma actuators on aircraft structure surface and thus impose small effect on overall structure, and rapid time response.

Acknowledgments

This work was supported by TIMPAN (Technologies to IMProve Airframe Noise) project, which is co-funded by the European Commission within the sixth Framework Programme (2002-2006). We would like to acknowledge Stephen Chow of Airbus for helpful discussions.

References

[1]Raman, G. and McLaughlin, D. K., "Recent aeroacoustics research in the United States," *Noise & Vibration Worldwide*, Vol. 31, No. 10, 2000, pp. 15–20.

[2]for Aeronautics Research in Europe, A. C., "Strategic Research Agenda," Vol. 1 and 2, 2002.

[3]Chan, S., Zhang, X., and Gabriel, S., "The attenuation of cavity tones using plasma actuators," *AIAA Journal*, Vol. 45, No. 7, 2007, pp. 1525–1538.

[4]Huang, X., Chan, S., and Zhang, X., "An atmospheric plasma actuator for aeroacoustic applications," *IEEE Transactions on Plasma Science*, Vol. 35, No. 3, 2007, pp. 693–695.

[5]Huang, X., Chan, S., Zhang, X., and Gabriel, S., "Variable structure model for flow-induced tonal noise control with plasma actuators," *AIAA Journal*, Vol. 46, No. 1, 2008, pp. 241–250.

[6]Huang, X. and Zhang, X., "Streamwise and Spanwise Plasma Actuators for Flow-Induced Cavity Noise Control," *Physics of Fluids*, Vol. 20, No. 3, 2008, pp. 037101–1–037101–10.

[7]Roth, J. R., "Aerodynamic flow acceleration using paraelectric and peristaltic electrohydrodynamic effects of a one atmosphere uniform glow discharge plasma (OAUGDP)," *Physics of Plasmas*, Vol. 10, No. 5, 2003, pp. 1166–1172.

[8]Roth, J. R., "Electrohydrodynamically induced airflow in a one atmosphere uniform glow discharge surface plasma," *IEEE International Conference on Plasma Science*, , No. 6P-67, June 1998.

[9]Roth, J. R., Sherman, D. M., and Wilkinson, S. P., "Electrohydrodynamic flow control with a glow-discharge surface plasma," *AIAA Journal*, Vol. 38, No. 7, July 2000, pp. 1166–1172.

[10]Thomas, O. F., Kozlov, A., and Corke, C. T., "Plasma Actuators for Landing Gear Noise Reduction," AIAA Paper 2005-3010, 2005.

[11]Sung, Y., Kim, W., Mungal, M. G., and Cappelli, M. A., "Aerodynamic modification of flow over bluff objects by plasma actuation," *Experiments in Fluids*, Vol. 41, 2006, pp. 479–486.

[12]Moreau, E., "Airflow control by non-thermal plasma actuators," *J. Phys. D: Appl. Phys.*, Vol. 40, 2007, pp. 605–636.

[13]Forte, M., Jolibois, J., Pons, J., Moreau, E., Touchard, G., and Cazalens, M., "Optimization of a dielectric barrier discharge actuator by stationary and non-stationary measurements of the induced flow velocity: application to airflow control," *Experiments in Fluids*, Vol. 43, No. 6, 2007, pp. 917–928.

An experimental investigation of a gapless high-lift system using circulation control

K. C. Pfingsten, R. D. Cecora and R. Radespiel
Institute of Fluid Mechanics (ISM), Technische Universität Braunschweig
Bienroder Weg 3, 38106 Braunschweig, Germany
K.C.Pfingsten@gmail.com

Abstract

When air is blown from a slot directly upstream of a flap, the flow over the flap can bear large adverse pressure gradients without separation. This effect is used to design high-lift airfoils with low momentum coefficients of blowing. For experimental assessment of these airfoils a rectangular wing with an aspect ratio of 4.3 was built. The flow around the model in a low speed wind tunnel is analysed using pressure measurements and long distance microscopic particle image velocimetry. To measure the velocity in the vicinity of the slot and next to the surface of the flap the jet is seeded with particles. For Reynolds numbers of about $\mathrm{Re} = 1 \cdot 10^6$ the dimensionless momentum coefficient of the jet and the angle of attack of the airfoil are varied. Numerical simulations of the three-dimensional flow around the circulation control airfoil in the wind tunnel are compared to the experimental data. Good agreement is observed in terms of pressure distributions and velocity profiles.

1 Introduction

In recent years noise pollution from aircraft, especially around airports, has become a huge problem. Hence there is an increasing interest in reducing the noise emitted during take off and landing. The conventional high-lift systems, consisting of slats and slotted flaps, are a major contributor of airframe noise. Therefore a gapless high-lift system without slats has a potential of reducing the overall noise emitted by an aircraft. With active flow control a gapless high-lift device is capable of generating the high lift coefficients needed for climb and landing. For circulation control a small fraction of the cold engine flow is used for blowing. The bleed air is pipelined from the engine to a slot directly upstream of the flap and thus the flow over the flap can bear large adverse pressure gradients without separation. Thus a gapless high-lift device with circulation control can generate the required lift. The low drag coefficients during climb-out, achievable with this powered high-lift system, could also allow for new low-noise trajectories, which would further reduce noise impact on the ground. The absence of slats might allow for laminar flow conditions in cruise flight, thereby reducing the drag in this flight segment. Even taking into account the additional system weight associated with the bleed air distribution for a gapless high-lift system, there is a chance of reducing the total weight of the aircraft and possibly the cost, because slats and fowler systems are no longer needed.

The first experiments using blowing to improve lift were conducted in the thirties of the last century by Bamber [1] as well as Hagedorn and Ruden [2]. Circulation control was first proposed for the flow over a circular cylinder by Davidson [3] and then applied to elliptical airfoils by Kind and Maul [4]. Elliptical airfoils utilising circulation control were also investigated by Stevenson et al [3] and Novak et al [6]. At Technische Universität Braunschweig systematic measurements and theoretical considerations for wings with blown flaps by Thomas [7] and Körner [8] yielded lift increase versus necessary momentum coefficients. The elliptical airfoil with circulation control as well as the internally blown flap were extensively investigated by Englar [9] who could demonstrate good lift-over-drag performance. The first aircraft to demonstrate the high-lift capability of circulation control was a technology demonstrator built by Loth [10]. An experimental investigation using particle image velocimetry to assess the flow around a circulation control airfoil with an elliptical trailing edge as well as the flow around an airfoil with a flap was conducted by Jones et al [11]. These configurations were assessed numerically by Baker and Paterson [12] using two-dimensional RANS simulations. Large-eddy simulations for an elliptical profile with circulation control were performed by Slomski et al [13].

Due to the promising results of preceding numerical simulations by the authors [14] further experimental investigations were conducted to analyse an airfoil with circulation control [15]. As in the preceding exper-

iments the jet was not seeded with tracer particles, the velocity in the jet could not be measured. In the experiments discussed here, the jet flow is seeded to measure the velocity profiles in the vicinity of the slot and on the flap surface using long distance microscopic particle image velocimetry. The special requirements for long distance μPIV are discussed by Kähler et al [16]. Simultaneously, numerical simulations of the wind tunnel experiments are performed. The experimental and numerical results are compared to assess the ability of the used flow solver to simulate the flow around an airfoil with circulation control.

2 Coanda Effect

Profiles with blowing close to the trailing edge use the well known Coanda principle to generate high lift coefficients. If a jet is positioned close to a wall, pressure forces change the path of the fluid elements. Thus the jet is deflected to the surface and becomes a tangential wall jet. The reason for this behaviour is low pressure between the jet and the solid surface. Due to the momentum transport from the jet to the stationary or slowly moving fluid, the flow in the vicinity of the jet is accelerated. Since the wall prevents fluid inflow into the area between the jet and the wall, pressure decreases. The emerging pressure gradient normal to the wall generates a force, which moves the jet flow towards the wall. This effect applies for jets along straight and curved walls and hence tangential blowing can be used to achieve large turning of the flow over airfoils.

Investigations by Englar and Hemmerly [17] showed that the Coanda effect works best when the slot height is about 1% to 5% of the curved surface radius and the slot height is about one to two per mil of the chord length.

The driving parameter for the Coanda effect is the dimensionless momentum coefficient, c_μ, of the jet, which is defined as follows:

$$c_\mu = \frac{v_{jet}\ \dot{m}_{jet}}{\frac{1}{2}\,\rho_\infty\, v_\infty^2\, S}$$

It is important to notice that the increase of the lift coefficient is much higher than the used dimensionless momentum coefficient. So the lift gain is due to flow separation control and super circulation and does not arise because the momentum of the jet is directed downwards.

3 Model Design for Wind Tunnel Experiments

Numerical two-dimensional simulations of the flow around profiles using circulation control were conducted to find favourable geometries with low momentum coefficients. The flow around the circulation control profiles was simulated by solving the Reynolds-averaged Navier-Stokes equations using the DLR hybrid unstructured flow solver TAU, which is based on a finite volume scheme [19, 20]. The code processes meshes with different types of cells and combines the advantages of structured grids to resolve boundary layers with the flexible grid generation of unstructured grids. To accelerate the convergence to steady state, techniques like local time stepping, residual smoothing and multi grid based on agglomeration of the dual-grid volumes are available. All preliminary two-dimensional computations were undertaken assuming the boundary layer to be fully turbulent and with the Spalart-Allmaras [21] turbulence model, which has proven its general capability of computing the flow fields around profiles with circulation control, using simulations of the experimental results achieved by Novak [6] for an elliptical profile with circulation control [22, 23].

As a starting point for two-dimensional investigations of circulation control a modern transonic airfoil was chosen, which can be seen in **Figure 1**. The design of the profile with circulation control has been done in a way to retain the characteristics of the basic profile at cruise conditions. First the x-wise position of the slot is defined, which also determines the length of the flap. Thus the slot is positioned directly upstream of the flap. Upstream of this position the original upper surface is used. Downstream of the slot the upper surface of the flap has to be defined. The results of the numerical two-dimensional simulations for different flap geometries were previously published by the authors [15].

For the wind tunnel tests the upper surface of the flap downstream of the vertical slot is defined as shown in **Figure 2**. The length of the large high-lift flap is set to $c_{flap}/c = 0.3$. This geometry is selected for the following reasons: With the large high-lift flap large lift coefficients can be generated for a given momentum coefficient and even when the blowing fails, reasonable lift coefficients can still be achieved. Low momentum coefficients are here assumed as the most important requirement. When the Coanda radius is hidden in the profile during cruise flight conditions the circulation control profile and the basic airfoil are identical. If the flap is deflected for take off and landing, the Coanda radius appears downstream of the slot. The exact

position of the hinge line can be used to obtain continuity in surface slope. This feature is not shown in **Figure 2**.

Note that by doubling the slot height the generated lift is only slightly increased. Therfore here a profile with a small slot height such as $h/c = 0.001$ is preferred compared to a larger slot size, because the lift gain per momentum is larger and (as a rough estimate) the percentage of engine bleed air corresponds to the percentage of overall thrust reduction.

As a reference aircraft for the following consideration, an airplane for 260 passengers, a wing area of $S = 244m^2$ and a maximum take off weight of $m = 134\,t$ is chosen. For take off the reference aircraft needs a high-lift system, which can generate a two-dimensional lift coefficient of about $c_l \approx 2.7$. The large high-lift flap with circulation control can provide the necessary lift for take off with flap deflections of $\eta = 20°$. For landing much higher lift coefficients are needed in combination with large drag coefficients. The reference aircraft requires a necessary two-dimensional lift coefficient of about $c_l \approx 3.7$ for the high-lift system. The preceding two-dimensional numerical simulations for this flow condition showed, that this can be achieved with a flap deflected by $\eta = 40°$, this time for an angle of attack of $\alpha = 4°$ [15]. Therefore the model features a flap deflection angle of $\eta = 40°$ to investigate the most important configuration.

In order to achieve a two-dimensional flow around the circulation controlled airfoil and to keep wall interference as small as possible, the aspect ratio of the model should be large. Therefore the chord has to be as short as possible. On the other hand the Reynolds number should be as large as possible to reduce the influence of low Reynolds number effects. As a reasonable compromise a chord length of $c = 0.3m$ was chosen for the wind tunnel model, which yields an aspect ratio of $\Lambda = 4.3$ and a Reynolds number of $\mathrm{Re} = 1 \cdot 10^6$. A profile with this length also provides sufficient space for the ducting of the pressurised air.

With the geometric parameters defined, an aluminium wind tunnel model was manufactured. The model design is displayed in **Figure 3**. The necessary mass flow of pressurised air used for circulation control is supplied into the model using both lateral sides of the wing. Thereby the total pressure distribution in the duct becomes more homogeneous and symmetrical in spanwise direction. Before wind tunnel testing the uniformity of the static pressure in the plenum in spanwise direction was checked by pressure measurements at five locations in the model. For medium feed pressures corresponding to momentum coefficients around $c_\mu = 0.04$ the mean absolute deviation of the static pressures in the plenum was less than 0.1%.

To analyse the jet distribution in spanwise direction, the dynamic pressure in the jet $0.01m$ downstream of the slot was measured. For that reason a small Pitot tube was traversed in spanwise direction. To always measure the same location inside the jet, the probe was kept in close contact to the wall. The results for a medium feed pressure are plotted in **Figure 4**. Here η is the normalised spanwise coordinate of the probe position. The mean absolute deviation of the dynamic pressure is less than 6.5%. Thus we can assume an almost constant momentum coefficient of the jet in spanwise direction over the whole model, which is an important requirement to obtain two-dimensional flow in the middle of the airfoil. It is important to mention that this data cannot be used to determine the jet velocity, as because of its size the probe measures an averaged pressure over a certain boundary layer height. Measurements of the slot yielded a slot height of $h/c = 0.001$ with a maximum deviation of $\Delta h/c = 0.0001$.

4 Wind Tunnel Experiments

The experimental investigations were conducted in the low speed wind tunnel of the Technische Universität Braunschweig, which is a closed-return atmospheric tunnel with a $1.3m$ x $1.3m$ closed test section. An opening angle of $\gamma = 0.2°$ of the floor and ceiling of the test section compensates for the boundary layer growth. In the measurement section a maximum speed of $55m/s$ can be achieved. A heat exchanger in the settling chamber allows constant flow temperature.

The wind tunnel model with circulation control was investigated at a free stream velocity of $v_\infty = 50m/s$, which results in a Mach number of $\mathrm{Ma}_\infty = 0.15$ and a Reynolds number of $\mathrm{Re} = 1 \cdot 10^6$. To analyse the performance of the airfoil for different momentum coefficients the static pressure of the pressurised air provided by a blower could be varied from ambient pressure to $p_{blower}/p_\infty = 2$. To determine the momentum coefficient of the jet, the mass flow from the slot and the jet velocity are needed. To measure the massflow into the airfoil, a flow measuring device is connected to the piping. When the total pressure and the total temperature of the air in the plenum and the static pressure at the slot are measured, the jet velocity can be computed, using the equations for compressible flow and assuming an isentropic change of state from the plenum to the slot. To account for non isentropic losses an efficiency factor for the expansion was evaluated based on numerical simulations of the flow: $\eta_{expansion} = \Delta h/\Delta h_s = v_{jet}^2/v_{jet,s}^2 = 0.96^2$. Thus the momentum coefficient for all experiments could be computed.

The strong suction peak at the airfoil nose causes large laminar flow separation bubbles with a strong effect on the overall airfoil flow. Therefore a zigzag strip was glued very close to the leading edge. The thickness of this transition strip was chosen as $25\mu m$, by which overtripping could be avoided.

To check for two-dimensional separation behaviour of the airfoil, tufts were attached to the upper surface. The flow separation always started in the centre of the airfoil as there was the highest aerodynamic load and then started to grow towards the side walls.

The pressure distribution around the airfoil was measured for different momentum coefficients. For each analysed momentum coefficient the measurements started at an angle of attack of $\alpha = -5°$. The angle of attack was then gradually increased until the flow separated from the airfoil. The pressure distribution on the model surface was measured by 63 pressure taps, which are positioned in the plane of symmetry of the airfoil. The pressure taps were distributed to offer high resolution at the leading edge and on the Coanda surface to capture the suction peaks with sufficient accuracy. There was also one pressure tap in the trailing edge, which features a thickness of $d/c = 0.004$.

In order to compute the c_p-distribution, the pressure at the ceiling and the floor in the plane of symmetry of the test section at a position of 9.5 chord length behind the airfoil was averaged and used as reference pressure. As the experimental calibration of the freestream velocity by the wind tunnel nozzle factor is affected by the high-lift airfoil in the test section, the velocity in the measurement section is measured at the same position as the reference pressure using two Prandtl tubes.

In **Figure 5** the c_p-distributions for an angle of attack of $\alpha = 0°$ and different momentum coefficients are plotted. Without blowing the flow separates at the very beginning of the flap. For small momentum coefficients like $c_\mu = 0.021$ the flow separates downstream of the Coanda surface. If momentum coefficients greater than $c_\mu = 0.040$ are used the flow stays attached up to the trailing edge. Note that an increase of the momentum coefficient always corresponds to an increase of the circulation around the complete airfoil and not only decreases the pressure on the flap. The stagnation point on the lower surface moves backwards if the blowing is intensified. **Figure 8** shows the c_p-distributions around the wind tunnel model for $c_\mu = 0.045$. If the angle of attack is increased the suction peak at the nose becomes stronger as the stagnation point moves backwards. At the same time the suction peak above the Coanda surface weakens.

Using the measured pressure distribution the force normal to the airfoil chord could be computed. In **Figure 7** the normal force coefficients c_n are shown for seven different momentum coefficients between $c_\mu = 0.021$ and $c_\mu = 0.057$. For comparison the normal force coefficients of the airfoil without blowing are also plotted, here the flow over the flap is fully detached for each angle of attack. When the momentum coefficient of the jet is increased, the normal force is increased as well, whereas the angle of attack, for which the maximum normal force is achieved, decreases. The gain in normal force for increasing the momentum coefficient becomes smaller for higher momentum coefficients. For small momentum coefficients the blowing works as boundary layer control, the momentum of the jet results in a later separation of the flow on the upper surface of the flap. When the flow stays attached up to the trailing edge, the end of boundary layer control is reached; a further increase in jet momentum results in super circulation. For super circulation the normal force is still increased by increasing the momentum coefficient. However, the efficiency of the flow control device $\Delta c_n/\Delta c_\mu$ is reduced. This can be seen in **Figure 8**, where the gain in normal force coefficient is plotted over the corresponding momentum coefficient for an angle of attack of $\alpha = 3°$. For the investigated airfoil super circulation starts for momentum coefficients larger than $c_\mu = 0.040$.

Long distance μPIV was used to measure the velocity field over the flap in the centre of the airfoil. Therefore a Quantel Brilliant double pulsed Nd:YAG laser with an energy of $E = 150mJ$ per pulse was used to illuminate a flow parallel light sheet in the middle of the wind tunnel. Due to the necessary high laser power per volume needed for long distance μPIV, reflections of the laser light become an important issue. To prevent the laser sheet from hitting the airfoil surface at a right angle, the light sheet was tilted by $\gamma \approx 35°$ from the vertical. Thus the reflections from the surface could be reduced. To further reduce the reflections the model surface was polished. The laser sheet had a width of $w = 80mm$ and a thickness of $t = 0.1mm$ to reduce the out of plane component of the measured velocity.

Due to the high spatial resolution in association with μPIV a high concentration of seeding particles is necessary in the area of interest. To achieve this high density of tracer particles in the outer flow, stream-tube seeding was realised by introducing the seeding to the flow in the settling chamber of the wind tunnel by a traversable tube with a streamline fairing. Thus a filament of high density seeding with a diameter of about 50mm is created. The pressure distribution around the airfoil is not changed by the tube. The influence of the traversable tube on the turbulence level was assessed by Kruse [18] and has no significant effect on the current measurements.

To get tracer particles into the jet, a second flow of pressurised air is mixed with the flow from the blower. Before the secondary flow is fed into the main flow, after passing through a seeding generator, it is ducted

through a cyclone to remove large tracer particles. Thus the interior of the model could be kept clean and a high quality of the seeding particles in the jet can be assured.

For the computation of the momentum coefficient of the jet this additional mass flow has to be monitored as well. As seeding, oil particles with a diameter of about $1\mu m$ were employed. To reduce window contamination by tracer particles, pressurised air is blown through a slot in the wind tunnel wall upstream of the model.

A LaVision Imager ProX 11M with a resolution of 4008 x 2672 pixels was used to capture the particle images. Fast recording of image pairs is ensured by a minimum frame transfer rate of 250ns. A long-distance microscope (Infinity K2) equipped with two magnifier tubes and the close objective CF1 is employed to obtain the optical magnification necessary to investigate the flow in the vicinity of the slot and on the Coanda surface. For data acquisition and data evaluation, Davis7.2 by LaVision was used.

One set of measurements was done to visualize the velocity field in the vicinity of the slot. Thousand images with a field of view of $17mm$ x $11mm$ were taken for an angle of attack of $\alpha = 0°$ and for momentum coefficients of $c_\mu = 0.026$, $c_\mu = 0.033$, $c_\mu = 0.038$, $c_\mu = 0.044$, $c_\mu = 0.050$ and $c_\mu = 0.055$. For an angle of attack of $\alpha = 3°$ thousand images were taken for momentum coefficients of $c_\mu = 0.026$, $c_\mu = 0.032$, $c_\mu = 0.037$, $c_\mu = 0.043$, $c_\mu = 0.049$ and $c_\mu = 0.055$. Once the particle image acquisition of 1000 image pairs for each measurement was completed, the velocity vector field of the flow around the airfoil had to be determined. After several image preprocessing techniques to improve the particle image quality, the particle displacement evaluation was executed in the next step using a cross correlation scheme. Here a multipass interrogation scheme was applied with decreasing interrogation window size from 128 x 128 pixels down to 64 x 64 pixels, 50% overlap and window shifting and deformation. A spatial resolution of the obtained vector field of $0.14mm$ in both directions was achieved, with the first velocity vector in a distance of $d/c < 0.0005$ to the wall. The resulting set of 1000 vector fields for each measurement was then post-processed. It was necessary to filter out non physical vectors, which would corrupt the results of the ensemble averaging procedure. Only if in at least 250 vector fields a valid vector was found at a certain position an average velocity vector for this position was computed. The computed average flow field in the vicinity of the slot for a momentum coefficient of $c_\mu = 0.037$ and an angle of attack of $\alpha = 3°$ is displayed in **Figure 9**. The boundary layer on the upper surface upstream of the slot as well as the high velocity in the jet can be seen. In **Figure 12** the flow field for a momentum coefficient of $c_\mu = 0.043$ is plotted. It is apparent that the velocity in the boundary layer as well as the velocity in the jet is increased for the higher momentum coefficient.

The second set of images was taken in order to measure the velocity profiles on the Coanda surface downstream of the slot. As the same optical setup was used the vector field yields also a spatial resolution of $0.14mm$ in both directions. The first velocity information is gained in a distance of $d/c < 0.0005$ to the wall. One thousand images with a size of $17mm$ x $11mm$ were taken for the same parameter space as for the first setup. To evaluate the velocity vectors the same algorithm were used as above. The computed average flow field above the Coanda surface for a momentum coefficient of $c_\mu = 0.037$ and an angle of attack of $\alpha = 3°$ is displayed in **Figure 10**. The high velocity in the jet attached to the Coanda surface can be seen. For a momentum coefficient of $c_\mu = 0.043$ the velocity in the jet is further increased, which can be seen in **Figure 13**.

The third set of measurements was done to visualize the velocity field above the end of the flap. Thus it is possible to determine the minimum momentum coefficient necessary to keep the flow attached up to the trailing edge. For this measurement no magnifier tubes were used, thus the window size is increased to $70mm$ x $47mm$. The corresponding spatial resolution is $0.29mm$. Thousand images were taken for an angle of attack of $\alpha = 3°$ and for momentum coefficients of $c_\mu = 0.026$, $c_\mu = 0.032$, $c_\mu = 0.037$, $c_\mu = 0.043$, $c_\mu = 0.049$ and $c_\mu = 0.055$. To evaluate the velocity vectors the same algorithm were used as above, though a multipass interrogation scheme with decreasing interrogation window size from 128 x 128 pixels down to 32 x 32 pixels was applied. If a momentum coefficient of $c_\mu = 0.037$ is used for blowing the flow is not always attached to the flap. As the flow is in the transition from being completely separated and being attached, the average streamlines, which can be seen in **Figure 11**, are still parallel to the surface. However, the low velocity close to the flap surface shows that the flow is not attached to the surface most of the time. The flow field for a momentum coefficient of $c_\mu = 0.043$ is plotted in **Figure 14**. Here the momentum of the jet is high enough to keep the flow attached up to the trailing edge.

5 Numerical Simulation of Wind Tunnel Experiments

The three-dimensional flow around the wing utilising circulation control was simulated by solving the Reynolds-averaged Navier-Stokes equations, using the DLR hybrid unstructured flow solver TAU, as for the two-dimensional simulations used to design the wind tunnel model. To increase the accuracy of the three-dimensional simulations, low speed preconditioning was used. The viscous walls of the test section were also simulated to obtain realistic results for the flow around the wind tunnel model. For efficient flow computations the chimera technique was employed with a local grid defined around the airfoil. The chimera technique allows using an already attained solution as a restart for a following simulation with a different angle of attack. Using the chimera technique to gradually increase the angle of attack, the flow in the vicinity of maximum lift can be simulated correctly.

In **Figure 15** the spatial discretization of the wind tunnel test section can be seen. This hybrid mesh consists of $6 \cdot 10^6$ nodes. The cylindrical mesh around the model is positioned in the cylindrical hole of the background mesh. This local mesh, which is composed of $14 \cdot 10^6$ nodes, is displayed in **Figure 16** and can be rotated around its centreline. This centreline is identical to the axis of rotation of the wind tunnel model. Thus the chimera technique can be used to account for the hysteresis effect of the separation.

The structured area on the surface of the wing has a thickness of 40 cells. On the walls of the wind tunnel 32 prismatic layers were generated. The nondimensional first grid spacing normal to the wall is smaller than 1.5 on most parts of the surface of the wing, except for local values of about 5 at the nose and on the Coanda surface due to the locally very high velocities. In the vicinity of the jet slot and the trailing edge the grid for the numerical simulation is clustered to capture the jet behaviour correctly.

First simulations of the flow field around the wind tunnel model are performed with the standard ***S**palart-**A**llmaras* (SA) turbulence model without any curvature correction. In **Figure 17** the c_p-distribution on the model surface and the surface streamlines are shown for an angle of attack of $\alpha = 0°$ and a momentum coefficient of $c_\mu = 0.045$. Only one half of the symmetric model is shown in **Figure 17**. The backward side in the figure is the location of the wind tunnel side wall. The computed flow field shows that almost two-dimensional flow can be assumed in the middle of the measurement section. To compute the momentum coefficients the jet velocity in the plane of symmetry is mass averaged over the slot height, multiplied by the overall massflow and divided by the wing area and the dynamic pressure of the flow.

In order to compute the c_p-distribution, the pressure at the ceiling and the floor in the plane of symmetry of the test section at a position of 9.5 chord length behind the airfoil was averaged and used as reference pressure, as it was done for the experimental data. In **Figure 18** and **Figure 19** the measured c_p-distributions for a momentum coefficient of $c_\mu = 0.040$ for an angle of attack of $\alpha = -5°$ and $\alpha = 0°$ are compared with the results of the numerical simulations. In **Figure 20** and **Figure 21** the measured c_p-distributions for a higher momentum coefficient of $c_\mu = 0.045$ are compared with the results of the numerical simulations for the same angles of attack as above.

The good agreement of the numerical and the experimental results demonstrates the capability of the SA turbulence model to simulate the flow around a circulation control airfoil with a sharp trailing edge. Unsteady simulations for higher angles of attack have to be conducted to analyse the capability of the SA turbulence model to predict the flow in the proximity of maximum lift.

In **Figure 22 - 24** velocity profiles attained by particle image velocimetry are compared with the simulated velocity profiles at the midspan position of $x/c = 0.690$, $x/c = 0.715$ and $x/c = 0.755$. All velocity profiles shown here are given for an angle of attack of $\alpha = 0°$ and only the velocity component parallel to the surface is shown. At all positions the velocity is increased by increasing the momentum coefficient.

In **Figure 22** the velocity profiles at $x/c = 0.690$ are plotted, which corresponds to a position about $3mm$ upstream of the slot($x/c = 0.7$). For $c_\mu > 0.040$ the flow on the flap is completely attached and the shape of the velocity profiles is well predicted by using the SA turbulence model. Though the curvature of the experimental velocity profiles in the middle of the boundary layer is slightly smaller. In the regime of boundary layer control, when the c_μ is not large enough to keep the flow attached on the complete flap, the discrepancy between experimental and numerical velocity profiles is larger. Here the numerically simulated velocity for $c_\mu = 0.035$ at the edge of the boundary layer differs by 2% from the velocity interpolated from the experimental results for $c_\mu = 0.033$ and $c_\mu = 0.038$. The simulation for $c_\mu = 0.035$ shows a small separation on the edge of the flap, which has only a size of 2% of the chord length. In the experimental results the separation on the flap is already much stronger for this momentum coefficient (see **Figure 5**) and thus the circulation around the airfoil is reduced in the experiment. If a turbulence model is applied, which takes the effect of shear flow curvature into account, as the SARC model (SARC: ***S**palart-**A**llmaras* model for **R**otation and/or **C**urvature effects) [24], the size of the separation for $c_\mu = 0.035$ increases to 5%.

In **Figure 23** the velocity profiles at $x/c = 0.715$ are plotted, which corresponds to a position about

$4.5mm$ downstream of the slot. In these graphs the jet as well as the shear layer above the jet can be seen. Again the numerically simulated velocity for $c_\mu = 0.035$ at the edge of the boundary layer differs by 2% from the velocity interpolated from the experimental results. For the momentum coefficients of $c_\mu = 0.044$, $c_\mu = 0.050$ and $c_\mu = 0.055$ the shape of the shear layer is predicted quite well, but the momentum deficiency caused by the wake of the lip is about 6% larger in the experiment. The maximum jet velocity for $c_\mu = 0.055$ is about 30% higher in the simulations. It can be speculated that the resolution of the μPIV data is not high enough to resolve the jet profile completely that close to the slot, as the jet has a thickness of about $0.3mm$ at this position.

The velocity profiles on the Coanda surface are shown in **Figure 24** for a position of $x/c = 0.755$, which corresponds to an angle of 40° on the Coanda surface. The shape of the simulated velocity profile fits well to the experimental results. The absolute values get closer to the experimental results if the blowing is increased. For the highest investigated momentum coefficient of $c_\mu = 0.055$ the velocity is about 4% too small in the shear layer and about 7% in the middle of the jet.

6 Conclusions

The experimental investigation of an airfoil with circulation control using an internally blown high-lift flap yields high normal force coefficients at comparably low momentum coefficients. Pressure distributions along the airfoil and μPIV measurements are obtained to establish a data set useful for validating numerical simulation methods. First numerical simulations show a good agreement with the measured data, even if a simple one-equation turbulence model without curvature correction is used. More numerical simulations have to be conducted to see if the same good agreement can be achieved for maximum lift and if the momentum coefficient and the angle of attack for which separation starts can be predicted as well.

Acknowledgments

The present work is performed as a part of the European research project TimpAN (Technologies to IMProve Airframe Noise), which is part of the sixth framework programme. This project is founded by the European Commission and is coordinated by Airbus France. The authors thank the "Norddeutscher Verbund für Hoch- und Höchstleistungsrechnen" (HLRN) for providing the necessary computational resources.

References

[1] Bamber, M.J.: *Wind tunnel tests on airfoil boundary layer control using a backward-opening slot*, NACA Report 385, 1932.

[2] Hagedorn, H. and Ruden, P.: *Windkanaluntersuchungen an einem Junkers-Doppelflügel mit Ausblaseschlitz am Heck des Hauptflügels*, Bericht A 64 der Lilienthal-Gesellschaft für Luftfahrtforschung, 1938.

[3] Davidson, I. M.: *Aerofoil boundary layer control system*, British Patent No.913,754, 1960.

[4] Kind, R. J., Maul, D. J.: *An experimental investigation of a low-speed circulation controlled airfoil*, The Aeronautical Quarterly, Vol. XIX, May 1968, pp.170-182.

[5] Stevenson, T. A., Franke, M. E., Rhynard, W. E. and Snyder J. R.: *Wind-tunnel study of a circulation control elliptical airfoil*, AIAA Journal of Aircraft Vol.14, No. 9, 1977, pp.881-886.

[6] Novak, C. J.,Cornelius, K. C. and Roads R. K.: *Experimental investigations of the circular wall jet on a circulation control airfoil*, AIAA Paper 87-0155, 1987.

[7] Thomas, F.: *Untersuchungen über die Grenzschichtbeeinflussung durch Ausblasen zur Erhöhung des Auftriebes*, Technische Universität Braunschweig, doctoral thesis, 1961.

[8] Körner, H. and Löhr, R.: *Dreikomponentenmessungen am Modell eines leichten STOL-Flugzeuges mit Ausblasen in Flügeltiefenrichtung*, Deutsche Forschungs- und Versuchsanstalt für Luft- und Raumfahrt, DLR-FB 75-74, 1975.

[9] Englar, R. J.: *Overview of circulation control pneumatic aerodynamics: Blown force and moment augmentation and modification as applied primarily to fixed-wing aircraft*, In: Joslin, D., Jones, G. S. (editors): Applications of circulation control technology, Progress in Astronautics and Aeronautics, Vol.214, AIAA, 2006, pp.23-68.

[10] Loth, J. L.: *Advantages of combining BLC suction with circulation control high-lift generation*, In: Joslin, D., Jones, G. S. (editors): Applications of circulation control technology, Progress in Astronautics and Aeronautics, Vol.214, AIAA, 2006, pp.3-21.

[11] Jones, G. S., Yao, C.-S. and Allan, B. G.: *Experimental investigation of a 2D supercritical circulation-cotrol airfoil using particle image velocimetry*, AIAA Paper 2006-3009, 2006.

[12] Baker, W. J. and Paterson, E. G.: *Simulation of steady circulation control for the general aviation circulation control (GACC) wing*, 2004 NASA-ONR Circulation Control Workshop, March 2004.

[13] Slomski, J. F.,Chang, P. A. and Arunajatesan, S.: *Large eddy simulation of a circulation control airfoil*, 2004 NASA-ONR Circulation Workshop, March 2004.

[14] Pfingsten, K. C. and Radespiel, R.: *Numerical Simulation of a wing with a gapless high-lift system using circulation control*, Notes on Numerical Fluid Mechanics and Multidisciplinary Design, Vol. 96, C. Tropea, Springer, Berlin, 2007.

[15] Pfingsten, K. C. and Radespiel, R.: *Experimental and Numerical Investigation of a Circulation Control Airfoil.*, AIAA Paper 2009-533, 47th AIAA Aerospace Sciences Meeting, Orlando, Florida, 2009.

[16] Kähler, C. J., Scholz, U. and Ortmanns, J.: *Wall-shear-stress and near-wall turbulence measurements up to single pixel resolution by means of long-distance micro-PIV*, Exp. Fluids 41,2006, Springer 2006.

[17] Englar, R.J. and Hemmerly, R.A.: *Design of the circulation control wing STOL demonstrator aircraft*, AIAA Journal of Aircraft Vol.18, No. 1, 1981, pp. 51-58.

[18] Kruse, M. and Radespiel, R.: *Measurement of a laminar separation bubble on a swept horizontal tailplane using μPIV*, AIAA Paper 2008-4054, 38th Fluid Dynamics Conference, Seattle, Washington, 2008.

[19] DLR: *Technical Documentation of the DLR TAU-Code*, Institut für Aerodynamik und Strömungsmechanik, Braunschweig, Göttingen, 2006.

[20] Gerhold, T.: *Overview of the hybrid RANS code TAU*, MEGAFLOW-Numerical Flow Simulation for Aircraft Design Vol.89 Springer-Verlag, 2005 (Notes on Numerical Fluid Mechanics and Multidisciplinary Design), pp.81-92.

[21] Spalart, P. R. and Allmaras, S. R.: *A one-equation turbulence model for aerodynamic flows*, AIAA 92-043, 1992.

[22] Pfingsten, K. C., Jensch, C.,Körber, K. W. and R. Radespiel: *Numerical simulation of the flow around circulation control airfoils*, First CEAS European Air and Space Conference, Berlin, 2007.

[23] Swanson, R. C. and Rumsey, C. L.: *Numerical issues for circulation control calculations*, AIAA Paper 2006-3008, 2006.

[24] Shur, M. L. ,Strelets, M. K., Travin, A. K. and Spalart, P. R.: *Turbulence modeling in rotating and curved channels: Assessing the Spalart-Shur correction*, AIAA Journal, Vol.38, No. 5, 2000, pp. 784-792.

Figures

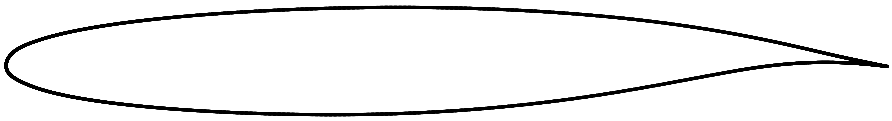

Figure 1: Basic transonic airfoil (not to scale)

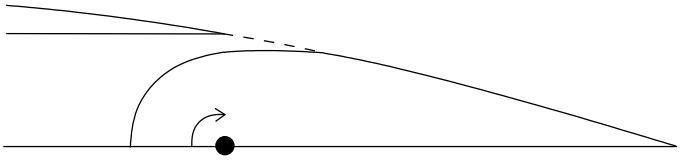

Figure 2: Design of the large high-lift flap

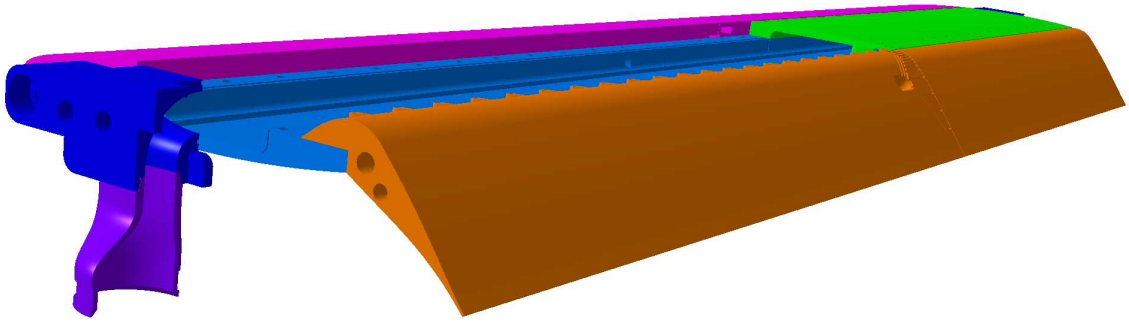

Figure 3: Wind tunnel model with circulation control ducts ($c/c_{flap} = 0.3, h/c = 0.001, \eta = 40°, b/c = 4.3$)

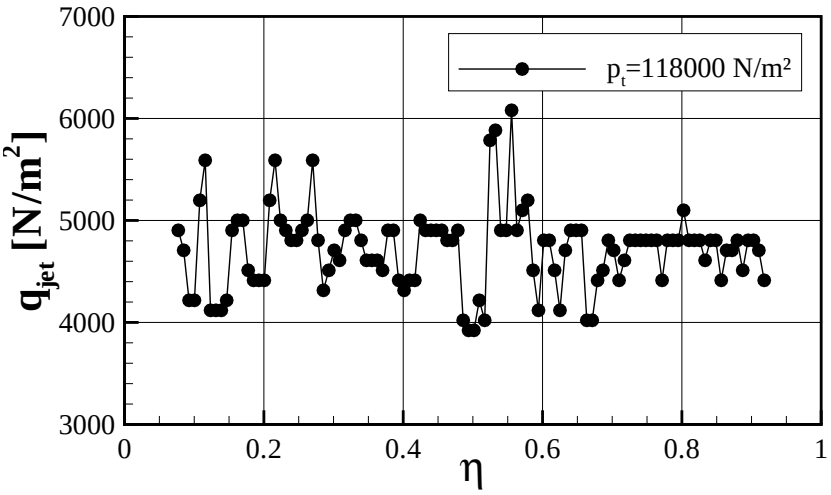

Figure 4: Dynamic pressure distribution in spanwise direction at a position $0.01m$ downstream of the slot

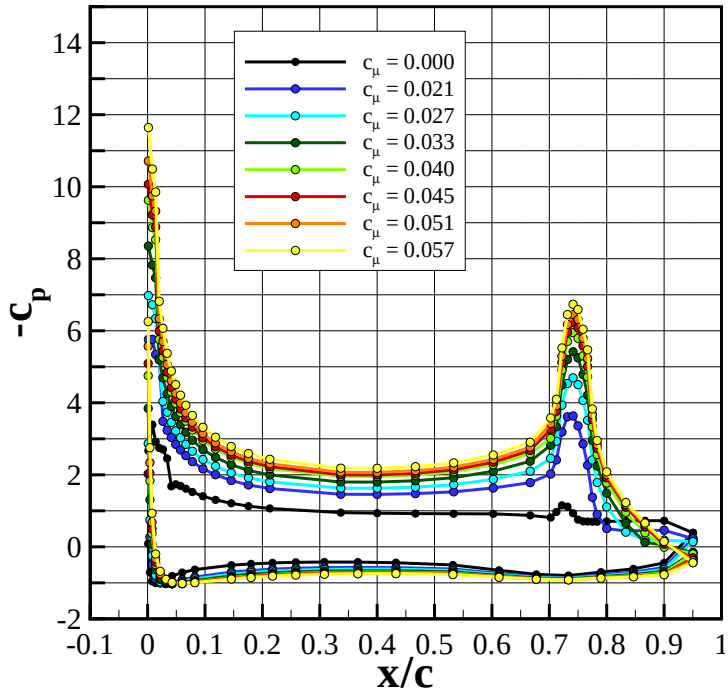

Figure 5: c_p-distribution for $\alpha = 0°$, $\mathrm{Ma}_\infty = 0.15$, $\mathrm{Re} = 1 \cdot 10^6$

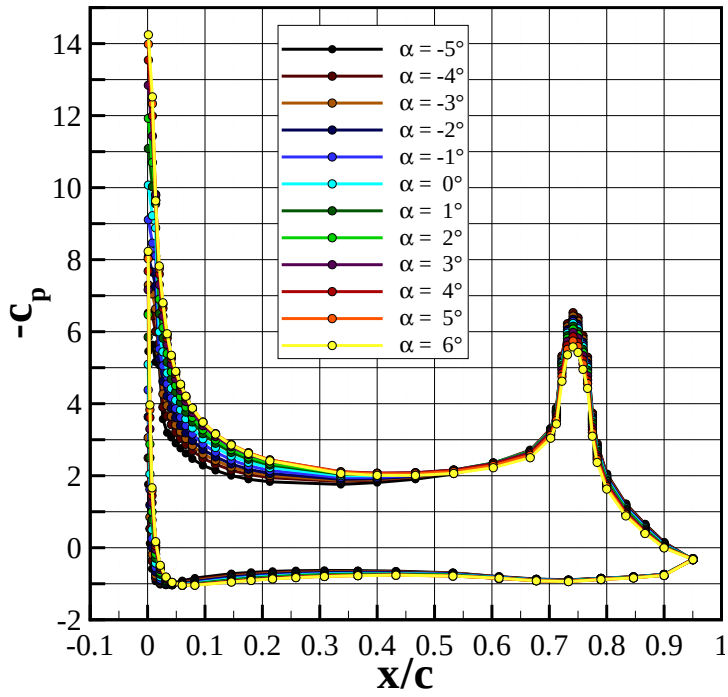

Figure 6: c_p-distribution for $c_\mu = 0.045$, $\mathrm{Ma}_\infty = 0.15$, $\mathrm{Re} = 1 \cdot 10^6$

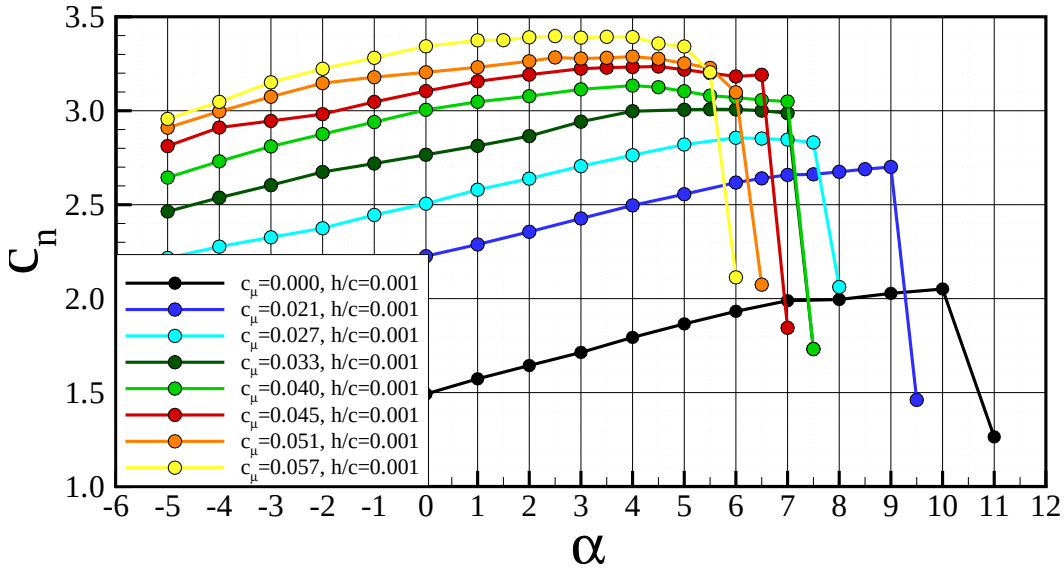

Figure 7: c_n over α for different momentum coefficients ($\mathrm{Ma}_\infty = 0.15$, $\mathrm{Re} = 1 \cdot 10^6$)

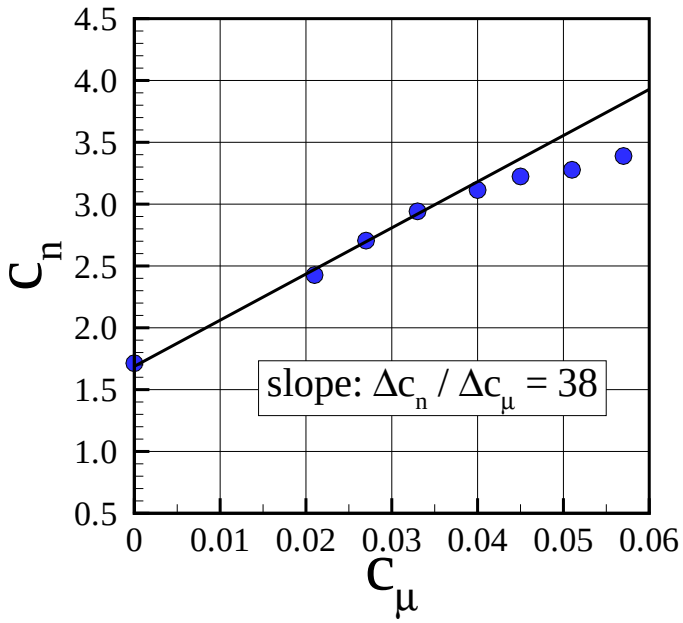

Figure 8: c_n over c_μ for an angle of attack of $\alpha = 3°$ ($\mathrm{Ma}_\infty = 0.15$, $\mathrm{Re} = 1 \cdot 10^6$)

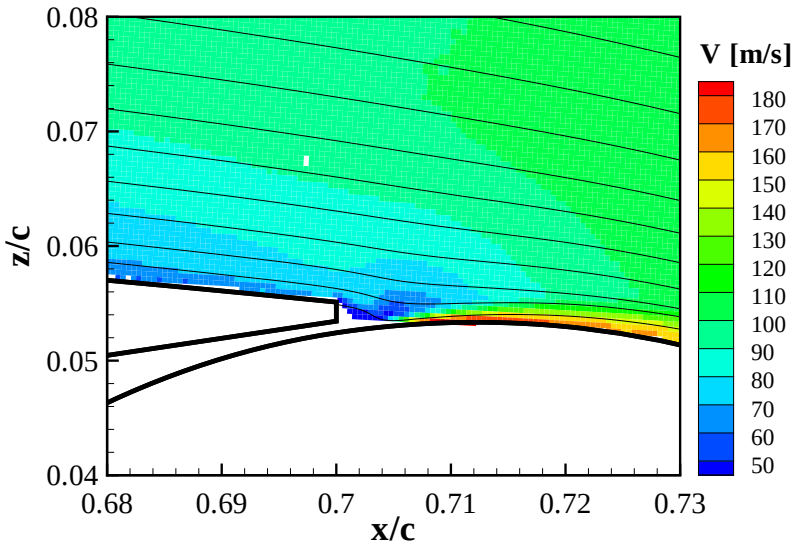

Figure 9: Measured velocity field at the slot for $c_\mu = 0.037$ and $\alpha = 3°$ ($\mathrm{Ma}_\infty = 0.15$, $\mathrm{Re} = 1 \cdot 10^6$)

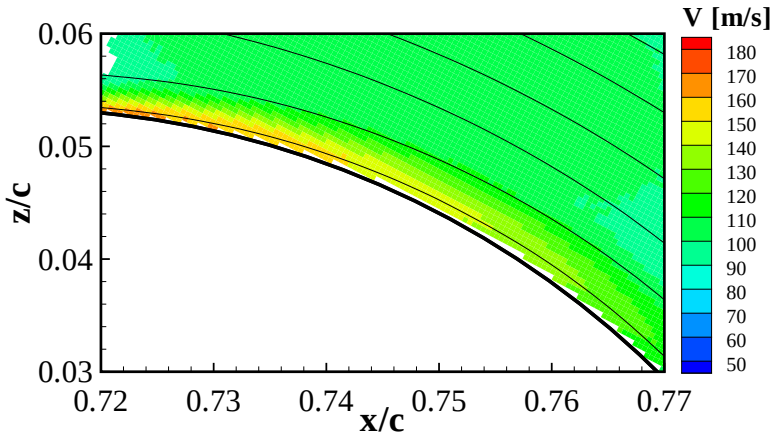

Figure 10: Measured velocity field at the Coanda surface for $c_\mu = 0.037$ and $\alpha = 3°$ ($\mathrm{Ma}_\infty = 0.15$, $\mathrm{Re} = 1{\cdot}10^6$)

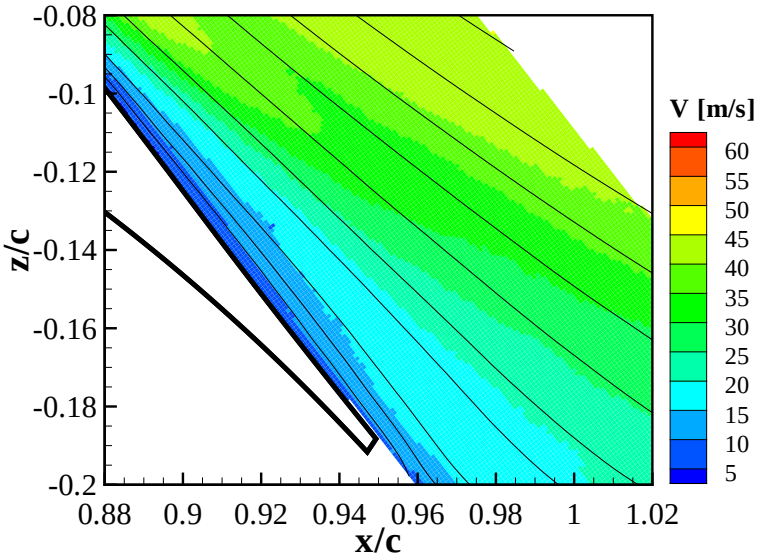

Figure 11: Measured velocity field at the trailing edge for $c_\mu = 0.037$ and $\alpha = 3°$ ($\mathrm{Ma}_\infty = 0.15$, $\mathrm{Re} = 1 \cdot 10^6$)

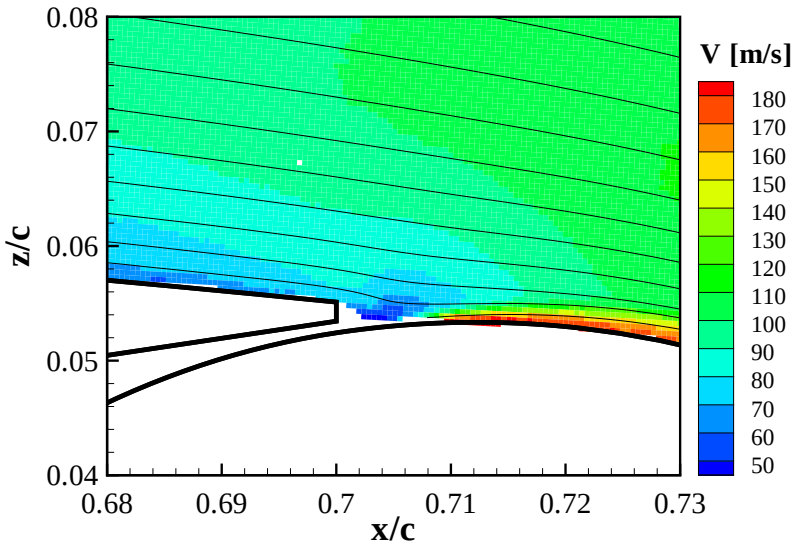

Figure 12: Measured velocity field at the slot for $c_\mu = 0.043$ and $\alpha = 3°$ ($\mathrm{Ma}_\infty = 0.15$, $\mathrm{Re} = 1 \cdot 10^6$)

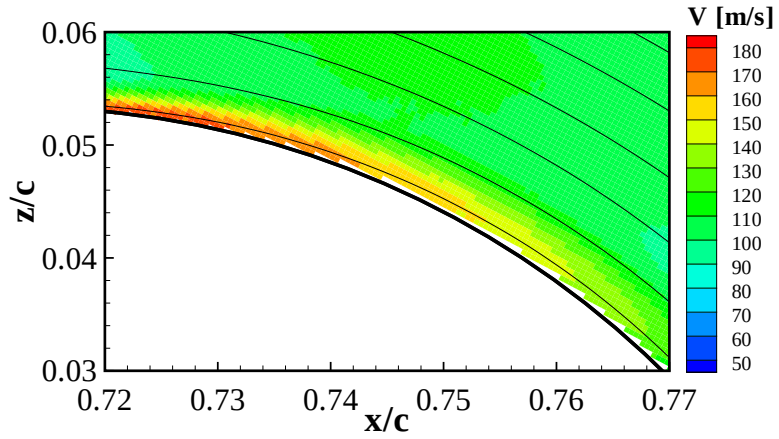

Figure 13: Measured velocity field at the Coanda surface for $c_\mu = 0.043$ and $\alpha = 3°$ ($\mathrm{Ma}_\infty = 0.15$, $\mathrm{Re} = 1{\cdot}10^6$)

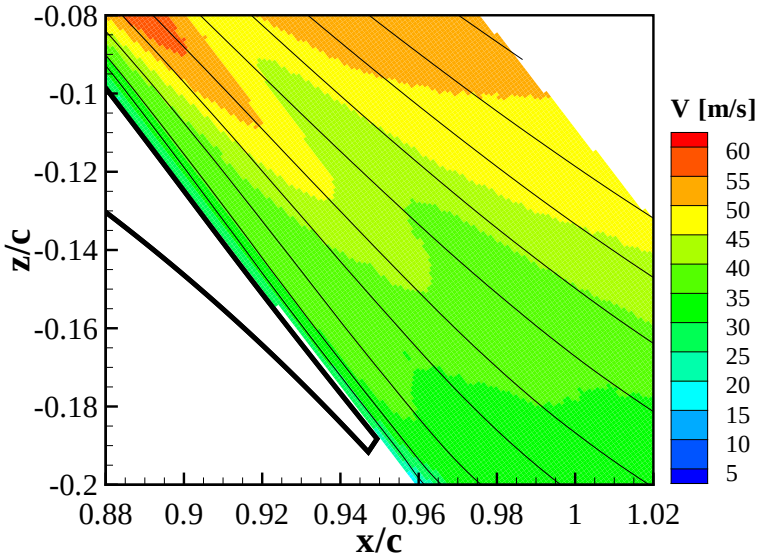

Figure 14: Measured velocity field at the trailing edge for $c_\mu = 0.043$ and $\alpha = 3°$ ($\mathrm{Ma}_\infty = 0.15$, $\mathrm{Re} = 1 \cdot 10^6$)

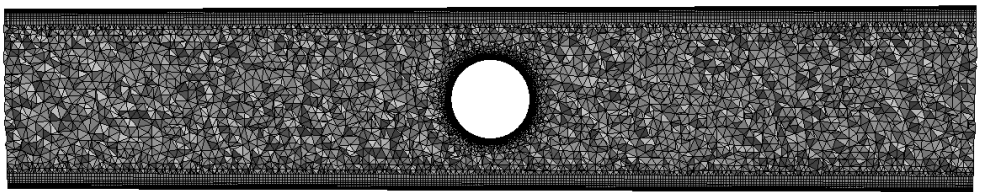

Figure 15: Spatial discretization of the wind tunnel measurement section

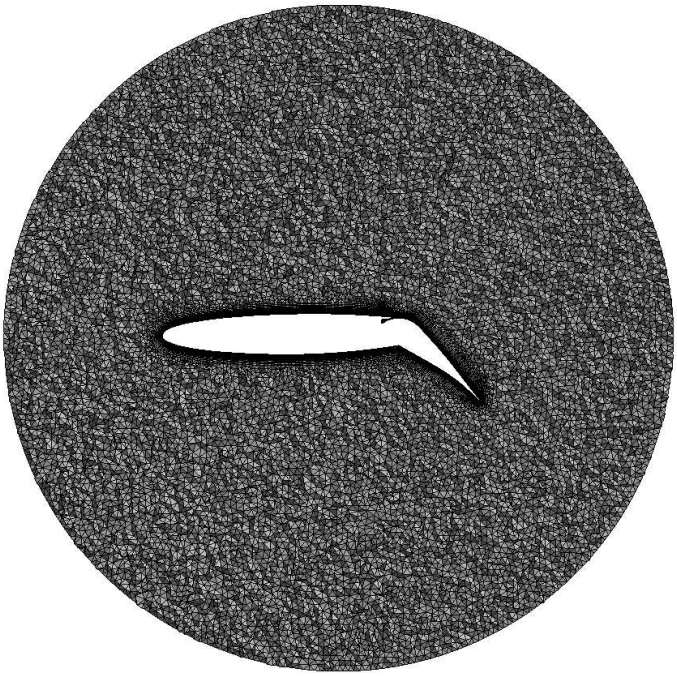

Figure 16: Spatial discretization of the circulation control airfoil

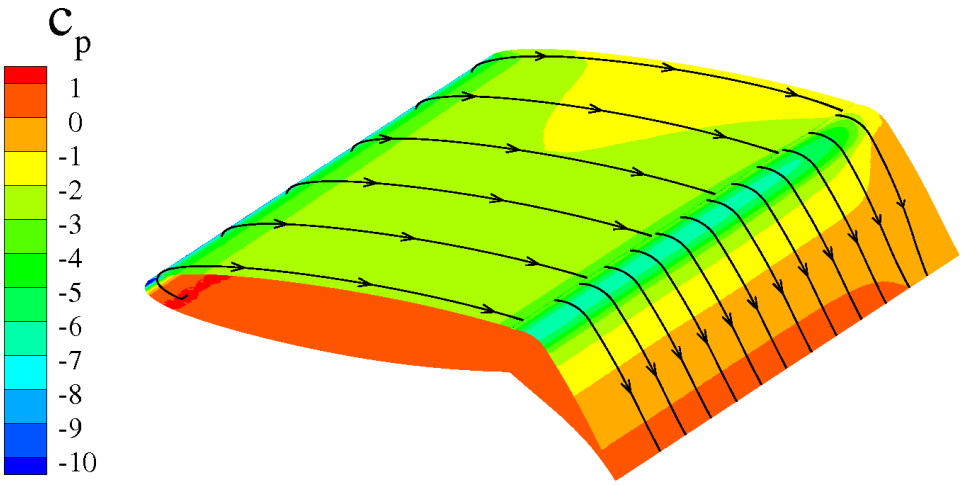

Figure 17: c_p-distribution and surface streamlines on the wing with circulation control:
$\mathrm{Re} = 1 \cdot 10^6$, $\mathrm{Ma} = 0.15$, $c_{flap}/c = 0.3$, $\eta = 40°$, $\alpha = 0°$, $c_\mu = 0.045$, $c_L = 3.04$, $c_D = 0.097$, $c_{M,1/4} = -0.55$

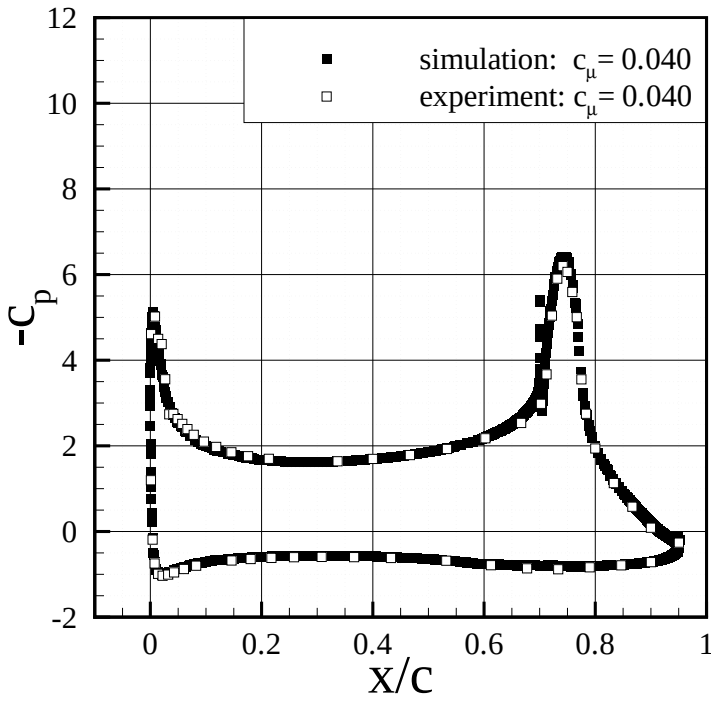

Figure 18: c_p-distribution for $\alpha = -5°$, $\mathrm{Ma}_\infty = 0.15$, $\mathrm{Re} = 1 \cdot 10^6$ (SA turbulence model)

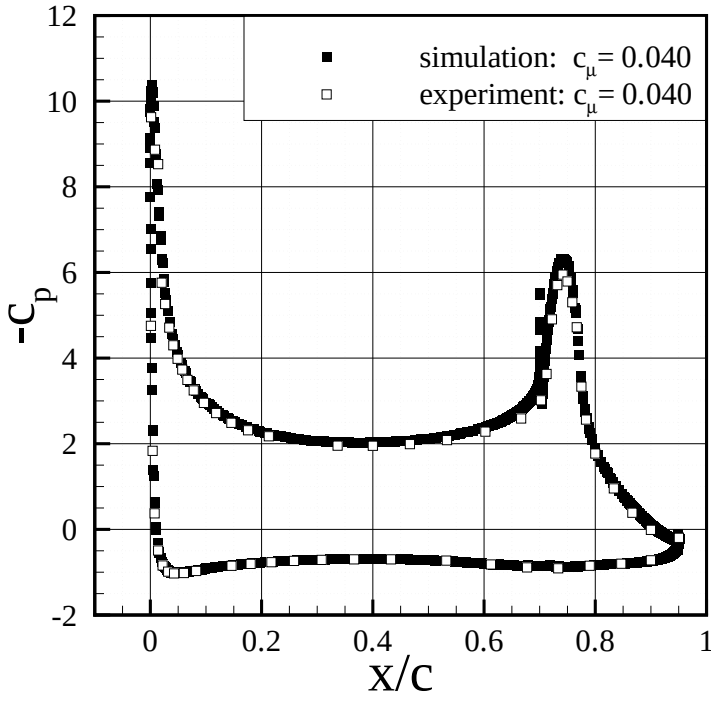

Figure 19: c_p-distribution for $\alpha = 0°$, $\mathrm{Ma}_\infty = 0.15$, $\mathrm{Re} = 1 \cdot 10^6$ (SA turbulence model)

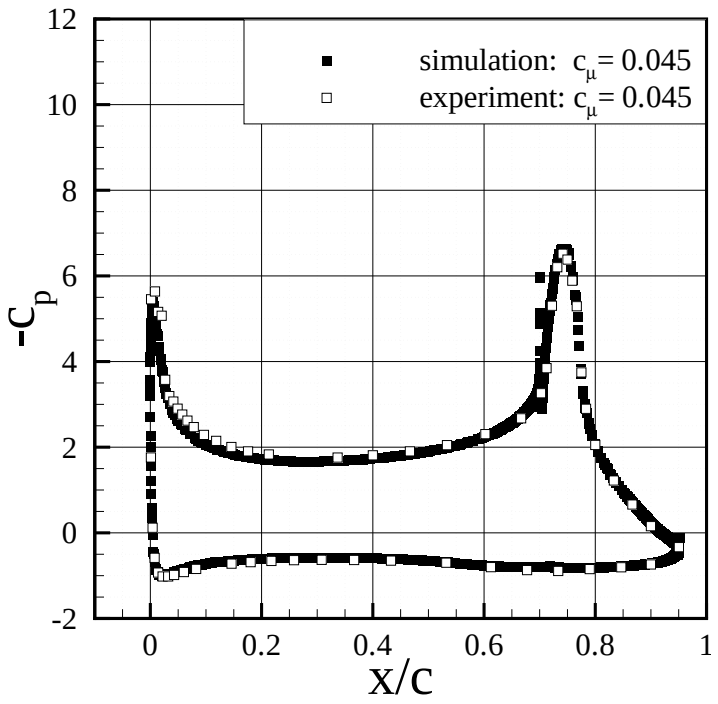

Figure 20: c_p-distribution for $\alpha = -5°$, $\mathrm{Ma}_\infty = 0.15$, $\mathrm{Re} = 1 \cdot 10^6$ (SA turbulence model)

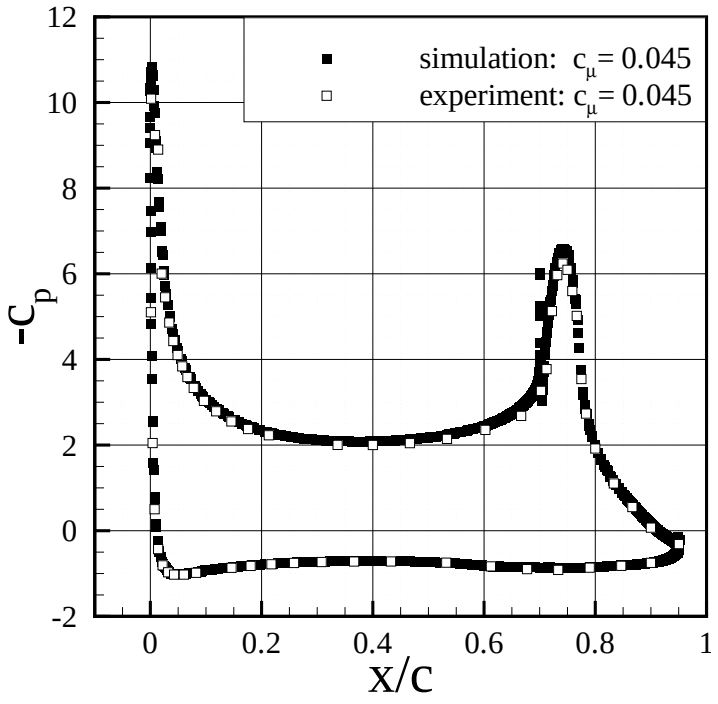

Figure 21: c_p-distribution for $\alpha = 0°$, $\mathrm{Ma}_\infty = 0.15$, $\mathrm{Re} = 1 \cdot 10^6$ (SA turbulence model)

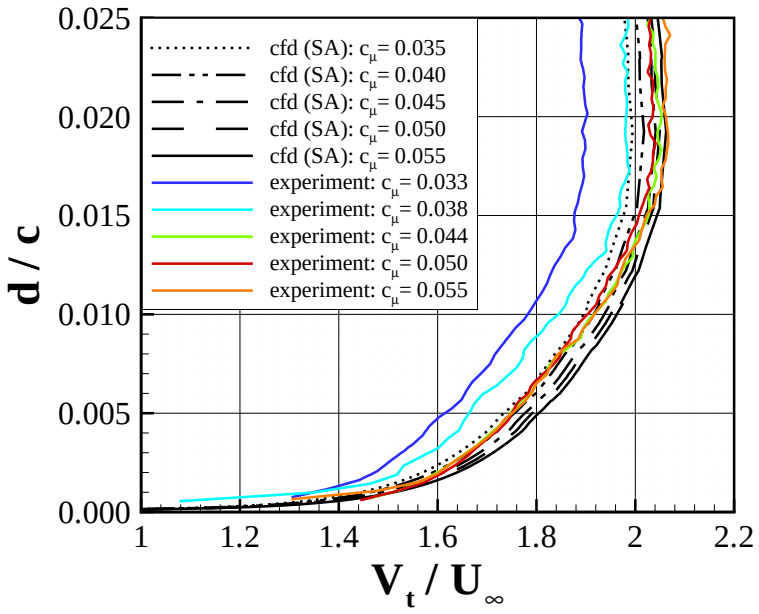

Figure 22: Tangential velocity at $x/c = 0.690$ for $\alpha = 0°$ ($\mathrm{Ma}_\infty = 0.15$, $\mathrm{Re} = 1 \cdot 10^6$)

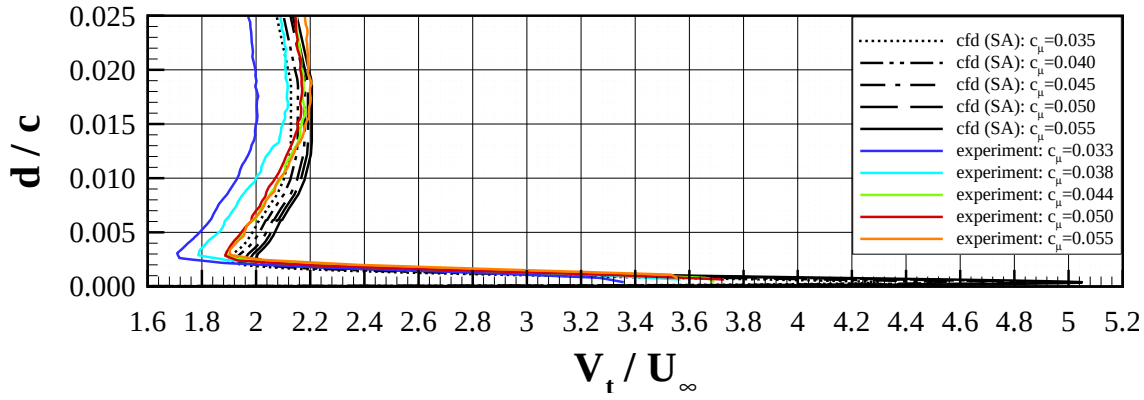

Figure 23: Tangential velocity at $x/c = 0.715$ for $\alpha = 0°$ ($\mathrm{Ma}_\infty = 0.15$, $\mathrm{Re} = 1 \cdot 10^6$)

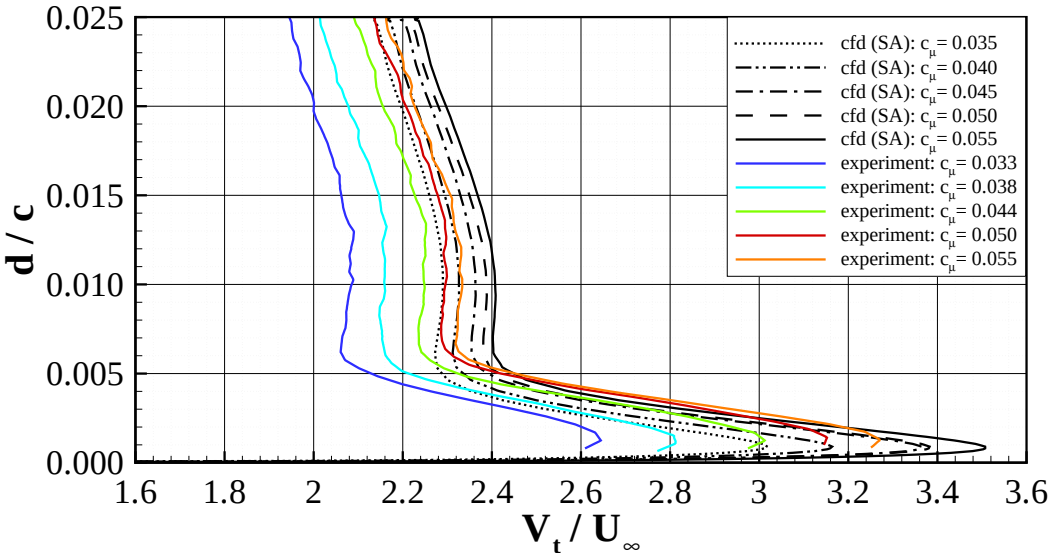

Figure 24: Tangential velocity at $x/c = 0.755$ for $\alpha = 0°$ ($\mathrm{Ma}_\infty = 0.15$, $\mathrm{Re} = 1 \cdot 10^6$)

47th AIAA Aerospace Sciences Meeting Including The New Horizons Forum and Aerospace Exposition
5 - 8 January 2009, Orlando, Florida

AIAA 2009-533

Experimental and numerical investigation of a circulation control airfoil

Kai Christoph Pfingsten* and Rolf Radespiel†

Institute of Fluid Mechanics (ISM), Technische Universität Braunschweig

Bienroder Weg 3, 38106 Braunschweig, Germany

K.C.Pfingsten@googlemail.com

When air is blown from a slot directly upstream of a flap, the flow over the flap can bear large adverse pressure gradients without separation. This effect is used to design high-lift airfoils with low momentum coefficients of blowing. For experimental assessment of these airfoils a rectangular wing with an aspect ratio of 4.3 was built. The flow around the model in a low speed wind tunnel is analysed using pressure measurements, oil flow pictures and particle image velocimetry. For Reynolds numbers of about Re$= 1 \cdot 10^6$ the dimensionless momentum coefficient of the jet and the angle of attack of the airfoil are varied. Numerical simulations of the three-dimensional flow around the circulation control airfoil in the wind tunnel are compared to the experimental data. Good agreement is observed in terms of pressure distributions and wall streamlines.

I. Introduction

In recent years noise pollution from aircraft, especially around airports, has become a huge problem. Hence there is an increasing interest in reducing the noise emitted during take off and landing. The conventional high-lift systems, consisting of slats and slotted flaps, are a major contributor of airframe noise. Therefore a gapless high-lift system without slats has a potential of reducing the overall noise emitted by an aircraft. With active flow control a gapless high-lift device is capable of generating the high lift coefficients needed for climb and landing. For circulation control a small fraction of the cold engine flow is used for blowing. The bleed air is pipelined from the engine to a slot directly upstream of the flap and thus the flow over the flap can bear large adverse pressure gradients without separation. Thus a gapless high-lift device with circulation control can generate the required lift. The low drag coefficients during climb-out, achievable with this powered high-lift system, could also allow for new low-noise trajectories, which would further reduce noise impact on the ground. The absence of slats might allow for laminar flow conditions in cruise flight, thereby reducing the drag in this flight segment. Even taking into account the additional system weight associated with the bleed air distribution for a gapless high-lift system, there is a chance of reducing the total weight of the aircraft and possibly the cost, because slats and fowler systems are no longer needed.

The first experiments using blowing to improve lift were conducted in the thirties of the last century by Bamber[1] as well as Hagedorn and Ruden.[2] Circulation control was first proposed for the flow over a circular cylinder by Davidson[3] and then applied to elliptical airfoils by Kind and Maul.[4] Elliptical airfoils utilising circulation control were also investigated by Stevenson et al[3] and Novak et al.[6] At Technische Universität Braunschweig systematic measurements and theoretical considerations for wings with blown flaps by Thomas[7] and Körner[8] yielded lift increase versus necessary momentum coefficients. The elliptical airfoil

*Research Assistant.

†Professor. AIAA Senior Member.

with circulation control as well as the internally blown flap were extensively investigated by Englar[9] who could demonstrate good lift-over-drag performance. The first aircraft to demonstrate the high-lift capability of circulation control was a technology demonstrator built by Loth.[10] An experimental investigation using particle image velocimetry to assess the flow around a circulation control airfoil with an elliptical trailing edge as well as the flow around an airfoil with a flap was conducted by Jones et al.[11] These configurations were assessed numerically by Baker and Paterson[12] using two-dimensional RANS simulations. Large-eddy simulations for an elliptical profile with circulation control were performed by Slomski et al.[13]

Due to the promising results of preceding numerical simulations by the authors[14] further experimental investigations are conducted to analyse an airfoil with circulation control. Simultaneously, numerical simulations of the wind tunnel experiments are performed. The experimental and numerical results are compared to assess the ability of the used flow solver to simulate the flow around an airfoil with circulation control.

II. Coanda Effect

Profiles with blowing close to the trailing edge use the well known Coanda principle to generate high lift coefficients. If a jet is positioned close to a wall, pressure forces change the path of the fluid elements. Thus the jet is deflected to the surface and becomes a tangential wall jet. The reason for this behaviour is low pressure between the jet and the solid surface. Due to the momentum transport from the jet to the stationary or slowly moving fluid, the flow in the vicinity of the jet is accelerated. Since the wall prevents fluid inflow into the area between the jet and the wall, pressure decreases. The emerging pressure gradient normal to the wall generates a force, which moves the jet flow towards the wall. This effect applies for jets along straight and curved walls and hence tangential blowing can be used to achieve large turning of the flow over airfoils.

Investigations by Englar and Hemmerly[15] showed that the Coanda effect works best when the slot height is about 1% to 5% of the curved surface radius and the slot height is about one to two per mil of the chord length.

The driving parameter for the Coanda effect is the dimensionless momentum coefficient, c_μ, of the jet, which is defined as follows:

$$c_\mu = \frac{v_{jet}\ \dot{m}_{jet}}{\frac{1}{2}\,\rho_\infty\, v_\infty^2\, S} \tag{1}$$

It is important to notice that the increase of the lift coefficient is much higher than the used dimensionless momentum coefficient. So the lift gain is due to flow separation control and super circulation and does not arise because the momentum of the jet is directed downwards.

III. Model Design for Wind Tunnel Experiments

III.A. 2D-Airfoil Design

Numerical simulations of the flow around profiles using circulation control are conducted to find favourable geometries with low momentum coefficients. As a starting point for two-dimensional investigations of circulation control a modern transonic airfoil was chosen, which can be seen in **Figure 1**.

The results shown in this paper are given for a slot height of one per mil of the chord length. The design of the profile with circulation control has been done in a way to retain the characteristics of the basic profile at cruise conditions.

First the x-wise position of the slot is defined, which also determines the length of the flap. Upstream of this position the original upper surface is used. Downstream of the vertical slot the upper surface of the flap has to be defined. Thus the slot is positioned directly upstream of the flap. There are two basic design constraints for the flap geometry. On the one hand the Coanda radius should be as large as possible to enhance the Coanda effect. On the other hand the profile should be well suited for cruise flight, which means

that it needs a thin trailing edge like the basic airfoil and the flap contour should be as close as possible to the shape of the basic profile. There are three general options of designing the upper surface of the flap, which are displayed in **Figure 2**.

In version A the Coanda radius is hidden in the profile during cruise flight conditions. When the slot is closed for cruise the circulation control profile and the basic airfoil are identical. If the flap is deflected for take-off and landing the Coanda radius appears downstream of the slot.

In version B the upper surface downstream of the flap is translated downwards to create the slot. During cruise the upper surface of the flap is slightly recessed and there is a small step at the position of the slot. As for version A the Coanda radius is hidden when the flap is not deflected. Note that the exact position of the hinge line can be used to obtain continuity in surface slope with version A and B. This feature is not shown in **Figure 2**.

Version C describes a dual-radius flap, which was first mentioned by Englar.[15] Here the upper surface of the flap is composed out of two circle segments. The first circle segment is hidden in cruise. Its radius is chosen as large as possible, i.e. corresponding to about the local thickness of the profile at the slot position as for version A and B. The radius of the second segment is chosen in a way that the position of the trailing edge stays unchanged. Since the second segment represents a circle of very large radius, the new shape of the upper surface stays very close to the original contour in **Figure 1**.

A large high-lift flap with a flap length of $c_{flap}/c = 0.3$ was designed according to version B to numerically assess its high-lift characteristics. Furthermore a dual-radius flap (type C) was realised with a flap length of $c_{flap}/c = 0.07$. Both flap geometries can be seen in **Figure 3**.

To obtain a realistic flow at the slot exit a converging duct was designed, which has a length of seven times the height of the slot. At the inflow position the duct is two times as wide as at the slot exit to ensure that the jet is accelerated until it reaches the exit. The duct shape is depicted in **Figure 4**.

III.B. Numerical 2D-Simulation

The flow around profiles utilising trailing edge blowing is simulated by solving the Reynolds-averaged Navier-Stokes equations using the DLR hybrid unstructured flow solver TAU, which is based on a finite volume scheme.[16,17] The code processes meshes with different types of cells and combines the advantages of structured grids to resolve boundary layers with the flexible grid generation of unstructured grids. To accelerate the convergence to steady state, techniques like local time stepping, residual smoothing and multi grid based on agglomeration of the dual-grid volumes are available. All preliminary two-dimensional computations were undertaken assuming the boundary layer to be fully turbulent and with the Spalart-Allmaras[18] turbulence model, which has proven its general capability of computing the flow fields around profiles with circulation control, using simulations of the experimental results achieved by Novak[6] for an elliptical profile with circulation control.[19,20]

The numerical investigations using TAU simulate the flow around the profile at free stream conditions. Free stream values were chosen according to the standard atmosphere (i.e. $0m$ for take-off and landing but $10500m$ for cruise flight) for a Reynolds number that represents the wing of a 260-seat passenger aircraft. The total pressure and total temperature of the pressurised air used for circulation control were chosen corresponding to the flow conditions in the exhaust of a modern shrouded high-bypass engine. For take-off the following conditions were chosen: $p_{t,jet}/p_\infty = 1.68$ and $T_{t,jet}/T_{t,\infty} = 1.63$.

For all geometries the total number of grid points is about $0.7 \cdot 10^5$ (see **Figure 4** for mesh details). The structured area on the surface has a thickness of 48 cells. In the vicinity of the jet slot the grid for the numerical simulation is clustered to capture the jet behaviour correctly. Behind the trailing edge and behind the upper boundary of the duct a wake plane with structured cells is added to achieve a better resolution at these sharp edges.

III.C. Results of 2D-Simulation

A typical computed flow field around the circulation control airfoil with a dual-radius flap is displayed in **Figure 5**. **Figure 6** shows a computed flow field around the circulation controlled airfoil with the large high-lift flap. In **Figure 7** the computed lift coefficients for the two flap geometries (as shown in **Figure 3**) are compared.

For the large high-lift flap and a slot height of $h/c = 0.001$ the momentum coefficient is $c_\mu = 0.043$. When the flap is deflected by $\alpha = 60°$, lift coefficients of up to $c_l = 4.4$ can be achieved. Higher deflection angles shift the angle of maximum lift to smaller values. For a deflection angle of $\alpha = 60°$ the angle of maximum lift is already negative. Note that by doubling the slot height the generated lift is only slightly increased. Hence a profile with a small slot height, such as $h/c = 0.001$, is preferred compared to a larger slot size, because the lift gain per momentum is larger and (as a rough estimate) the percentage of engine bleed air corresponds to the percentage of overall thrust reduction. It can be seen that the much shorter and lighter dual-radius flap achieves lift coefficients of $c_l = 3.2$ for $c_\mu = 0.038$.

In **Figure 8** the lift versus drag performance for different flap deflection angles is shown. To account for the thrust loss due to the bleed air taken from the engine the momentum coefficient c_μ is added to the drag coefficient prior to computing the performance. By decreasing the momentum coefficient to just the value needed to prevent flow separation the effective lift over drag values for lower flap deflection angles can be much improved. Results for the minimum momentum coefficient for three different flap deflection angles are plotted in **Figure 9**.

A detailed analysis of the airfoil stall behaviour with circulation control shows that stall is caused by reversed flow on the flap suction side. Here the Coanda jet still follows the flap contour whereas flow reversal of the wake from the main wing takes place. Note that the implementation of circulation control does not generate higher pitching moments than a modern high-lift profile with slat and Fowler flaps at comparable lift coefficients.

All results for the investigated large high-lift flap (type B) are also applicable for a flap of type A, because the high-lift characteristics of version A and B are almost identical. The cruise performance of a version A flap is identical to the performance of the basic airfoil, since in cruise the geometries are the same. Thus the improved high-lift performance of the investigated large high-lift flap can be achieved without degrading the cruise performance if a flap of version A is used. Therefore no numerical simulations to assess the cruise performance of the large high-lift flap were conducted in the course of this study.

For the dual-radius flap the slot is closed with a straight cap in cruise. The reference profile generates a drag cofficient $c_d = 0.0073$ at its design point ($Ma_\infty = 0.72, c_l = 0.4$). The dual-radius flap has a drag coefficient of $c_d = 0.0075$ at the design point and thus increases the drag by two drag counts.

III.D. Model Design

For the wind tunnel tests the large high-lift flap (type A, $c_{flap}/c = 0.3$) was selected for the following reasons: With the large high-lift flap significantly larger lift coefficients can be generated for a given momentum coefficient and even when the blowing fails, reasonable lift coefficients can still be achieved. Low momentum coefficients are here assumed as the most important requirements of overall aircraft system design.

As a reference aircraft for the following consideration, an airplane for 260 passengers, a wing area of $S = 244m^2$ and a maximum take off weight of $m = 134\,t$ is chosen. For take off the reference aircraft needs a high-lift system, which can generate a two-dimensional lift coefficient of about $c_l \approx 2.7$. The large high-lift flap with circulation control can provide the necessary lift for take off with flap deflections of $\eta = 20°$ (see **Figure 7**). For landing much higher lift coefficients are needed in combination with large drag coefficients. The reference aircraft requires a necessary two-dimensional lift coefficient of about $c_l \approx 3.7$ for the high-lift system. This can be achieved with a flap deflected by $\eta = 40°$, this time for an angle of attack of $\alpha = 4°$. Therefore the model features a flap deflection angle of $\eta = 40°$ to investigate the most important configuration.

In order to achieve a two-dimensional flow around the circulation controlled airfoil and to keep wall interference as small as possible, the aspect ratio of the model should be large. Therefore the chord has to be as short as possible. On the other hand the Reynolds number should be as large as possible to reduce the influence of low Reynolds number effects. As a reasonable compromise a chord length of $c = 0.3m$ was chosen for the wind tunnel model, which yields an aspect ratio of $\Lambda = 4.3$ and a Reynolds number of $\mathrm{Re} = 1 \cdot 10^6$. A profile with this length also provides sufficient space for the ducting of the pressurised air.

With the geometric parameters defined, the wind tunnel model was manufactured. The model design is displayed in **Figure 10**. The necessary mass flow of pressurised air used for circulation control is supplied into the model using both lateral sides of the wing. Thereby the total pressure distribution in the duct becomes more homogeneous and symmetrical in spanwise direction. Before the wind tunnel testing the uniformity of the static pressure in the plenum in spanwise direction was checked by pressure measurements at five positions in the model. For medium feed pressures corresponding to momentum coefficients around $c_\mu = 0.04$ the mean absolute deviation of the static pressures in the plenum was less than 0.1%.

To analyse the jet distribution in spanwise direction the dynamic pressure in the jet $0.02m$ downstream of the slot was measured for different feed pressures. For that reason a small Pitot tube was traversed in spanwise direction. To always measure the same location inside the jet, the probe was kept in close contact to the wall. The results are plotted in **Figure 11**. Here η is the normalised spanwise coordinate of the probe position. It can be seen that the mean absolute deviation is always less than 10%. Thus we can assume an almost constant momentum coefficient of the jet in spanwise direction over the whole model, which is an important requirement to obtain two-dimensional flow in the middle of the airfoil. It is important to mention that this data cannot be used to determine the jet velocity, as because of its size the probe measures an averaged pressure over a certain boundary layer height. Measurements of the slot yielded a slot height of $h/c = 0.0011$ with a deviation of less than $\Delta h/c = 0.0001$.

IV. Wind Tunnel Experiments

The experimental investigations were conducted in the low speed wind tunnel of the Technische Universität Braunschweig, which is a closed-return atmospheric tunnel with a $1.3m$ x $1.3m$ closed test section. An opening angle of $\gamma = 0.2°$ of the floor and ceiling of the test section compensates for the boundary layer growth. In the measurement section a maximum speed of $55m/s$ can be achieved. A heat exchanger in the settling chamber allows constant flow temperature.

The wind tunnel model with circulation control was investigated at a free stream velocity of $v_\infty = 50m/s$, which results in a Mach number of $\mathrm{Ma}_\infty = 0.15$ and a Reynolds number of $\mathrm{Re} = 1 \cdot 10^6$. To analyse the performance of the airfoil for different momentum coefficients the static pressure of the pressurised air provided by a blower could be varied from ambient pressure to $p_{blower}/p_\infty = 2$. To determine the momentum coefficient of the jet, the mass flow from the slot and the jet velocity are needed. To measure the massflow into the airfoil, a flow measuring device is connected to the piping. When the total pressure and the total temperature of the air in the plenum and the static pressure at the slot is measured, the jet velocity can be computed, using the equations for compressible flow and assuming an isentropic change of state from the plenum to the slot. To account for non isentropic losses an efficiency factor for the expansion was evaluated based on numerical simulations of the flow: $\eta_{expansion} = \Delta h/\Delta h_s = v_{jet}^2/v_{jet,s}^2 = 0.89^2$. Thus the momentum coefficient for all experiments could be computed.

The strong suction peak at the airfoil nose causes large laminar flow separation bubbles with a strong effect on the overall airfoil flow. Therefore a zigzag strip was glued very close to the leading edge. The thickness of this transition strip was chosen as $25\mu m$, by which overtripping could be avoided.

To check for two-dimensional separation behaviour of the airfoil, tufts were attached to the upper surface. The flow separation always started in the centre of the airfoil as there was the highest aerodynamic load and then started to grow towards the side walls.

The pressure distribution around the airfoil was measured for different momentum coefficients. For each analysed momentum coefficient the measurements started at an angle of attack of $\alpha = -5°$. The angle of

attack was than gradually increased until the flow separated from the airfoil. The pressure distribution on the model surface was measured by 63 pressure taps, which are positioned in the plane of symmetry of the airfoil. The pressure taps were distributed to offer high resolution at the leading edge and on the Coanda surface to capture the suction peaks with sufficient accuracy. There was also one pressure tap in the trailing edge, which features a thickness of $d/c = 0.004$.

Using the measured pressure distribution the force normal to the airfoil chord could be computed. In **Figure 12** the normal force coefficients c_n are shown for seven different momentum coefficients between $c_\mu = 0.020$ and $c_\mu = 0.054$. For comparison the normal force coefficients of the airfoil without blowing are also plotted, here the flow over the flap is fully detached for each angle of attack. When the momentum coefficient of the jet is increased, the normal force is increased as well, whereas the angle of attack, for which the maximum normal force is achieved, decreases. The gain in normal force for increasing the momentum coefficient becomes smaller for higher momentum coefficients. For small momentum coefficients the blowing works as boundary layer control, the momentum of the jet results in a later separation of the flow on the upper surface of the flap. When the flow stays attached up to the trailing edge, the end of boundary layer control is reached; a further increase in jet momentum results in super circulation. For super circulation the normal force is still increased by increasing the momentum coefficient. However, the efficiency of the flow control device $\Delta c_n/\Delta c_\mu$ is reduced. This can be seen in **Figure 13**, where the gain in normal force coefficient is plotted over the corresponding momentum coefficient for an angle of attack of $\alpha = 0°$. For the investigated airfoil super circulation starts for momentum coefficients larger than $c_\mu = 0.043$.

To measure the drag of the airfoil a wake rake was used at a distance of $d/c = 1.24$ behind the trailing edge in the plane of symmetry. Using the measured drag coefficients the normal force coefficients could be converted to lift coefficients. Measured drag and lift coefficients for five different momentum coefficients are displayed in **Figure 14**. For large momentum coefficients the drag coefficients are negative, resulting in airfoil thrust. The thrust is larger for larger momentum coefficients. If the momentum coefficient is added to the drag coefficient to eliminate the momentum of the jet from the drag measurement, only the pressure drag and the friction drag of the airfoil remain. This airfoil drag distribution is very similar for all configurations as long as the flow is fully attached to the flap. This can be seen in **Figure 15**. Only a part of the graph for $c_\mu = 0.032$ and $c_\mu = 0.038$ differs from the rest, as for these cases the flow starts to separate from the flap surface if the angle of attack is increased. The angle of attack for which separation starts can also be determined from **Figure 12**, where the slope of the graphs for $c_\mu = 0.032$ and $c_\mu = 0.038$ displays a sudden change when separation occurs on the upper surface of the flap.

Particle image velocimetry was used to measure the velocity field over the flap in the centre of the airfoil. Therefore a Quantel Brilliant double pulsed Nd:YAG laser with an energy of $E = 150mJ$ per pulse was used to illuminate a flow parallel light sheet in the middle of the wind tunnel. As seeding, oil particles with a diameter of about $1\mu m$ were employed. A LaVision Imager ProX 11M with a resolution of 4008 x 2672 pixels was used to capture the particle images. For data acquisition and data evaluation, Davis7.2 by LaVision was used.

One set of measurements was done to visualize the velocity field above the flap and behind the airfoil to determine the momentum coefficient for which the flow stays attached to the surface. To reduce reflections of the laser light from the airfoil surface, the model surface was polished. Thousand images with a size of $220mm$ x $180mm$ were taken for momentum coefficients of $c_\mu = 0.026$, $c_\mu = 0.038$, $c_\mu = 0.043$ and $c_\mu = 0.049$ for angles of attack of $\alpha = -2°$, $\alpha = 0°$ and $\alpha = 2°$.

Once the particle image acquisition of 1000 image pairs for each measurement was completed, the velocity vector field of the flow around the airfoil had to be determined. After several image preprocessing techniques to improve the particle image quality, the particle displacement evaluation was executed in the next step using a cross correlation scheme. Here a multipass interrogation scheme was applied with decreasing interrogation window size from 128 x 128 pixels down to 16 x 16 pixels, 50% overlap and window shifting and deformation. With a $105mm$ lens a spatial resolution of the obtained vector field of $0.6mm$ in both directions was achieved. The resulting set of 1000 vector fields for each measurement was then post-processed. It was necessary to filter out non physical vectors, which would corrupt the results of the ensemble averaging procedure. Only

if in at least 250 vector fields a valid vector was found at a certain position an average velocity vector for this position was computed.

The computed average flow field above the flap for a momentum coefficient of $c_\mu = 0.026$ and an angle of attack of $\alpha = 0°$ is displayed in **Figure 16**. It can be seen that the flow on the upper surface of the flap does not stay attached up to trailing edge. For a momentum coefficient of $c_\mu = 0.043$ the velocity field is plotted in **Figure 17**. Here the flow is fully attached to the trailing edge and the wake has a larger inclination, which demonstrates the increased circulation.

The second set of images was taken with a much higher resolution using a teleconverter and a $180mm$ lens in order to measure the boundary layer profile upstream of the slot. With this setup the obtained vector field yields a spatial resolution of $0.3mm$ in both directions. The first velocity information is gained in a distance of $d/c = 0.001$ to the wall. Due to the necessary higher laser power per volume needed for the higher resolution the reflections of the laser light become more severe. Therefore the area upstream of the slot was coated with a thin reflective foil with a thickness of $s = 25\mu m$. The foil was replaced after every thousand double exposures. One thousand images with a size of $62mm$ x $50mm$ were taken for the same parameter space as for the first setup. For this set of images the size of the final window of the multipass interrogation scheme had to be increased to 32 x 32 pixels. Again an average velocity vector was computed only for positions where at least in 250 vector fields a valid vector was found.

In **Figure 18** and **Figure 19** the velocity fields in the vicinity of the slot are displayed for a momentum coefficient of $c_\mu = 0.026$ and $c_\mu = 0.043$, both measurements are given for an angle of attack of $\alpha = 0°$. For the higher momentum coefficient the higher velocity in the shear layer next to the jet can be seen as well as the higher acceleration of the boundary layer upstream of the slot. In **Figure 26** the extracted velocity profiles for an angle of attack of $\alpha = 0°$ at a position of $x/c = 0.65$ are plotted for different momentum coefficients. The velocity profile of the jet could not be determined as the jet was not yet seeded with particles.

V. Numerical Simulation of Wind Tunnel Experiments

The flow around the wing utilising circulation control was simulated by solving the Reynolds-averaged Navier-Stokes equations, using the DLR hybrid unstructured flow solver TAU again. To increase the accuracy of the three-dimensional simulations, low speed preconditioning was used. The viscous walls of the test section were also simulated to obtain realistic results for the flow around the wind tunnel model. For efficient flow computations the chimera technique was employed with a local grid defined around the airfoil. The chimera technique allows using an already attained solution as a restart for a following simulation with a different angle of attack. Using the chimera technique to gradually increase the angle of attack, the flow in the vicinity of maximum lift can be simulated correctly.

In **Figure 20** the spatial discretization of the wind tunnel test section can be seen. This hybrid mesh consists of $6 \cdot 10^6$ nodes. The cylindrical mesh around the model is positioned in the cylindrical hole of the background mesh. This local mesh, which is composed of $14 \cdot 10^6$ nodes, is displayed in **Figure 21** and can be rotated around its centreline. This centreline is identical to the axis of rotation of the wind tunnel model. Thus the chimera technique can be used to account for the hysteresis effect of the separation.

The structured area on the surface of the wing has a thickness of 40 cells. On the walls of the wind tunnel 32 prismatic layers were generated. The nondimensional first grid spacing normal to the wall is smaller than 1.5 on most parts of the surface of the wing, except for local values of about 5 at the nose and on the Coanda surface due to the locally very high velocities. In the vicinity of the jet slot and the trailing edge the grid for the numerical simulation is clustered to capture the jet behaviour correctly.

First simulations of the flow field around the wind tunnel model are performed with the standard ***S**palart-**A**llmaras* (SA) turbulence model without any curvature correction. In **Figure 22** the c_p-distribution on the model surface and the surface streamlines are shown for an angle of attack of $\alpha = -5°$ and a momentum coefficient of $c_\mu = 0.055$. This result corresponds to the highest momentum coefficient of $c_\mu = 0.054$ investigated in the experiments. Only one half of the symmetric model is shown in **Figure 22**. The

backward side in the figure is the location of the wind tunnel side wall. The computed flow field shows that almost two-dimensional flow can be assumed in the middle of the measurement section. The c_p-distribution for an angle of attack of $\alpha = 0°$ and a momentum coefficient of $c_\mu = 0.055$ can be seen in **Figure 23**. Due to the higher angle of attack the pressure on the upper surface is reduced and thus the lift increases.

Oil with fluorescent particles was used in the experiment to visualize the surface streamlines on the airfoil and on the wall of the wind tunnel. The photos taken can be used to assess the interaction of the wall boundary layer with the flow around the airfoil. In **Figure 24** the oil flow on the side wall of the measurement section can be seen for an angle of attack of $\alpha = -5°$ and a momentum coefficient of $c_\mu = 0.043$. The horseshoe vortex is clearly seen. The same flow field topology can be found in **Figure 25**. Here the simulated surface streamlines and the c_p-distribution on the wall for the same angle of attack and a momentum coefficient of $c_\mu = 0.042$ are displayed.

In **Figure 26** velocity profiles attained by particle image velocimetry are compared with the simulated velocity profiles in the boundary layer at the midspan position of $x/c = 0.65$, which is $15mm$ up-stream of the slot. All velocity profiles are given for an angle of attack of $\alpha = 0°$. For higher momentum coefficients the velocity is increased. The general behaviour as well as the shape and the boundary layer thickness are well predicted by using the SA turbulence model. However the velocity at the edge of the boundary layer is about 5% too small for all investigated momentum coefficients. At this point it is assumed that the experimental calibration of the freestream velocity by the wind tunnel nozzle factor is affected by the high-lift airfoil in the test section and this causes the observed dicrepancies.

In order to compute the c_p-distribution, the pressure at the ceiling and the floor in the plane of symmetry of the test section at a position of 9.5 chord length behind the airfoil was averaged and used as reference pressure. This was done for the experimental data as well as for the numerical data. In **Figure 27** and **Figure 28** the measured c_p-distributions for a high momentum coefficient of $c_\mu \approx 0.055$ for an angle of attack of $\alpha = -5°$ and $\alpha = 0°$ are compared with the results of the numerical simulations. In **Figure 29** and **Figure 30** the measured c_p-distributions for a medium momentum coefficient of $c_\mu = 0.032$ for the same angles of attack are again compared with the results of the numerical simulations. The good agreement of the numerical and the experimental results demonstrates the capability of the SA turbulence model to simulate the flow around a circulation control airfoil with a sharp trailing edge. More simulations for higher angles of attack have to be conducted to analyse the capability of the SA turbulence model to predict the flow in the proximity of maximum lift.

Numerical simulations are also performed to assess the effect of shear flow curvature for the present flow configuration. Therefore further computations are conducted with the SARC model (SARC: ***S**palart-**A**llmaras* model for **R**otation and/or **C**urvature effects).[21] The obtained c_p-distribution by using the SARC model for $c_\mu = 0.032$ and $\alpha = 0°$ is plotted in **Figure 31**. The pressure around the model virtually does not change. However a small separation on the edge of the flap, which has a size of 2% of the chord length when the standard SA turbulence model is applied, increases to a size of 5%.

VI. Conclusions

The experimental investigation of an airfoil with circulation control using an internally blown high-lift flap yields high normal force coefficients at comparably low momentum coefficients. Pressure distributions along the airfoil, wake probing, PIV measurements and oil flow pictures are obtained to establish a data set useful for validating numerical simulation methods. First numerical simulations show a good agreement with the measured data, even if a simple one equation turbulence model without curvature correction is used. More numerical simulations have to be conducted to see if the same good agreement can be achieved for maximum lift and if the momentum coefficient and the angle of attack for which separation starts can be predicted as well.

Acknowledgments

The present work is performed as a part of the European research project TimpAN (Technologies to IMProve Airframe Noise), which is part of the sixth framework programme. This project is founded by the European Commission and is coordinated by Airbus France. The authors thank the "Norddeutscher Verbund für Hoch- und Höchstleistungsrechnen" (HLRN) for providing the necessary computational resources.

References

[1]Bamber, M.J.: *Wind tunnel tests on airfoil boundary layer control using a backward-opening slot*, NACA Report 385, 1932.

[2]Hagedorn, H. and Ruden, P.: *Windkanaluntersuchungen an einem Junkers-Doppelflügel mit Ausblaseschlitz am Heck des Hauptflügels*, Bericht A 64 der Lilienthal-Gesellschaft für Luftfahrtforschung, 1938.

[3]Davidson, I. M.: *Aerofoil boundary layer control system*, British Patent No.913,754, 1960.

[4]Kind, R. J., Maul, D. J.: *An experimental investigation of a low-speed circulation controlled airfoil*, The Aeronautical Quarterly, Vol. XIX, May 1968, pp.170-182.

[5]Stevenson, T. A., Franke, M. E., Rhynard, W. E. and Snyder J. R.: *Wind-tunnel study of a circulation control elliptical airfoil*, AIAA Journal of Aircraft Vol.14, No. 9, 1977, pp.881-886.

[6]Novak, C. J.,Cornelius, K. C. and Roads R. K.: *Experimental investigations of the circular wall jet on a circulation control airfoil*, AIAA Paper 87-0155, 1987.

[7]Thomas, F.: *Untersuchungen über die Grenzschichtbeeinflussung durch Ausblasen zur Erhöhung des Auftriebes*, Technische Universität Braunschweig, doctoral thesis, 1961.

[8]Körner, H. and Löhr, R.: *Dreikomponentenmessungen am Modell eines leichten STOL-Flugzeuges mit Ausblasen in Flügeltiefenrichtung*, Deutsche Forschungs- und Versuchsanstalt für Luft- und Raumfahrt, DLR-FB 75-74, 1975.

[9]Englar, R. J.: *Overview of circulation control pneumatic aerodynamics: Blown force and moment augmentation and modification as applied primarily to fixed-wing aircraft*, In: Joslin, D., Jones, G. S. (editors): Applications of circulation control technology, Progress in Astronautics and Aeronautics, Vol.214, AIAA, 2006, pp.23-68.

[10]Loth, J. L.: *Advantages of combining BLC suction with circulation control high-lift generation*, In: Joslin, D., Jones, G. S. (editors): Applications of circulation control technology, Progress in Astronautics and Aeronautics, Vol.214, AIAA, 2006, pp.3-21.

[11]Jones, G. S., Yao, C.-S. and Allan, B. G.: *Experimental investigation of a 2D supercritical circulation-cotrol airfoil using particle image velocimetry*, AIAA Paper 2006-3009, 2006.

[12]Baker, W. J. and Paterson, E. G.: *Simulation of steady circulation control for the general aviation circulation control (GACC) wing*, 2004 NASA-ONR Circulation Control Workshop, March 2004.

[13]Slomski, J. F.,Chang, P. A. and Arunajatesan, S.: *Large eddy simulation of a circulation control airfoil*, 2004 NASA-ONR Circulation Workshop, March 2004.

[14]Pfingsten, K. C. and Radespiel, R.: *Numerical Simulation of a wing with a gapless high-lift system using circulation control*, Notes on Numerical Fluid Mechanics and Multidisciplinary Design, Vol. 96, C. Tropea, Springer, Berlin, 2007.

[15]Englar, R.J. and Hemmerly, R.A.: *Design of the circulation control wing STOL demonstrator aircraft*, AIAA Journal of Aircraft Vol.18, No. 1, 1981, pp. 51-58.

[16]DLR: *Technical Documentation of the DLR TAU-Code*, Institut für Aerodynamik und Str/"omungsmechanik, Braunschweig, Göttingen, 2006.

[17]Gerhold, T.: *Overview of the hybrid RANS code TAU*, MEGAFLOW-Numerical Flow Simulation for Aircraft Design Vol.89 Springer-Verlag, 2005 (Notes on Numerical Fluid Mechanics and Multidisciplinary Design), pp.81-92.

[18]Spalart, P. R. and Allmaras, S. R.: *A one-equation turbulence model for aerodynamic flows*, AIAA 92-043, 1992.

[19]Pfingsten, K. C., Jensch, C.,Körber, K. W. and R. Radespiel: *Numerical simulation of the flow around circulation control airfoils*, First CEAS European Air and Space Conference, Berlin, 2007.

[20]Swanson, R. C. and Rumsey, C. L.: *Numerical issues for circulation control calculations*, AIAA Paper 2006-3008, 2006.

[21]Shur, M. L. ,Strelets, M. K., Travin, A. K. and Spalart, P. R.: *Turbulence modeling in rotating and curved channels: Assessing the Spalart-Shur correction*, AIAA Journal, Vol.38, No. 5, 2000, pp. 784-792.

Figures

Figure 1. Basic transonic airfoil (not to scale)

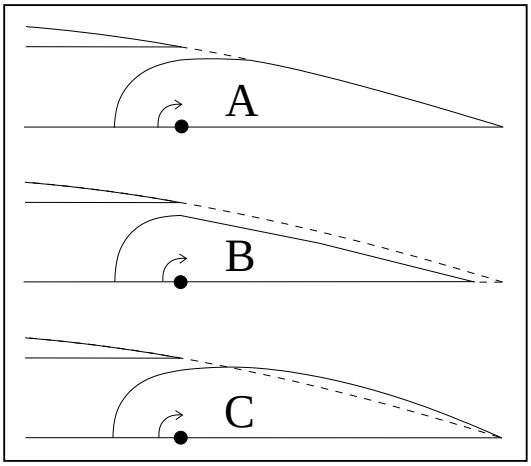

Figure 2. Three options for design of the flap geometry

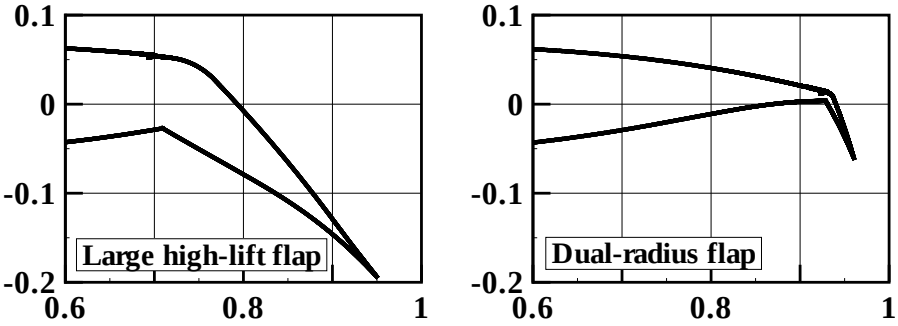

Figure 3. Investigated flap geometries for circulation control

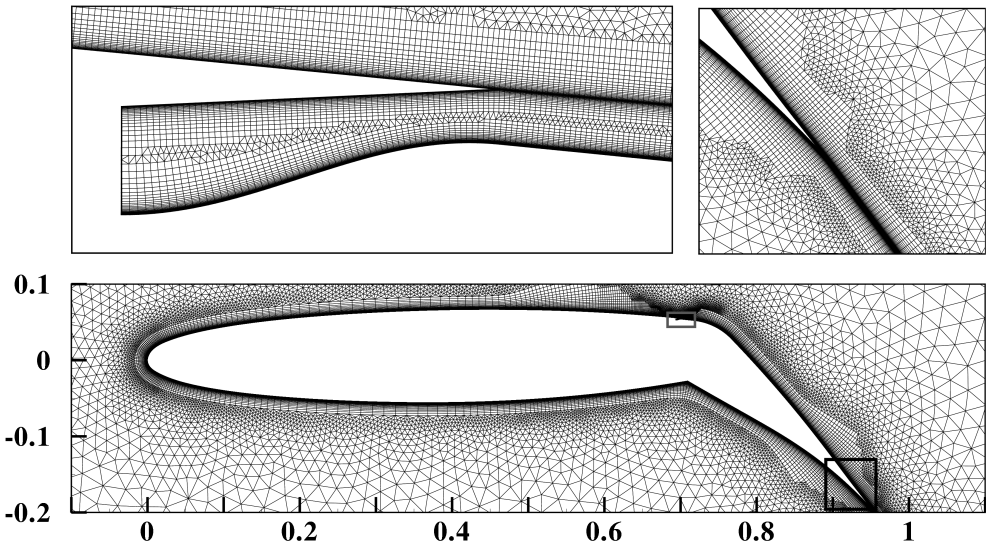

Figure 4. Mesh for circulation control profile with large high-lift flap

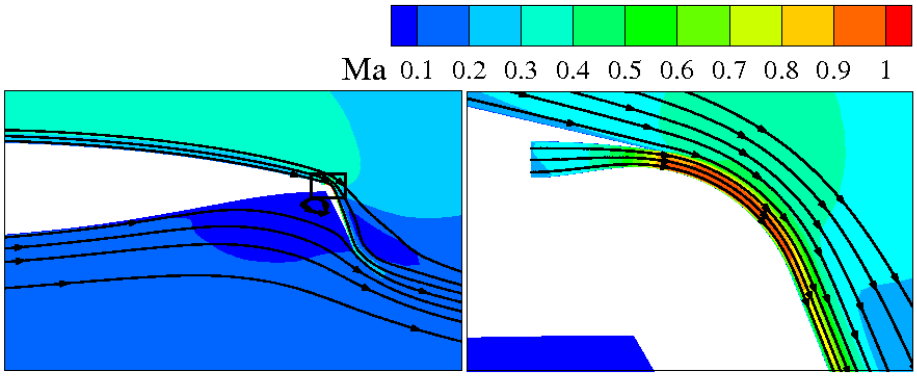

Figure 5. Dual-radius flap: $\mathbf{Ma}_\infty = 0.21$, $\mathbf{Re} = 29 \cdot 10^6$, $c_{flap}/c = 0.07$, $\eta = 60°$, $h/c = 0.001$
$\alpha = 9°$, $c_\mu = 0.038$, $c_l = 3.18$, $c_d = 0.052$, $c_{m,1/4} = -0.46$

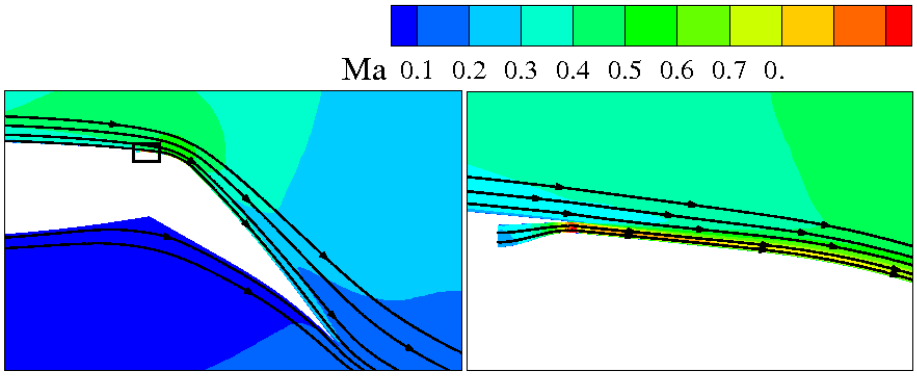

Figure 6. Large high-lift flap: $\mathbf{Ma}_\infty = 0.21$, $\mathbf{Re} = 29 \cdot 10^6$, $c_{flap}/c = 0.3$, $\eta = 40°$, $h/c = 0.001$ $\alpha = 4°$, $c_\mu = 0.043$, $c_l = 3.82$, $c_d = 0.052$, $c_{m,1/4} = -0.58$

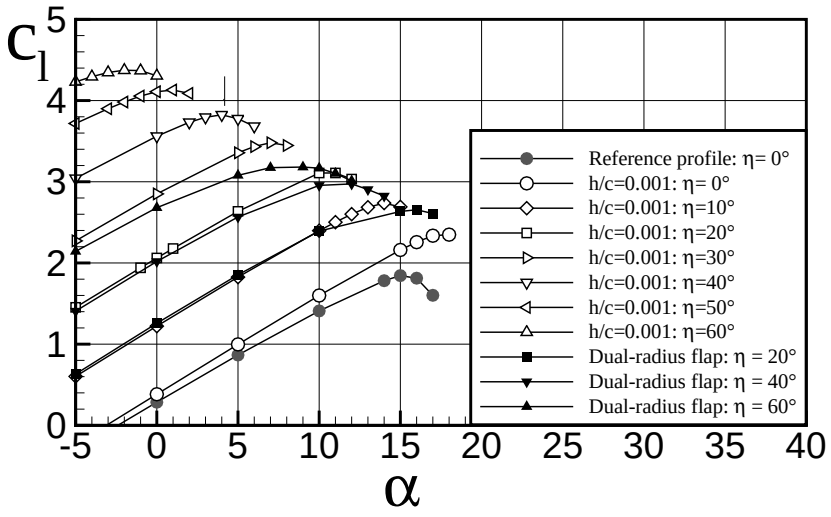

Figure 7. c_l **over** α **for different flap geometries for** $c_\mu = 0.04$ ($\mathbf{Ma}_\infty = 0.21$, $\mathbf{Re} = 29 \cdot 10^6$)

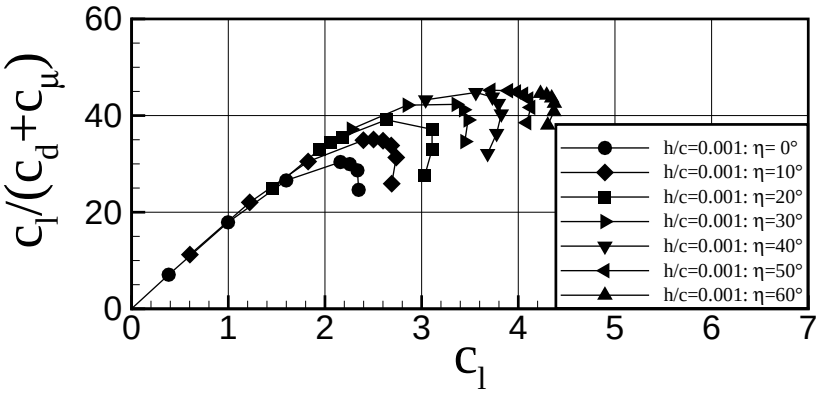

Figure 8. Performance of the large high-lift flap for different deflection angles for $c_\mu = 0.043$ ($\mathbf{Ma}_\infty = 0.21$, $\mathbf{Re} = 29 \cdot 10^6$)

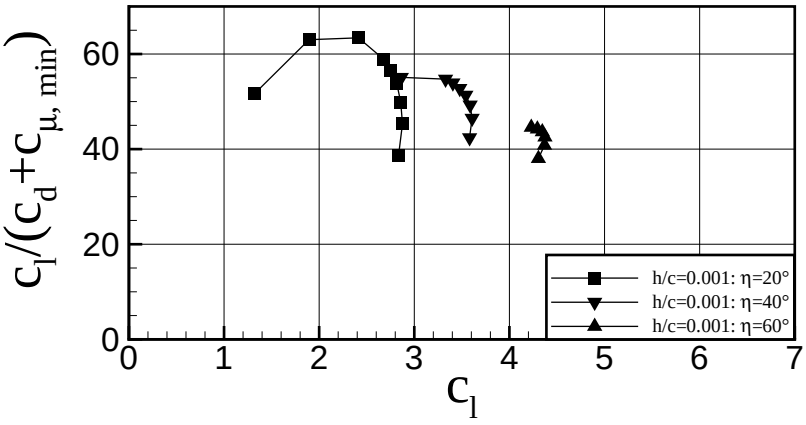

Figure 9. Performance of the large high-lift flap for different deflection angles for $c_{\mu,min}$ ($\mathbf{Ma}_\infty = 0.21$, $\mathbf{Re} = 29 \cdot 10^6$)

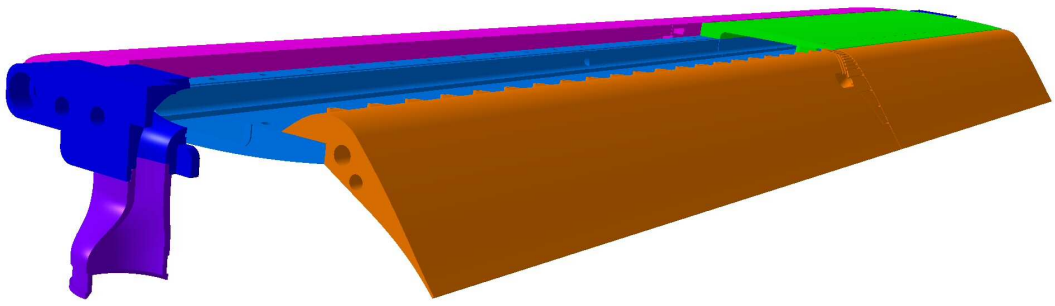

Figure 10. Wind tunnel model with circulation control ducts ($c/c_{flap} = 0.3, h/c = 0.001, \eta = 40°, b/c = 4.3$)

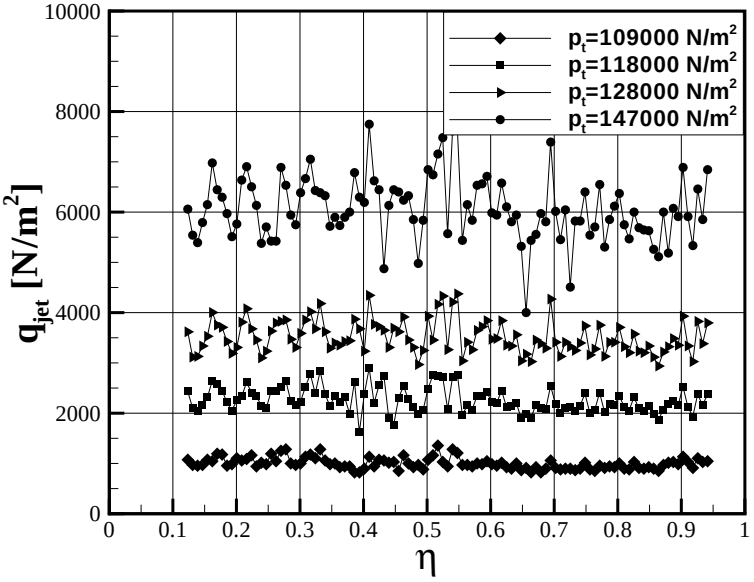

Figure 11. Dynamic pressure distribution in spanwise direction at a position $0.02m$ downstream of the slot

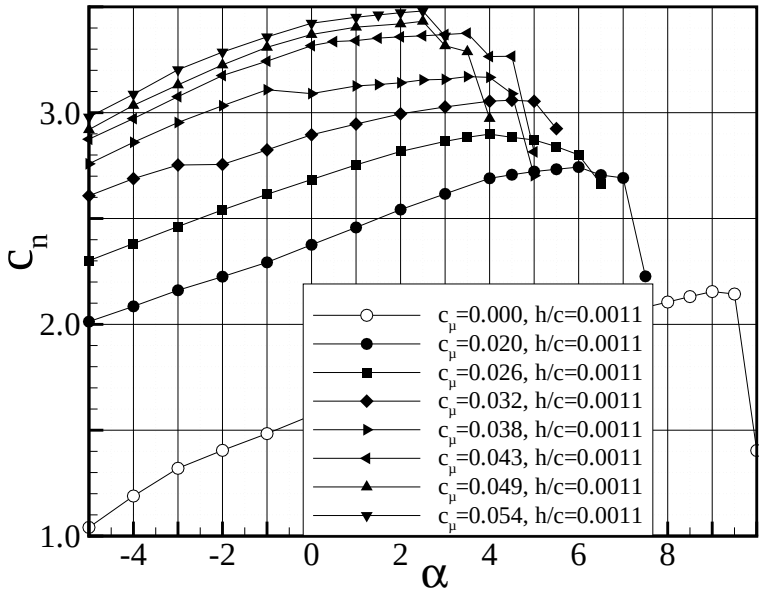

Figure 12. c_n over α for different momentum coefficients ($\mathbf{Ma}_\infty = 0.15$, $\mathbf{Re} = 1 \cdot 10^6$)

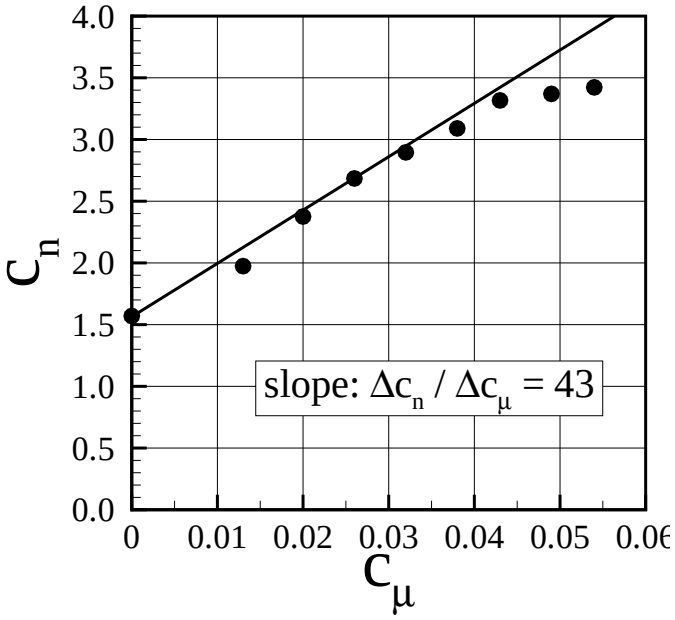

Figure 13. c_n **over** c_μ **for an angle of attack of** $\alpha = 0^\circ$ ($\mathbf{Ma}_\infty = 0.15$, $\mathbf{Re} = 1 \cdot 10^6$)

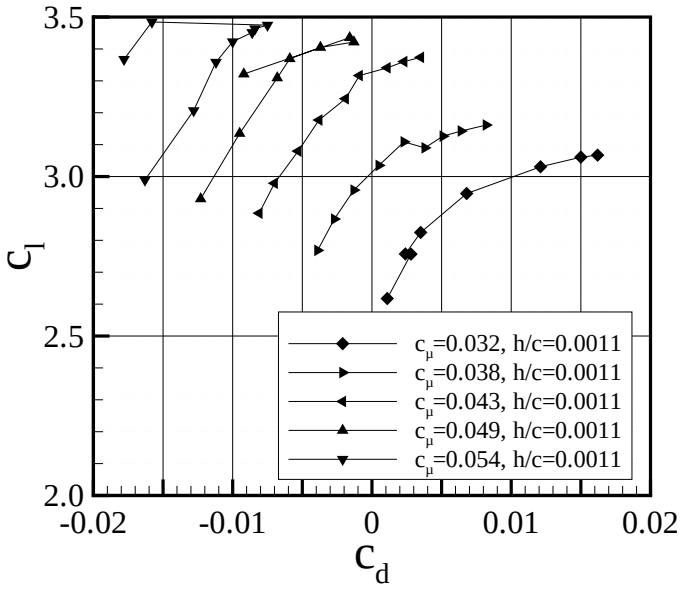

Figure 14. c_l **over** c_d **for different momentum coefficients** ($\mathbf{Ma}_\infty = 0.15$, $\mathbf{Re} = 1 \cdot 10^6$)

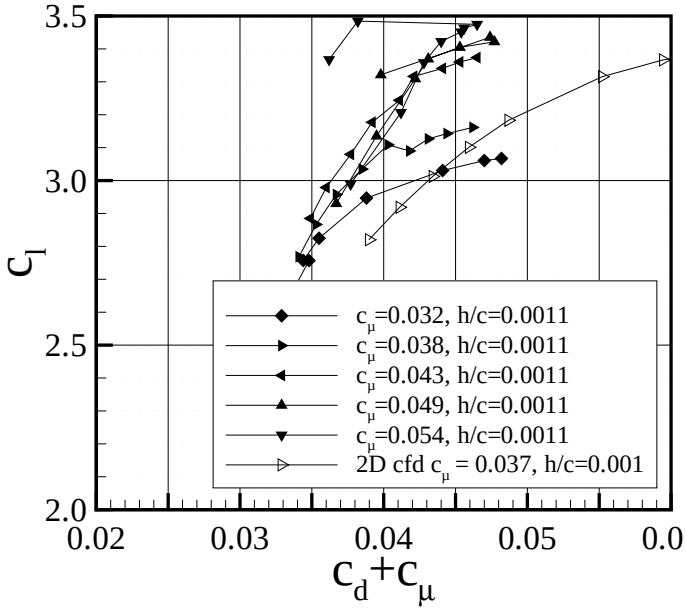

Figure 15. c_l **over** $c_d + c_\mu$ **for different momentum coefficients** ($\mathbf{Ma}_\infty = 0.15$, $\mathbf{Re} = 1 \cdot 10^6$)

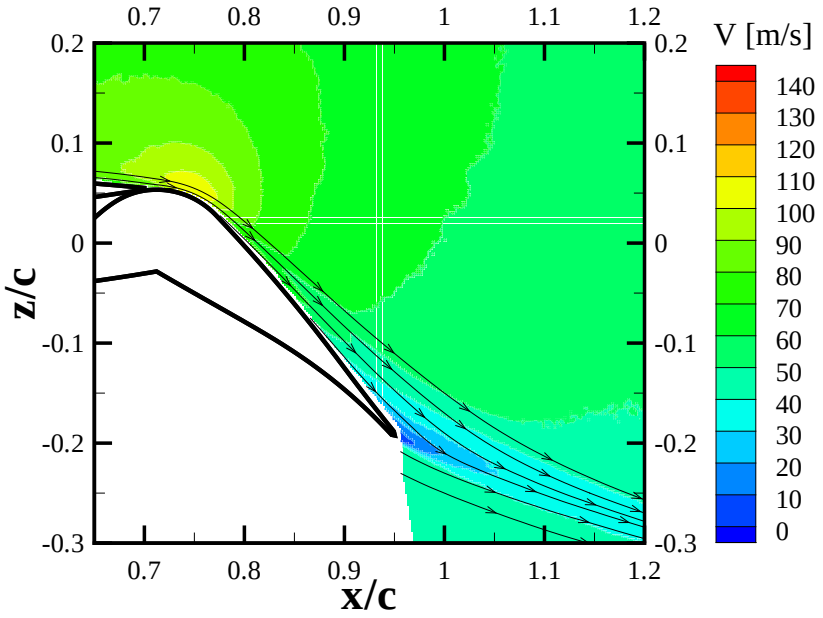

Figure 16. Measured velocity field above the flap for $c_\mu = 0.026$ and $\alpha = 0°$ ($\mathbf{Ma}_\infty = 0.15$, $\mathbf{Re} = 1 \cdot 10^6$)

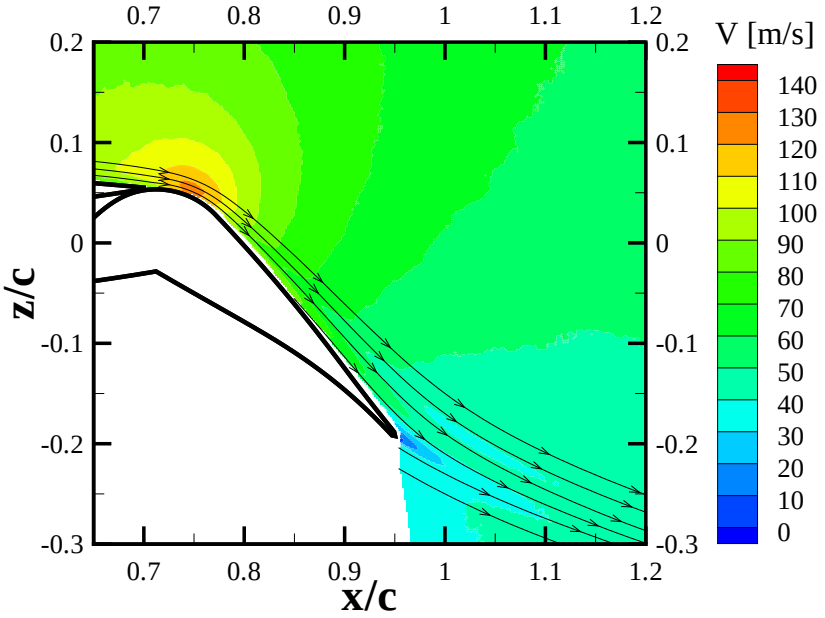

Figure 17. Measured velocity field above the flap for $c_\mu = 0.043$ and $\alpha = 0°$ ($\mathbf{Ma}_\infty = 0.15$, $\mathbf{Re} = 1 \cdot 10^6$)

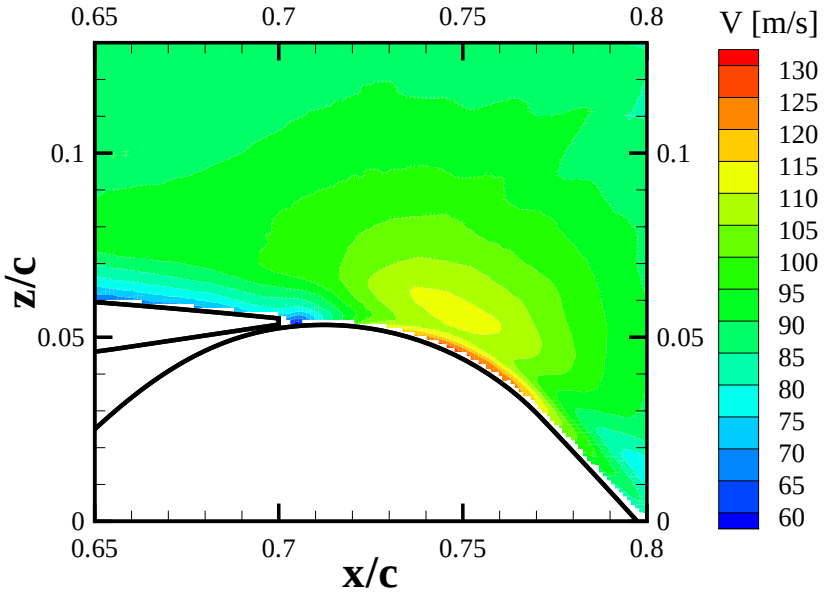

Figure 18. Measured velocity field in the vicinity of the slot for $c_\mu = 0.026$ and $\alpha = 0°$ ($\mathbf{Ma}_\infty = 0.15$, $\mathbf{Re} = 1 \cdot 10^6$)

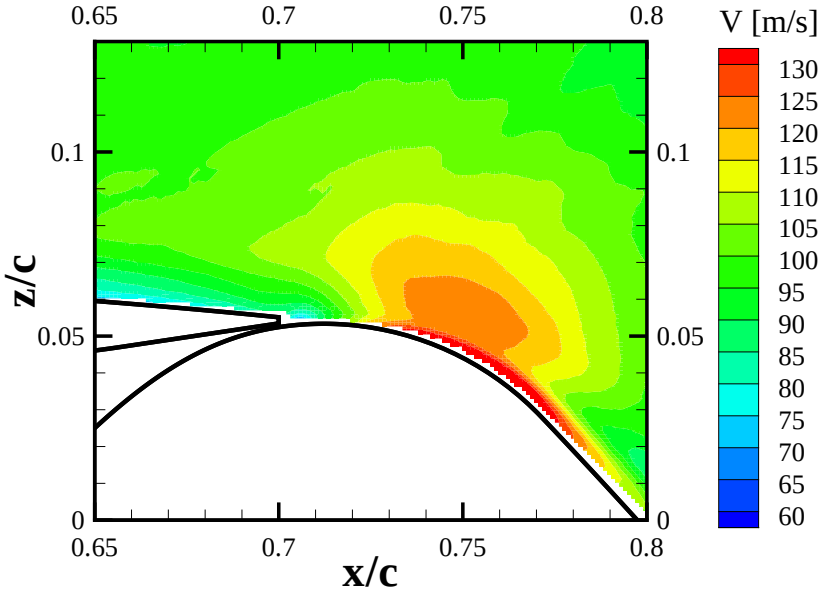

Figure 19. Measured velocity field in the vicinity of the slot for $c_\mu = 0.043$ and $\alpha = 0°$ ($\mathbf{Ma}_\infty = 0.15$, $\mathbf{Re} = 1 \cdot 10^6$)

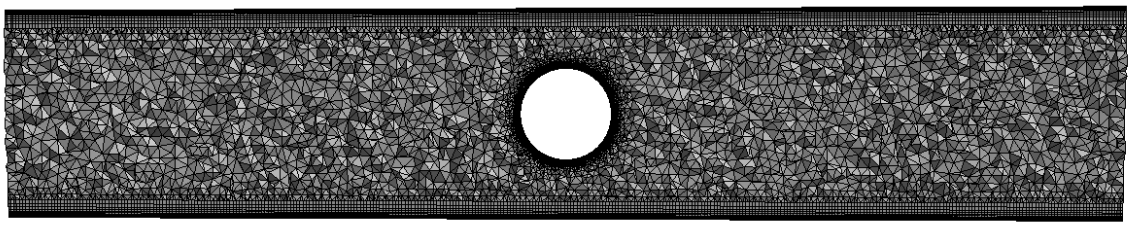

Figure 20. Spatial discretization of the wind tunnel measurement section

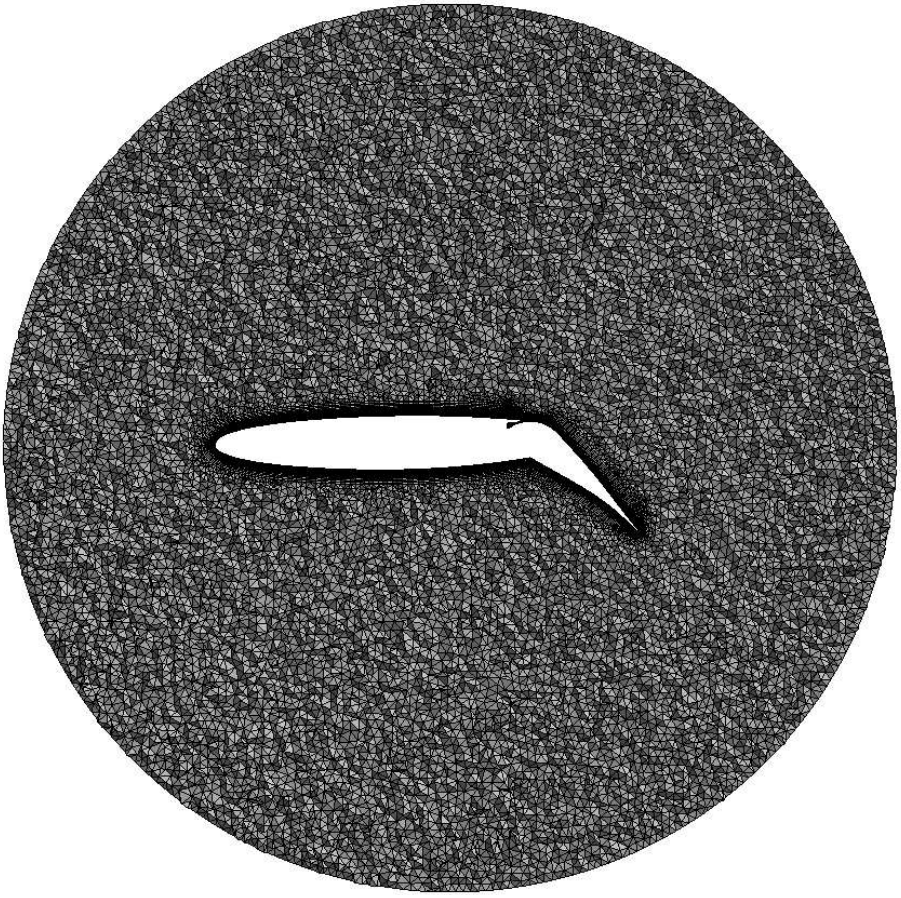

Figure 21. Spatial discretization of the circulation control airfoil

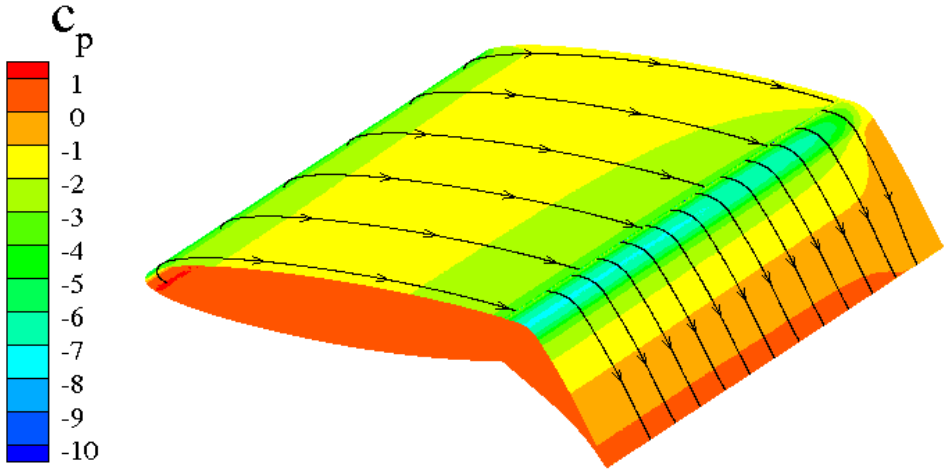

Figure 22. c_p**-distribution and surface streamlines on the wing with circulation control:**
Re $= 1 \cdot 10^6$, **Ma** $= 0.15$, $c_{flap}/c = 0.3$, $\eta = 40°$, $\alpha = -5°$, $c_\mu = 0.055$, $c_L = 2.72$, $c_D = 0.095$, $c_{M,1/4} = -0.60$

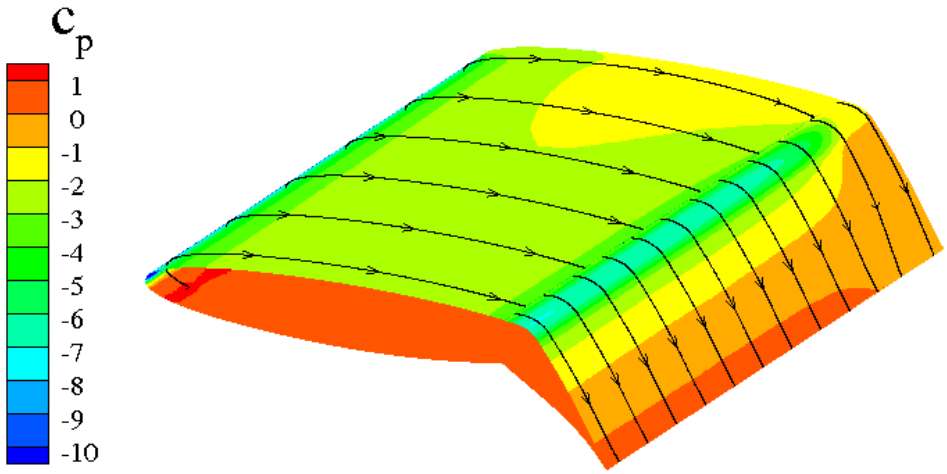

Figure 23. c_p**-distribution and surface streamlines on the wing with circulation control:**
Re $= 1 \cdot 10^6$, **Ma** $= 0.15$, $c_{flap}/c = 0.3$, $\eta = 40°$, $\alpha = 0°$, $c_\mu = 0.055$, $c_L = 3.06$, $c_D = 0.116$, $c_{M,1/4} = -0.56$

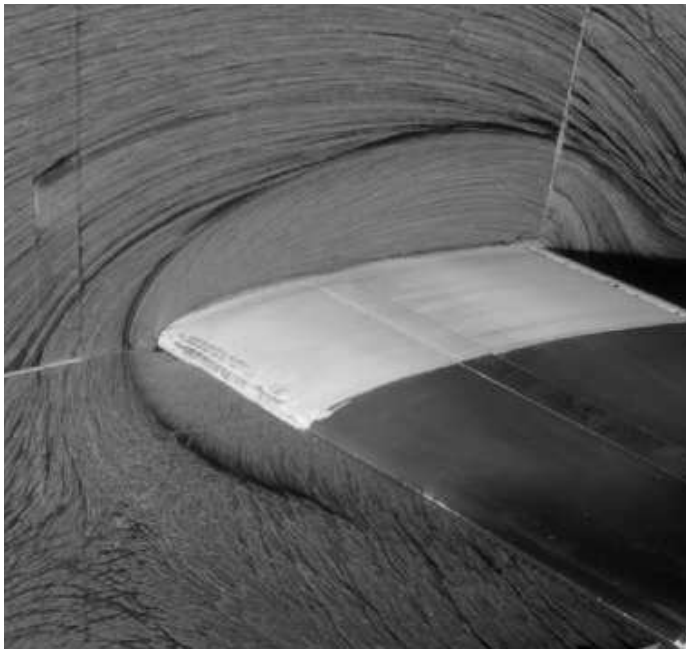

Figure 24. Surface streamlines on the wind tunnel wall:
Re $= 1 \cdot 10^6$, **Ma** $= 0.15$, $c_{flap}/c = 0.3$, $\eta = 40°$, $\alpha = -5°$, $c_\mu = 0.043$

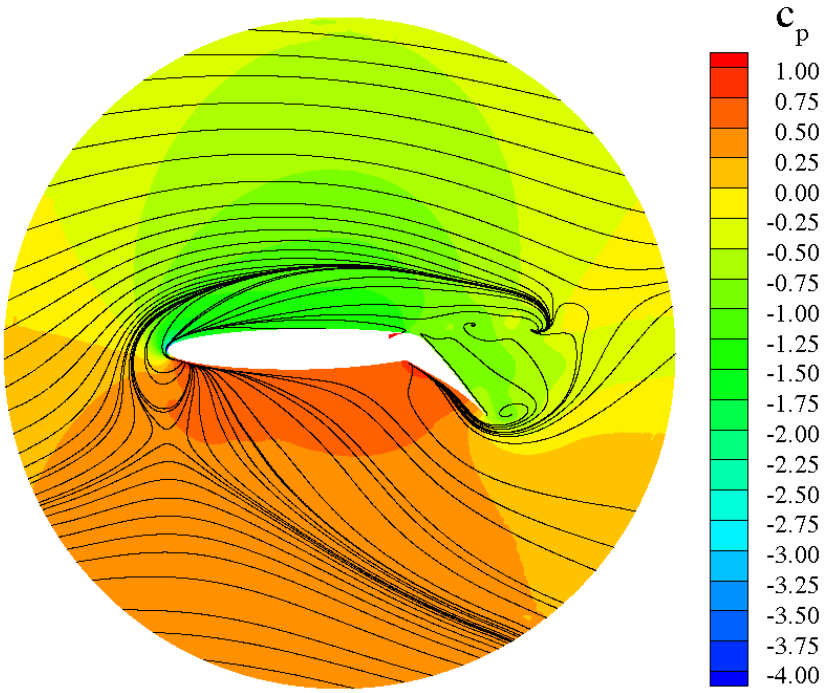

Figure 25. Simulated surface streamlines and c_p-distribution on the wind tunnel wall:
Re $= 1 \cdot 10^6$, **Ma** $= 0.15$, $c_{flap}/c = 0.3$, $\eta = 40°$, $\alpha = -5°$, $c_\mu = 0.042$

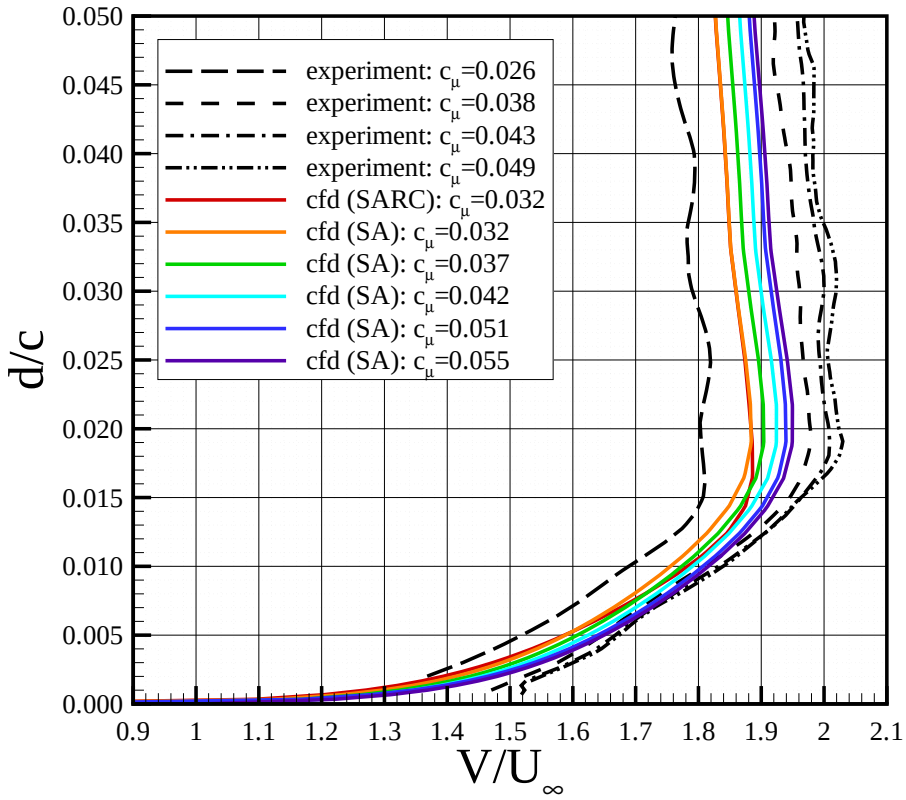

Figure 26. Distribution of total velocity at a position $15mm$ upstream of the slot for $\alpha = 0°$ ($\mathbf{Ma}_\infty = 0.15$, $\mathbf{Re} = 1 \cdot 10^6$)

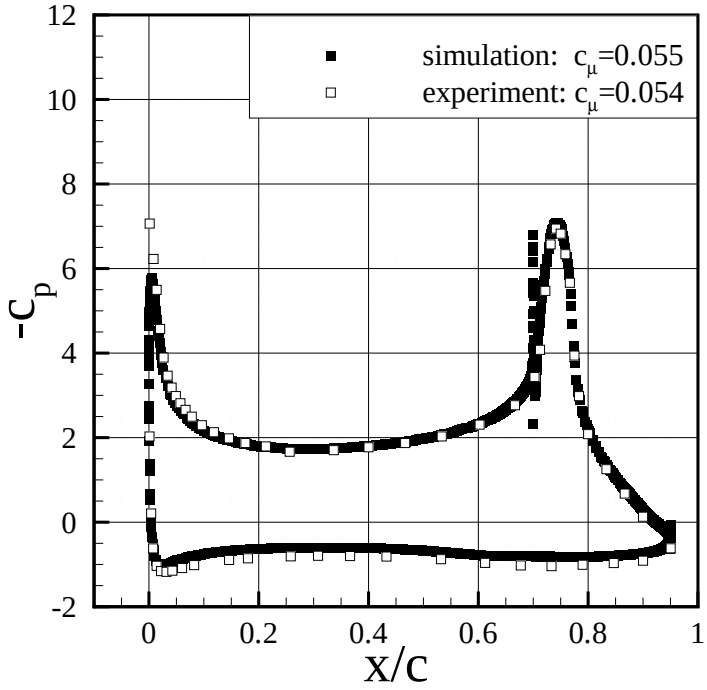

Figure 27. c_p**-distribution for** $\alpha = -5°$**,** $\mathbf{Ma}_\infty = 0.15$**,** $\mathbf{Re} = 1 \cdot 10^6$ **(SA turbulence model)**

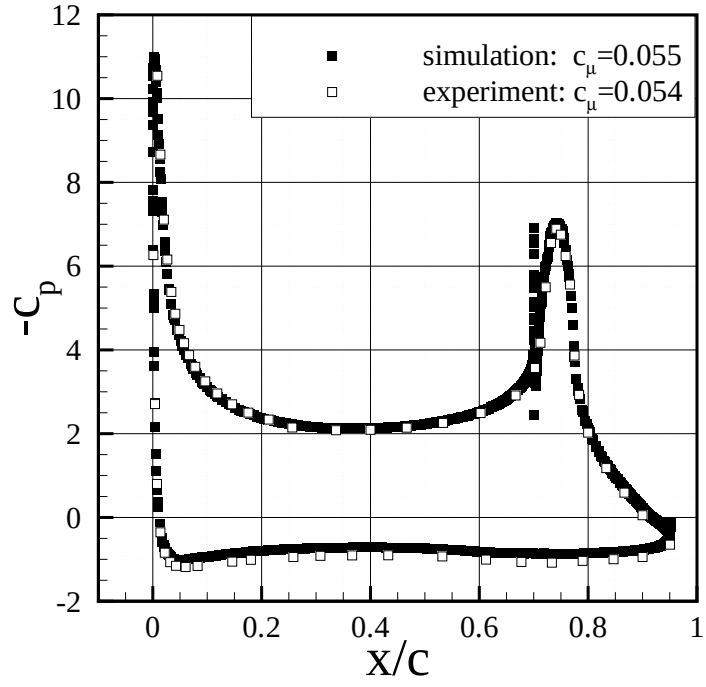

Figure 28. c_p**-distribution for** $\alpha = 0°$**,** $\mathbf{Ma}_\infty = 0.15$**,** $\mathbf{Re} = 1 \cdot 10^6$ **(SA turbulence model)**

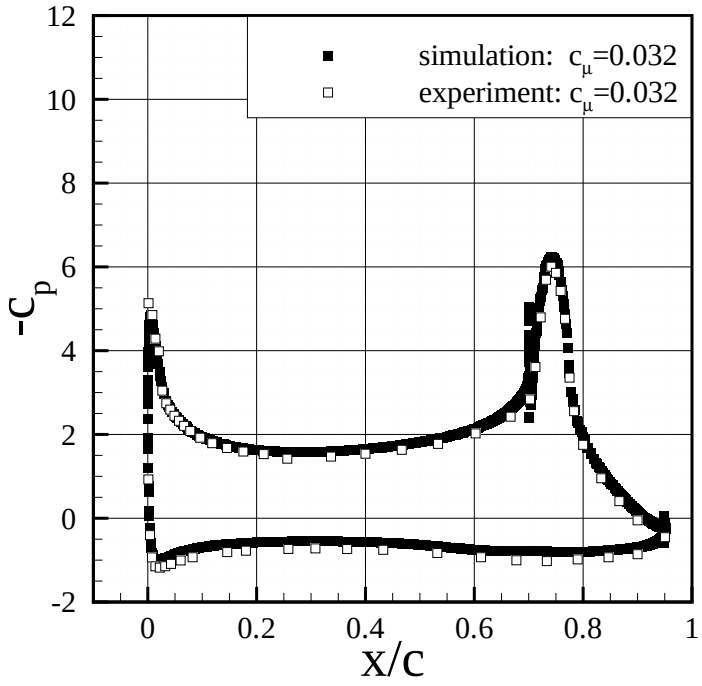

Figure 29. c_p**-distribution for** $\alpha = -5^\circ$**,** $\mathbf{Ma}_\infty = 0.15$**,** $\mathbf{Re} = 1 \cdot 10^6$ **(SA turbulence model)**

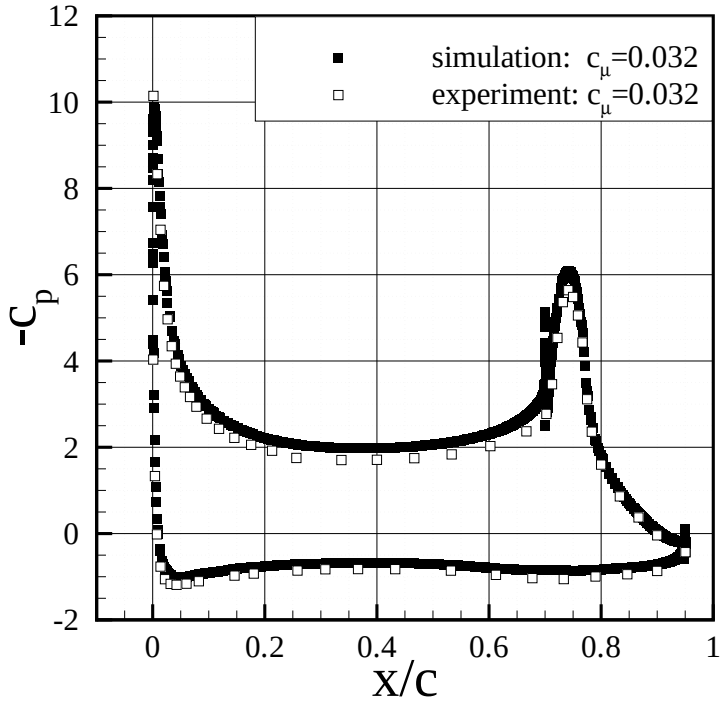

Figure 30. c_p**-distribution for** $\alpha = 0^\circ$**,** $\mathbf{Ma}_\infty = 0.15$**,** $\mathbf{Re} = 1 \cdot 10^6$ **(SA turbulence model)**

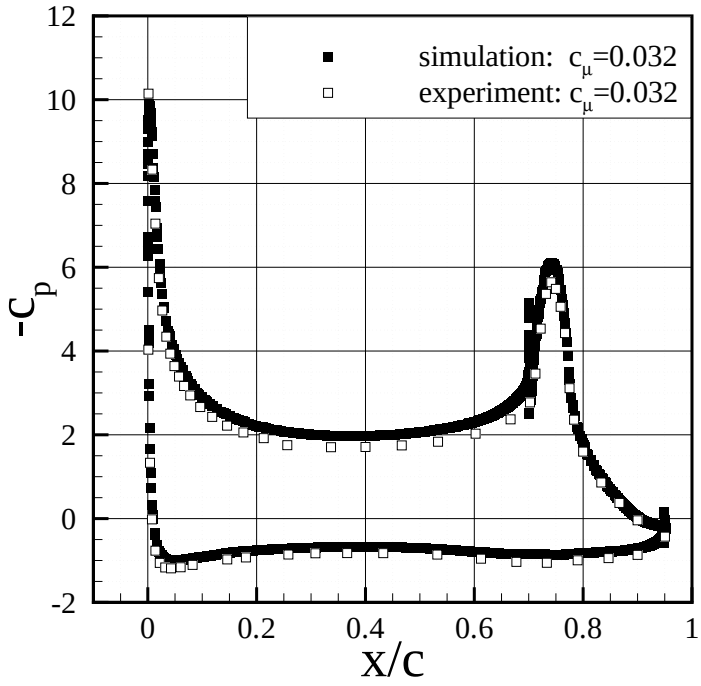

Figure 31. c_p**-distribution for** $\alpha = 0^\circ$**,** $\mathbf{Ma}_\infty = 0.15$**,** $\mathbf{Re} = 1 \cdot 10^6$ **(SARC turbulence model)**